PhD degree in System Medicine (curriculum: Molecular Oncology)
European School of Molecular Medicine (SEMM)
University of Milan

MICHELE CRESTANI
IFOM, Milan
R12422

Mechanoproperties, heterogeneity and cell migration in glioblastoma

Supervisor: Dr. Nils Gauthier

Academic year 2022/2023

Acknowledgements

Ringraziamenti

Rimango sempre della stessa convinzione di 5 anni fa, quando scrissi la tesi di master. Se sono arrivato dove sono è grazie al supporto di mamma e papà. Sono le persone che hanno creduto in me ancor prima che io stesso lo facessi, dandomi tutto il supporto del mondo affinchè camminassi sulle mie gambe. Saranno sempre le prime persone che ringrazierò, insieme a Marghe. Grazie ad Annalisa, compagna di vita, per supportarmi ogni giorno e vivere insieme le più delicate transizioni e ogni cambiamento, più o meno grande che sia. Se non ci fossi stata non so se avrei tirato fuori un decimo delle palle che tu e Cesare tirate fuori ogni giorno. Grazie a Maya, l'unica a dare sempre ed incondizionatamente amore. Voi tutti siete famiglia.

Grazie a Nils e Pascale, i miei "happy supervisors", per avermi dato fiducia fin da prima che ci conoscessimo profondamente. Penso che umanamente sia la gratificazione migliore che si possa ricevere, ben più degli insegnamenti tecnici che sono stati in grado di impartirmi durante questi 4 anni.

Se sono il ricercatore che sono diventato è grazie ad Andreone AG, Piccione (fai schifo!) e Ale (mitico!). Finchè si è stati tutti e 4 insieme il lavoro in IFOM è stato non solo profittevole, ma anche divertentissimo. Un grazie a Tania, umanamente e lavorativamente squisita, e a Cami, per *"averle fatto passare l'anno più bello del suo PhD"*. Grazie a Paolo, sempre disponibilissimo e gentilissimo a lavoro, di un'integrità morale d'altri tempi. Con lui, Paulina e Margaux il Gauthier-Maiuri lab è stato il punto di riferimento lavorativo del PhD.

Uno degli affetti più grandi incontrati durante il PhD è Sergio *"Rambo"* Cattadori, vera quercia di IFOM, hai lasciato un segno indelebile in tutti quelli che ti sono stati vicino. Grazie ai Maiali Ram, Zika, Nikos, Corey per le risate condivise e le idee scambiate anche al di fuori dal lab, mi avete aiutato a mantenere un altro punto di

vista. Grazie ai disgraziati Francesco - vera amicizia che mi porterò sempre dalla classe di PhD - e Ilaria, sempre di compagnia, e mai banali. Weber, grande e grosso ma un pezzo di pane, sembra che ci si conosca dalle scuole elementari. Ylli, con cui si è creata da subito sintonia e amicizia. Claudio P, ironico e intelligente in maniera fuori dal comune. Grazie a voi per essere stati lo zoccolo duro dei miei affetti in questi 4 anni in IFOM, insieme a Giulia, Euplio, Maira, Vanessa, Davide, Salvo, Ben, Robi, Diso, Beppe, Matteo, Flora, Olga, Anastasiya, Nicola, Mariagrazia e tutti i membri del Lab B; Dima, Alex, Francesca, le SF, Claudio M e gli Isotopi, Sharon, Ilaria la giuana, chef Rosario, Davide G, Daniel, Barnabas; la classe del PhD. Una menzione speciale per Qingsen, per avermi aiutato nella transizione verso IFOM, e per Sam e Susi: siete d'oro, e grazie per aver condiviso con me il vostro cristallino talento nel ping-pong!

Grazie a Giorgio, Benoit Marc-Antoine, e Monica per il supporto scientifico datomi durante il PhD. Grazie a tutti quelli che fanno andare avanti la macchina IFOM, dalla cucina ai manutentori, dalla sicurezza alle facilities.

Grazie a tutti gli amici della PM - Loca, sei stato quello che si è interessato più di tutti al mio percorso, ed infatti sei una testa fuori dal comune - e di Singapore, ai Barigiat - specialmente Marco e Matte, siete gli amici di una vita. Tutti quanti, sarete sempre un riferimento e, anche se ci si vede poco, quando ci si vede sembra che non ci si veda da ieri.

Mi scuso con chi potrei aver dimenticato, ma sto scrivendo queste righe all'ultimo momento disponibile.

Un grazie finale ai miei compagni di viaggio: James, Alessandro, Hannah, Fabrizio, Ernesto, Tiziano, Jack, Jill, Ernest, Vincent, Valerio, Joan, Byung-chul, Hermann, Jerome, Antonia. Siete sempre un'ancora di salvezza e se sono chi sono è anche grazie a voi.

A final apology for my non-italian-speaking friends going through this: I felt like writing the acknowledgements in my mothertongue.

Abstract

Glioblastomas (GBMs) are primary brain tumors endowed with inter- and intra-patient heterogeneity and extreme diffusivity. As heterogeneity is studied with genomic and transcriptomic analysis, little is known on how it is reflected on cell migration, mechano-properties and motility modes. Generally, the tumor cells invade the brain moving on brain vasculature or white matter tracks: Patient-Derived Xenograft (PDX) has been a standard to reproduce them in order to study GBM invasion. However, PDX presents many disadvantages, including time consumption, hard standardization, high cost and ethical concerns.

The present PhD thesis report aims at summarizing the existing literature through an historical journey that gradually walks the reader towards the state of the art in the biological knowledge, therapeutic treatments, and bioengineering of GBM. It also reports the results of this PhD work. They include novel bioengineering tools for studying the mechanoproperties in GBM and the development of methods to dissect their migration and motility modes. Finally, a stand-alone assay aims at fostering a discussion on how the scientific mindset and science have evolved and are evolving to drive technological innovation in nowadays' world.

The main goal of this PhD work was to develop bioengineering tools to crack mechanoproperties and GBM motility. Initially, by utilizing clones of patient-derived GBM cells that were either highly proliferative or highly invasive, I co-studied their cellular architecture, migratory, and biophysical properties. One of the milestones of this PhD work consists in the link between that invasiveness and cellular fitness. The most invasive cells were stiffer, developed higher mechanical forces on the substrate, and moved stochastically. The mechano-chemical-induced expression of the formin FMN1 supports the mechanical cohesion of the cytoskeleton and enhances cell's mechanoproperties, leading to a higher motility and invasive phenotype.

In order to scale up the motility screen to several GBM clones, I co-developed SP2G

(SPheroid SPreading on Grids), the live imaging of GBM spheroids spreading on grid micropatterns mimicking the brain vasculature. To counteract the issues in PDX and rapidly identify the most invasive sub-populations hidden in heterogeneous GBMs, we developed an *in vivo* mimicry platform named SP2G (SPheroid SPreading on Grids). Live imaging of tumor-derived spheroids spreading on gridded micro patterns imitating the brain vasculature mimicked 3D motility features observed in brain or 3D matrices. Using patient-derived samples coupled with a semi-automated ImageJ/Fiji macro suite, SP2G easily characterized and sorted differences in cell migration and motility modes through a set of 6 parameters (area expansion, diffusivity, boundary speed, collective migration, directional persistence, hurdling). Moreover, SP2G exposed the hidden intra-patient heterogeneity in cell motility that correlated molecularly to specific integrins. Thus, SP2G is intended as a versatile and potentially pan-cancer workflow to identify the invasive tumor sub-populations in patient-derived specimens. SP2G represents an integrative tool, available as open-source Fiji macro suite, for therapeutic evaluations at single patient level.

Contents

1 Introduction **20**

1.1 Understanding glioma patophysiology through an historical journey . . 22

1.1.1 Early discoveries in gliomas and the concept of GBM 22

1.1.2 Pheno- and genotypization, stem cells, inter- and intra-patient heterogeneity: the modern understanding of GBM 27

1.1.3 A brief overview on surgery, therapies and survival from the discovery of GBM: where is the state of the art? 34

1.2 Importance of cell migration in GBM tumors 39

1.2.1 The brain parenchyma and its interaction with GBM cells . . . 40

1.2.2 The brain blood vessels and their interaction with GBM cells . . 42

1.2.3 GBM migration and stem cells: defining tumor niches 44

1.3 Importance of functional cellular networks in GBM tumors 47

1.4 *In vitro* tools to mimic GBM migration 50

1.4.1 Bioengineering the extracellular matrix: the role of chemical composition 51

1.4.2 Bioengineering the extracellular matrix: the role of mechanics and mechanical gradients 52

1.4.3 Bioengineering interfaces and topographical cues: the role of blood vessels and white matter tracts 53

1.4.4 Bioengineering co-culture systems: the role of parenchymal cells 56

1.5 Hypotesis and goal 60

2 Results **63**

2.1 Spinning off from *"Adaptive mechanoproperties mediated by the formin FMN1 characterize glioblastoma fitness for invasion"* 63

2.2 SP2G mimics glioblastoma invasion on brain blood vessels 67

2.3 SP2G experimental setup and image analysis workflow 73
2.3.1 Characterization of cell migration with SP2G 73
2.3.2 Characterization of cell motility modes with SP2G 76
2.4 SP2G quantifies migratory tactics adopted by glioblastoma cells 83
2.5 SP2G reveals heterogeneity in the migratory tactics adopted by glioblastoma sub-populations isolated from patient-derived cell lines 93
2.6 Transcriptomic analysis of GBM7 sub-populations validates intra-patient heterogeneity highlighted with SP2G 104
2.7 Preliminary studies of functional cellular networks validate the motility modes detected by SP2G 108

3 Discussion 112
3.1 Comparison of SP2G with other *in vitro* systems 112
3.2 Advantages introduced by SP2G analytical toolbox 113
3.3 Advantages introduced by utilizing spheroids 114
3.4 SP2G added value in studying glioblastoma heterogeneity 115
3.5 Discussion of preliminary results obtained in the study of glioblastoma functional networks 116
3.6 Expanding SP2G towards a pan-cancer screening method 117
3.7 Limitations of this study 118
3.8 Debatable: is science running out of (original) ideas? 121

4 Materials and Methods 137
4.1 FMN1 shRNA design and cloning 137
4.2 Cell culture 138
4.3 Cell Transfection 138
4.4 Brain slice invasion assays and staining 139
4.5 Collagen and Matrigel invasion assays 140
4.6 Quantification of SPheroid SPreading (SP2) with area ratio and Mean Squared Displacement (MSD) 140
4.7 Generation of radar plots to assess *in vitro* system performance 141
4.8 Microcontact printing 141
4.9 SPheroid SPreading on Grids (SP2G) experimental and image analysis workflow 141

4.10 Simulation of particle diffusion 144
4.11 RNA sequencing 144
4.12 RNA extraction and qPCR analysis 144
4.13 Analysis of RNA sequencing data 145
4.14 Protein extraction and western blots 145
4.15 Statistical analysis and data availability 146
4.16 Calcium imaging and wave propagation 146
4.17 SP2G experimental protocol 147
4.17.1 Materials 147
4.17.2 DilC18 membrane dye preparation 147
4.17.3 Microcontact printing 147
4.17.4 Spheroid spreading 147

Abbreviations

AI Artificial Intelligence

AIRC Fondazione AIRC per la Ricerca sul Cancro

AMPAR α-Amino-3-hydroxy-5-Methyl-4-isoxazole Propionic Acid Receptor

BBB Blood-Brain Barrier

BCNU 1,3-Bis[2-chloroethyl]-l-nitrosourea

CDF Cumulative Distribution Function

CN Collagen

CNS Central Nervous System

CSF Cerebrospinal Fluid

CT Computed Tomography

CX43 Connexin 43

DNA Deoxyribonucleic Acid

ECM Extracellular Matrix

EGF Epidermal Growth Factor

ERC European Research Council

FA Focal Adhesion

FDA Food and Drug Administration

FN Fibronectin

G-CIMP Cytosine-Phosphate-Guanine Island Methylator Phenotype

GAP43 Growth-Associated Protein 43

GBM Glioblastoma

GFAP Glial Fibrillary Acidic Protein

GFP Green Fluorescent Protein

GSEA Gene Set Enrichment Analysis

HA Hyaluronic Acid

HIF Hypoxia-Inducible Factor

HUVEC Human Umbilical Vein Endothelial Cells

IDH Isocitrate Dehydrogenase

IHC Immunohistochemistry

KEGG Kyoto Encyclopedia of Genes and Genomes

LaMDA Language Models for Dialog Applications

LN Laminin

MGMT O6-Methylguanine-DNA Methyltransferase

MMP Matrix Metalloproteinase

MRE Magnetic Resonance Elastography

MRI Magnetic Resonance Imaging

MSD Mean Squared Displacement

NAD Nicotinamide Adenine Dinucleotide

NADP Nicotinamide Adenine Dinucleotide Phosphate

NF1 Neurofibromin 1

NIH quantitative National Institute of Health

OF Orientation Field

PA Polyacrylamide

PCA Principal Component Analysis

PCL Polycaprolactone

PCR Polymerase Chain Reaction

PDGF Platelet-Derived Growth Factor

PDMS Polydimethylsiloxane

PDX Patient-Derived Xenograft

PEG Polyethylene Glycol

PLL poly-L-lysine

qPCR quantitative PCR

RA Running Average

RNA Ribonucleic Acid

RNA-seq RNA-sequencing

ROI Region Of Interest

shRNA Short Hairpin RNA

SP2 SPheroid SPreading

SP2G SPheroid SPreading on Grids

TCGA The Cancer Genome Atlas

TERT Telomerase Reverse Transcriptase

TM Tumor Microtubes

TNT Tunnelling Nanotubes

VEGF Vascular-Endothelial Growth Factor

WHO World Health Organization

WWII World War II

List of Figures

1.1 Wiews of glia in 1860 and today 23
1.2 Reticularists vs. Neuronists 24
1.3 Classification scheme of primary brain tumors by Bailey and Cushing 26
1.4 Secondary structures of Scherer 27
1.5 Differentiation of GBM patient-derived cells 30
1.6 Integrated view of gene expression and genomic alterations across glioblastoma subtypes highlights inter-patient heterogeneity 32
1.7 Intra-patient heterogeneity in GBM tumors 33
1.8 Kaplan–Meier survival plots for patients diagnosed with GBM 37
1.9 MRI scans of a patient affected by GBM illustrating the spread of the disease 40
1.10 Basal laminae in brain blood vessels and schematic depiction of the glymphatic pathway 43
1.11 GBM migration and stem cell niches 45
1.12 GBM tumors form functional and resistant networks 48
1.13 Overview of different mechanobiology techniques used to study mechanochemical and topographical cues for glioma motility 54
1.14 Overview of different mechanobiology techniques used to study how interfaces and co-culture systems affect glioma motility 57

2.1 Gridded micropatterns mimic the brain blood vessel network 64
2.2 Motility on grids of patient-derived GBM cell lines 64
2.3 Spheroid embedding as validation of motility phenotypes 65
2.4 Brain slice overlay assay as validation of motility phenotypes 66
2.5 Comparison between *in vitro* setups hints at SP2G efficiently mimicking glioblastoma invasion on brain blood vessels 68

2.6 SPheroid SPreading on Grids (SP2G) quantification and substrate . . 69
2.7 SPheroid SPreading on Grids (SP2G) vs brain slice assay 69
2.8 Single cell behavior in SPheroid SPreading on Grids (SP2G) 70
2.9 SPheroid SPreading on Grids (SP2G) is independent from spheroid size, both considering area ratio and Mean Squared Displacement (MSD) 71
2.10 SPheroid SPreading on Grids (SP2G) is independent from spheroid size, both considering area ratio and Mean Squared Displacement (MSD) 72
2.11 SP2G experimental setup and image analysis workflow 74
2.12 SP2G: validation for collective migration algorithm 78
2.13 SPheroid SPreading on Grids (SP2G) at 0 h, 4 h, and time projections (maximum intensity, phase contrast) of patient-derived glioblastoma cells from NNI-21, NNI-24, NNI-11 Glioblastoma (GBM) cell lines . . 83
2.14 Benchmarking SPheroid SPreading on Grids (SP2G) with NNI-21, NNI-24, NNI-11 Glioblastoma (GBM) cell lines 84
2.15 Average polygon visualizing migration area for NNI-21, NNI-24, NNI-11 85
2.16 Diffusivity and boundary speed for NNI-21, NNI-24, NNI-11 85
2.17 Motility modes for NNI-21 and NNI-24 86
2.18 Testing SPheroid SPreading on Grids (SP2G) with cytoskeleton-perturbing drugs 87
2.19 SP2G detects the different migratory tactics upon inhibition of Arp2/3, myosin II, microtubules and f-Actin 88
2.20 SP2G detects the different motility modes upon inhibition of Arp2/3, myosin II, microtubules and f-Actin 89
2.21 SP2G detects the different migratory tactics upon changes in laminin concentration on the substrate 91
2.22 SP2G of the patient-derived cell line GBM7 heterogeneous bulk 93
2.23 SP2G of the patient-derived cell line GBM7 sub-populations 94
2.24 SP2G reveals heterogeneity in the migratory tactics adopted by glioblastoma sub-populations isolated from the GBM7 patient-derived cell line 95
2.25 Speroid Spreading of GBM7 sub-populations (green, DiOC6 dye) lent against an *ex-vivo* brain slices 96
2.26 SPheroid SPreading on Grids (SP2G) detects differences in the migration of GBM7 sub-populations 97

2.27 SPheroid SPreading on Grids (SP2G) detects differences in the motility modes of GBM7 sub-populations 98
2.28 SP2G of the patient-derived cell line GBM22 heterogeneous bulk . . . 98
2.29 SP2G of the patient-derived cell line GBM7 sub-populations 99
2.30 SP2G reveals heterogeneity in the migratory tactics adopted by glioblastoma sub-populations isolated from the GBM22 patient-derived cell line 100
2.31 SPheroid SPreading on Grids (SP2G) detects differences in the migration of GBM7 sub-populations 102
2.32 SPheroid SPreading on Grids (SP2G) detects differences in the motility modes of GBM22 sub-populations 103
2.33 Principal Component Analysis (PCA) showing segregation of the 5 GBM7 sub-population in motile (red) and non-motile (blue) groups . 104
2.34 Gene Set Enrichment Analysis (GSEA) of differentially expressed genes in the motile group (#09, #01, #07) vs non-motile ones (#03, #02) . 105
2.35 Heatmap representing z-score of expression levels of integrins 106
2.36 Bar plot of mRNA expression levels of ITGA1, ITGA2, ITGA3, ITGA5, ITGA6, ITGA7, ITGA10, ITGAV, and CD44 determined by qRT-PCR in the 5 GBM7 sub-populations 106
2.37 Integrin alpha6 is upregulated in motile clones compare to non-motile. 107
2.38 Intercellular communication and calcium waves propagation 108
2.39 Intercellular communication and expression of related proteins 109

3.1 The relationship between scientific effort on an idea and the scientific impact of the idea 126
3.2 The shift in scientists' effort away from exploration and toward incremental science 127
3.3 The impact factor and the edge factor for four ideas 128

List of Tables

1.1 Results from the clinical study by Roth and Elvidge 36
1.2 Cell-matrix and cell-cell adhesion molecules expressed in glioma cells compared with normal brain tissue 41

2.1 Table summarizing SP2G quantitative outputs and how to obtain them 79
2.2 Summary of the conditions tested with cytoskeleton-perturbing drugs (NNI-21) 86
2.3 Summary of the numerical outputs provided by SPheroid SPreading on Grids (SP2G) for cell migration of the GBM7 sub-populations . . . 97
2.4 Summary of the numerical outputs provided by SPheroid SPreading on Grids (SP2G) for cell migration of the GBM22 sub-populations . . 101

3.1 Summary of top 10 highest-grossing movies during the years 2018-2021 123
3.2 Summary of top 10 highest-grossing movies during the years 1993-1996 124

Chapter 1

Introduction

Glioblastoma is the most devastating form of brain tumor. A patient diagnosed with Glioblastoma (GBM) has almost no chances of survival, despite numerous studies on the topic. According to the 2021 World Health Organization (WHO) classification, GBM is a grade IV glioma officially named as *Glioblastoma, IDH-wildtype*, which

"should be diagnosed in the setting of an IDH-wildtype diffuse *and* astrocytic glioma in adults if there is microvascular proliferation *or* necrosis *or* TERT promoter mutation *or* EGFR gene amplification *or* +7/-10 chromosome copy number changes" [1].

Nowadays, scientists are growingly being seduced by technology-driven and data-driven approaches, which, in numerous type of cancers, pinpoint them as patient-specific diseases. A glimpse into the history of science shows how GBM has been considered individually unique at all times: in one of the earliest studies from 1926, Percival Bailey and Harvey Cushing classified the *"gliomata"* in no less than 14 categories. Up to the year 2000, GBM was officially known as *Glioblastoma Multiforme* due to the multiplicity of its facets: one of the most remarkable is its diffusivity. GBM cells aggressively invade the brain, leading to the patient's death. The Introduction of this PhD thesis report describes the known *whys*, *hows*, and the existing tools to study the way GBM cells move. However, how GBM *multiple forms* are reflected on its invasion is still poorly studied: the Results section includes a novel approach describing part of the *whys* and the *hows* that endow glioblastoma with *multiple forms* during the process of cell migration.

This PhD project was carried out combining expertise from biology, bioengineering and biophysics aiming to provide a tool for the careful dissection of GBM migration within and between patient-derived samples.

1.1 Understanding glioma patophysiology through an historical journey

I firmly believe that the careful understanding of any topic requires a dive into its history. In the fascinating chronicles of GBM, Hans Joachim Scherer was the pioneer who sharply summarized the work done until 1940 on cerebral gliomas and brought forward key pathophysiological ideas that are still accepted nowadays and expanded in the molecular biology and omics era.

1.1.1 Early discoveries in gliomas and the concept of GBM

Scherer's review [2], a watershed in glioma literature, cites the works published on British Scientific Reports by Berns in 1800 and by Abernety in 1804 as the first recorded papers on Central Nervous System (CNS) tumors. During these years, the authors provided gross morphological observations from autopsy materials, which described CNS tumors as a disease having macroscopical resemblance to normal brain tissue. Each school was coining its own jargon: the British used the term *Medullary Sarcoma*, the French *Encéphaloïde*, and the German knew GBM as *Fungus Medullare* [2, 3].

Rudolph Carl Virchow, one of the most towering scientists from the 19$^{\text{th}}$ century, revolutionized the approach to biomedical research [4]. In his vision, medical doctors had to look at pathophysiological states both at the macroscopic and the microscopic level, believing that any disease could initiate at the cellular level. From his lectures, held at Berlin University between 1858 and 1863 [5, 6], he identified the glial cells and created the name *"Glioma"* to indicate their cancerous degeneration. Glia derives from the Greek γλια and γλοια, "glue": at that time scientists believed that it was a homogeneous set of Extracellular Matrix (ECM)-secreting cells within the CNS. Nowadays, we know that the glia not only supports tissue integrity in the brain, but is composed of several cell lines (oligodendrocytes, Schwann cells, microglia, astrocytes) that are key in the maintenance of brain homeostasis and neural circuitry (Fig. 1.1) [7]. As for the descripiton of gliomas, Virchow differentiated between *"Glioma"* (*"enormous tumours of brain-like appearance, never showing a clear limitation towards the normal brain tissue; microscopically they are formed by a proliferation of glia cells and sometimes of glia fibres"*) and *"Sarcoma"* (*"tumors of spherical shape*

A

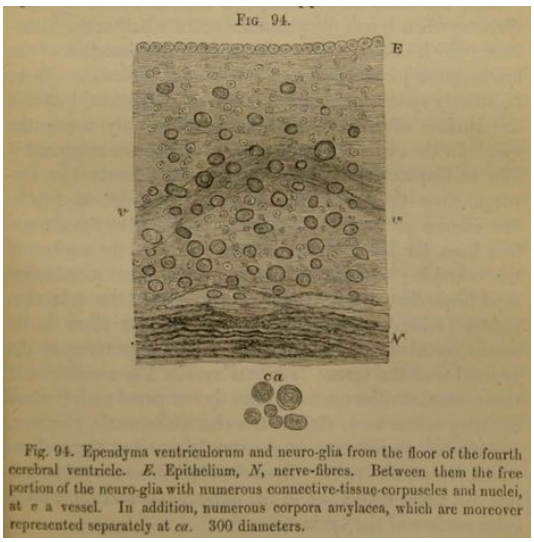

B

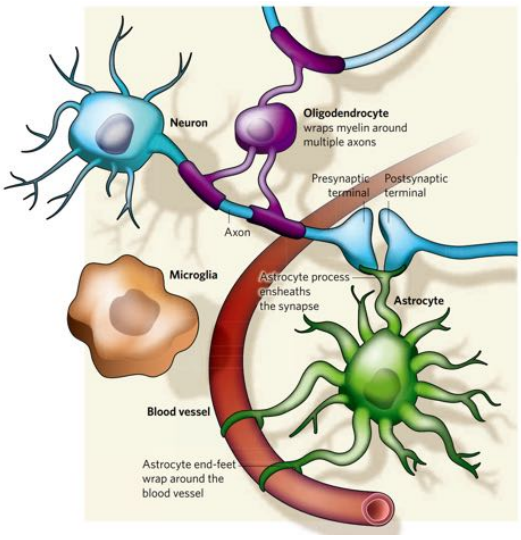

Figure 1.1: Wiews of glia in 1860 and today. (A) Wood engraving reported in Virchow's book of lectures. The glia is seen as an homogeneous set of cells. Adapted from [5], p. 275. (B) Glia–neuron interactions. Different types of glia interact with neurons and the surrounding blood vessels. Oligodendrocytes wrap myelin around axons to speed up neuronal transmission. Astrocytes extend processes that ensheath blood vessels and synapses. Microglia keep the brain under surveillance for damage or infection. Adapted from [7].

and definite boundaries, high cellularity and much larger, often fusiform, shape of cell; characterized by high vascularity and pronounced fatty degeneration"). Despite the immaturity of histological procedures at his time, what Virchow named *"Glioma"* strikingly matches the 2016 WHO classification of grade I,II CNS tumors, and what he named *"Sarcoma"* matches grade III,IV CNS tumors [3, 8].

The groundbreaking tool for the exploration of brain structures was invented during the next decade, by Camillo Golgi. In 1873, he published a novel histological procedure, named *"la reazione nera"* - "the black reaction" [9], which allowed to stain nerve cells in brain tissue samples with a black color at high contrast. After fixing the tissue in 2.5% potassium dichromate (1 to 45 days), its prolonged immersion in a 0.5-1% silver nitrate bath caused the precipitation of the salt silver chromate, which ultimately filled the neuron bodies up to the thinnest dendrite. However, the efficiency of Golgi's methodology was low (1 to 5% of neurons were successfully stained) [10]. At that time, the scientific community was disputing over the organization of tissues and the role of cells within them. Despite his observations, Golgi and the *Reticularists* believed the nervous system to be a continuous syncytium, and its functions the result of a collective action of fused nerve processes. The neu-

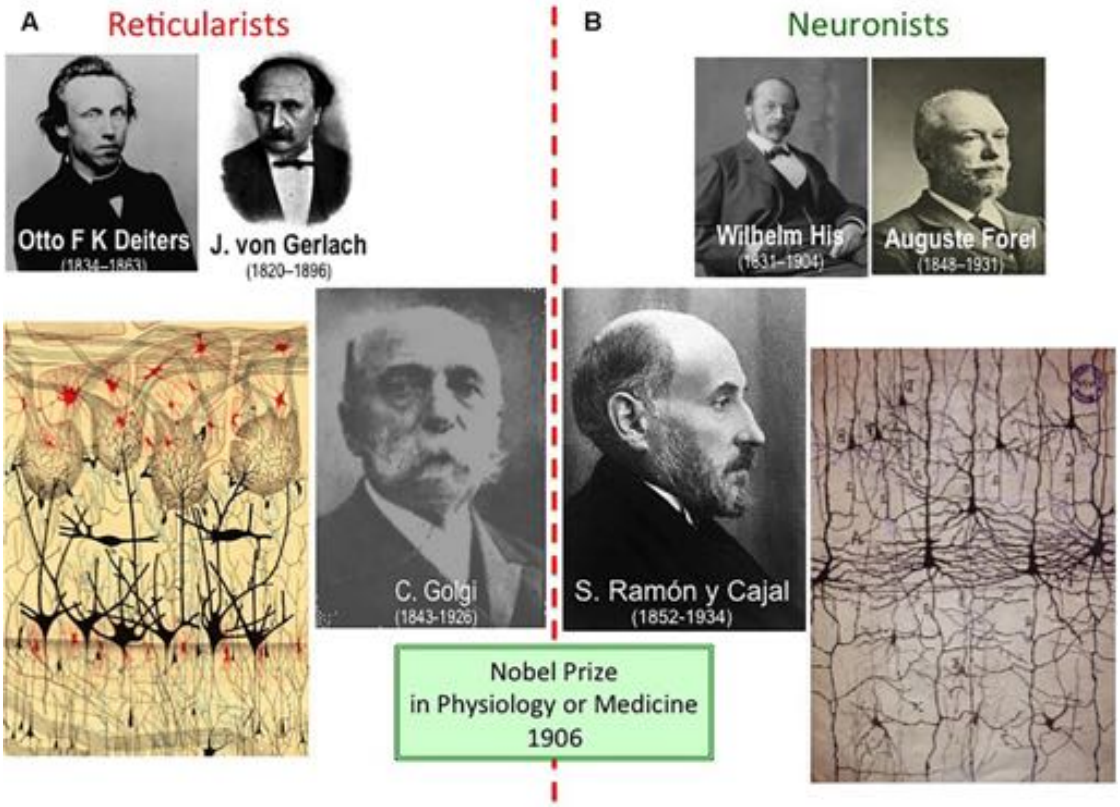

Figure 1.2: Reticularists vs. Neuronists. (A) Otto Reiters and Joseph von Gerlach initially proposed the "reticular theory", and later Camillo Golgi became the most prominent reticularist. (B) "Neuronism" was raised by Wilhelm His and August Forel as the "free endings hypothesis": the processes of each neuron could physically terminate and be in contact with their surroundings, keeping their own syncytium, contrarily to the view of the reticularists. Santiago Ramón y Cajal became the leader of the "neuron theory". How Golgi (left: drawing of the olfactory bulb) and Ramón y Cajal (right: pyramidal neurons from the cerebral cortex) presented their findings clearly differed, although both finally shared the Nobel Prize 1906. Adapted from [11].

rologist Santiago Ramón y Cajal optimized Golgi's black reaction in the '80s: he improved contrast and resolution of the images with a *"double impregnation"* step and he proved that the reaction worked best on non-myelinated axons by staining tissues from young/embryonic mammals, whose neurons are largely unmyelinated. Ramón y Cajal was the paladin of the *Neuronists*: they followed Virchow's ideas, according to which *"every animal appears as a sum of vital units, each of which bears in itself the complete characteristics of life"* [12, 13]. They thought that each neuron is the anatomical and independently functional "atom" of the nervous system, yet communicating with its neighbors (Fig. 1.2). Ultimately, the reticular theory turned

out to be obsolete and, ironically, Golgi and Ramón y Cajal shared the 1906 Nobel Prize for Physiology and Medicine *"in recognition of their meritorious work on the structure of the nervous system"* [14, 11].

The discoveries of Golgi and Ramón y Cajal paved the way to the histological era in GBM research. The first scientist who applied the newly-discovered methods to describe histological features was Heinrich Stroebe who, in addition to confirming Virchow's findings, provided the first detailed microscopical description of gliomas (1895) applying a multifocal, unbiased approach rather than confined to a single region of the lesion [15]. While reviewing Stroebe's work, in which the author described for the first time the polymorphism of glioma cells (i.e. its intratumoral heterogeneity) and detailed the microscopic differences between "*glioma*" and "*sarcoma*", Scherer cleverly envisioned the mechanical influence of the microenvironment on tumor cells, particularly on the cell shape, as they invade along pre-existing brain structures:

"[...] the essentially infiltrative growth type of "gliomas", using the pre-existent fasciculation of nerve fibres, which modifies the otherwise round shape of the tumour cells to an elongated one. This important notion that the cell form in gliomas may depend upon mechanical influences exercised by the pre-existent brain tissue has been entirely forgotten by most modern writers, who implicitly consider the forms of glioma cells as an exclusively intrinsic factor of 'histogenetic' significance." [2]

In addition to the detailed microscopic description of GBM histologies, other landmark discoveries for the CNS anatomy and biology that finally supported the "neuron theory" were: the presence of astrocytes (1893) by the hungarian histologist Mihály Lenhossék [16], the difference between grey and white matter (1893) [17], and the existence of oligodendrocytes and microglial cells (1919) by Wilder Penfield and Pío Del Río-Hortega - a collaborator of Ramón y Cajal [18, 19, 20, 21]. As the picture concerning the brain organization was clearly becoming more and more complicated, all these findings led in 1926 to the first extensive classification of gliomas. It was proposed by the American neuropathologist Percival Bailey and the father of modern neurosurgery Harvey Cushing (Fig. 1.3)[22], who baptized the most clinically malignant and histologically polymorphous form of glioma as *"Spongioblastoma*

Multiforme". They described this tumor has having no cells resembling neither glial

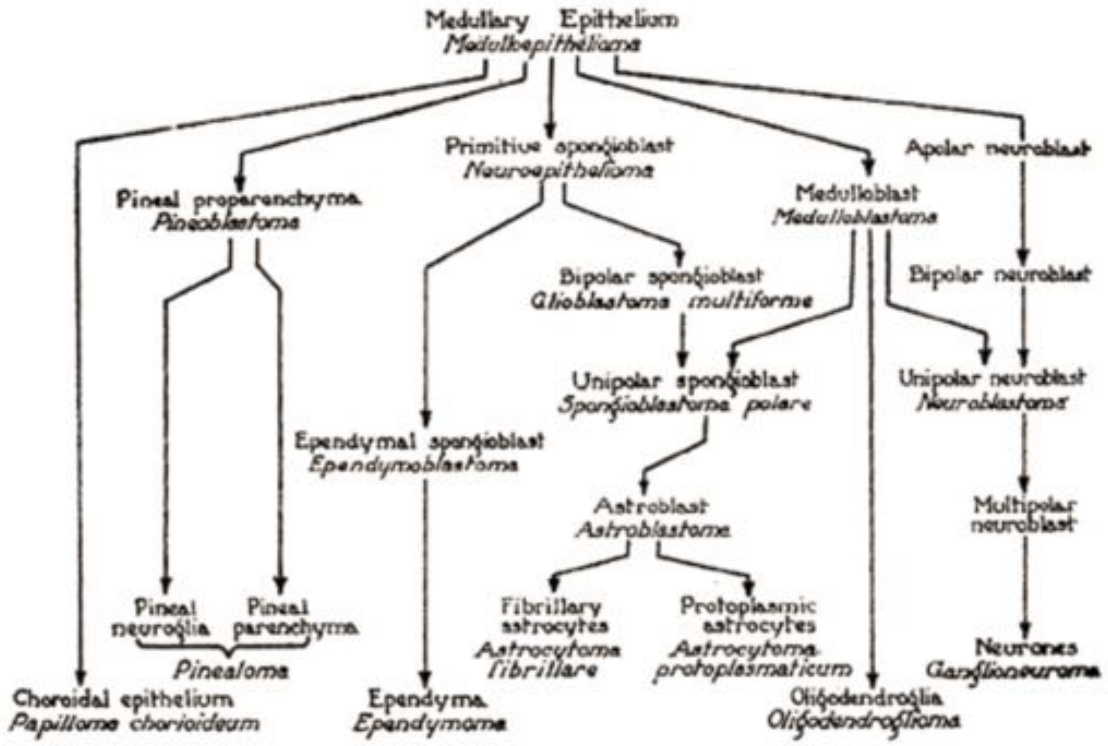

Figure 1.3: Classification scheme of primary brain tumors by Bailey and Cushing. Tumors were expected to arise from cells with corresponding differentiation. For example, ependymoma would originate from the ependyma or astrocytoma would originate from astrocytes. Adapted from [23].

cells, nor even other glioma cells. Scherer described this work as bearing *per se* few new facts (such as the discovery of oligodendrogliomas, cerebellar medulloblastomas) and being just a doctrinal classification, however he was aware of dealing with a milestone of glioma literature (and, nowadays, it is recognized so). In fact, their work proved for the first time that patient survival could be correlated with the histological properties of the lesion, probably aiming to facilitate clinicians in finding the best solution when dealing with patients. Their work also boosted the interest of the scientific community for brain tumors. Nevertheless, the term *"spongioblastoma"* was phased out with time and replaced with *"glioblastoma"*.

In his works, H. J. Scherer postulated that astrocytomas and glioblastomas can share the same cells of origin and that the former could degenerate in the latter (secondary glioblastoma), understanding the difference with primary glioblastomas (originating *de novo*) [2, 24]. Most importantly, he extensively described GBM as surrounding pre-existing brain structures, such as neural axons, the Virchow-Robin

spaces (i.e. the abluminal side of blood vessels that, among the myriad of his contributions, were described by Rudolph Virchow along with Charles-Philippe Robin, a French scientist), and white matter tracts, which are thick bundles of several axons (Fig. 1.4). These 3 structures were later named Secondary Structures of Scherer - primary structures are independent from pre-existing structures and pertain the biology of the tumor, such as rosettes, whorls, papillary structures, canalicular and glandular formations, since he foresaw that this interaction was due to GBM cell migration (see section 1.2) [24, 25].

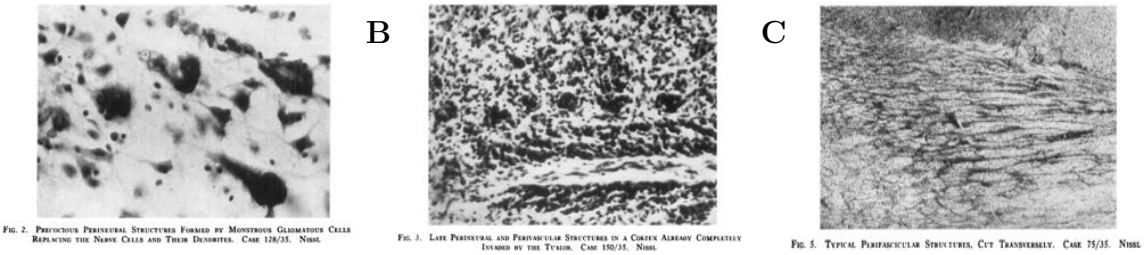

Figure 1.4: Secondary structures of Scherer. (A) Histology of GBM cells positioned along neuronal axons. (B) Histology of GBM cells populating the abluminal side of brain blood vessels. (C) Histology of GBM cells infiltrating white matter tracts. Adapted from [24].

1.1.2 Pheno- and genotypization, stem cells, inter- and intra-patient heterogeneity: the modern understanding of GBM

After Scherer's death in a bomb attack during the last stages of World War II (WWII), in 1945, the most relevant progresses in glioma research until circa the years 1990-2000 belonged to the clinical side and are discussed in the next subsection of the thesis. Beforehand, 2 main technological breakthroughs innovated the field of glioma research: electron microscopy and Immunohistochemistry (IHC). With the advent of electron microscopy, scientists analyzed (sub)cellular compartments and organelles, discovering the synaptic structure and definitively killing the "reticular theory". However, immunohistochemistry replaced electron microscopy as a tool to obtain a deeper clinical knowledge than provided by classical histological procedures [3, 26]. Lineage-specific antibodies constitute one of the most powerful methodologies for glioma classification and characterization. For example, Glial Fibrillary Acidic Protein (GFAP) IHC proved that pleomorphic xanthoastrocytoma

and chordoid glioma of third ventricle were of glial nature [27, 28], which led to their inclusion in 2016 WHO classification, demonstrating the IHC impact on CNS tumor diagnosis [8] (GFAP is a class III intermediate cytoskeletal filament found in all astrocytes). Other key glioma markers are, for instance, Vimentin (another class III intermediate cytoskeletal filament found in all cells with a mesenchymal origin), S-100B (a marker for astrocytes; S-100 is a family of 24 proteins involved in motility, cell growth, differentiation, cell cycle functions; the most common in glial cells and GBM is S-100B), Cytokeratin AE1/AE3 (type I and type II intermediate cytoskeletal flaments, respectively) and, for abnormal cell proliferation, Ki-67 (a nuclear protein associated with cell proliferation) [29].

In the '80s, with the inventions of Western Blotting [30] and Polymerase Chain Reaction (PCR) [31], science entered the molecular biology era, which truly revealed the *multiple forms* of GBM and allowed the identification of biomarkers. In this sense, key findings consist in the O6-Methylguanine-DNA Methyltransferase (MGMT) promoter methylation status and Isocitrate Dehydrogenase (IDH) mutations that allowed to stratify patients and classify gliomas according to their molecular profiles. MGMT is a DNA-repair enzyme that prevents alkylating agents (i.e. compounds that attaches alkyl groups - C_nH_{2n+1} - to the Deoxyribonucleic Acid (DNA), thus preventing its transcription into Ribonucleic Acid (RNA) and stopping protein synthesis) to kill tumor cells. Methylation of MGMT promoter silences the gene, and cells produce no more MGMT. A landmark clinical study showed correlation between patient survival and MGMT promoter methylation status: when treated with the alkylating agent 1,3-Bis[2-chloroethyl]-l-nitrosourea (BCNU), patients with a methylated MGMT promoter had a better survival, since the DNA of tumor cells was not repaired by the enzyme and efficiently damaged by the chemotherapy [32]. IDH1 and IDH2 are enzymes that catalyze the oxidative decarboxylation of isocitrate to α-ketoglutarate and reduce Nicotinamide Adenine Dinucleotide (NAD)+ and Nicotinamide Adenine Dinucleotide Phosphate (NADP)+ to NADH and NADPH, respectively. They are involved in the tricarboxylic acid cycle, as well as in protection against oxidative stress: in low-grade gliomas and secondary GBM they are often mutated, while they are not in primary GBMs [33]: this critical finding, along with co-deletion of chromosomes 1p and 19q, constitutes the most striking example of how the combination of geno- and phenotypization has powerfully characterized glioma biology and classification in the last 25 years. As long as clinicians used to employ only histological techniques for

diagnostic purposes, oligodendroglioma was indistinguishable from astrocytoma: both were falling under the group "oligoastrocytoma". With geno- and phenotypization, IDH mutation and chromosomes 1p/19q codeletion were identified and catalogued in the 2016 WHO classification as astrocytoma hallmarks, while oligodendroglioma keeps a wild-type genotype for IDH and 1p/19q status [34, 8].

Thanks to the technologies introduced with the molecular biology breakthroughs, other key signalling pathways involved in the oncogenetic potential of GBM were identified along the years. Some of the most remarkable are related to tyrosine kinase receptor-triggered pathways, such as Epidermal Growth Factor (EGF), Vascular-Endothelial Growth Factor (VEGF), and Platelet-Derived Growth Factor (PDGF) receptor associated mutations; others involve mutations in the Ras and PI3K/PTEN pathways, the P53 tumor-suppressor protein and several microRNAs. Other mutations are key in GBM pathophysiology and many papers had reviewed them [3, 35]. Their illustration, however, is out of the scope of this PhD thesis.

The increasing *multiforms* unveiled by this type of approach has led to another landmark discovery in GBM field, namely that GBM cells are endowed with stem features, i.e. that possesses a marked capacity for proliferation, self-renewal, differentiation, and phenocopy the original tumor. In the early 2000s, various important works were published in this regard. In 2002, Ignatova and collaborators from the group of Dennis A. Steindler discovered that samples isolated from patients diagnosed with anaplastic astrocytoma and recurrent malignant GBM with abnormal P53 status (indicative of tumorigenicity) were able to give rise to independent clonal populations that expressed either neuronal (β-III tubulin) or glial (GFAP) cytoskeletal markers [36]. A year later, the group of Peter B. Dirks further confirmed that cells from primary pediatric brain tumors (obtained from patients with medulloblastoma, astrocytoma, ependymoma and ganglioglioma) were positive to stem cell markers [37], such as CD133 [38] and nestin [39]. The next year, Galli et al. from the group of Angelo Vescovi extended these findings to GBM [40]. They showed the multipotency of early passage, patient-derived GBM cell lines. Upon undergoing terminal differentiation *in vitro* (obtained by growing cells on matrigel-coated glass coverslips in the presence of 10 ng/ml leukemia inhibitory factor), GBM cell lines differentiated into GFAP-positive astrocyte-like cells, neuron-like cells that were immunoreactive for β-III tubulin, and galactocerebroside-immunoreactive oligodendrocyte-like cells (galactocerebroside, GalC, is a specific oligodendrocyte marker [41]). Conversely,

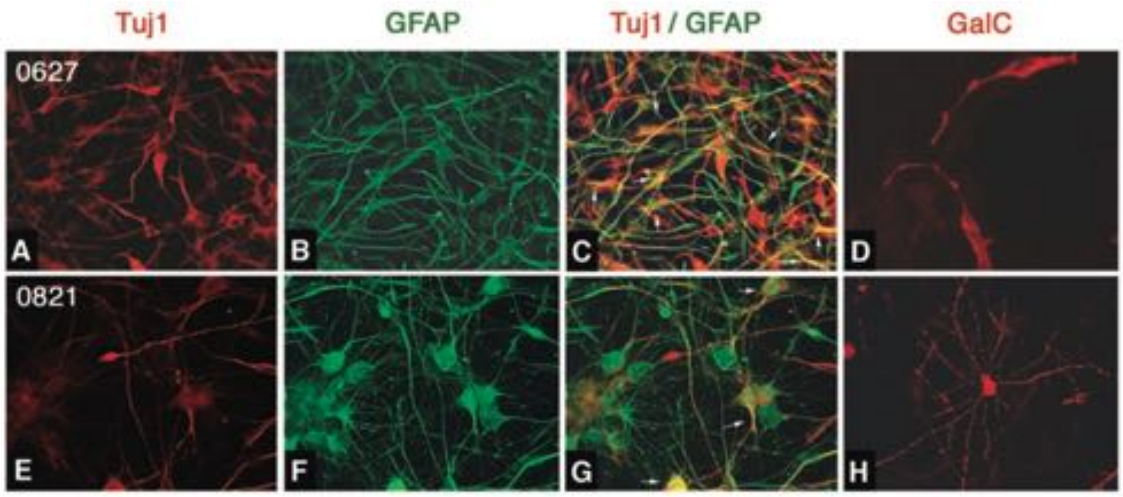

	βtub-IR cells (%)	GFAP-IR cells (%)	βtub/GFAP-IR cells (%)	GalC-IR cells (%)
0627	16 ± 2.7	25 ± 2.8	58 ± 2.4	4.8 ± 0.1
0913	18 ± 0.9	34 ± 3.3	41 ± 1.3	1.7 ± 0.1
1022	21 ± 1.5	29 ± 2.7	37 ± 0.9	2.7 ± 0.2
0821	18 ± 1.2	60 ± 0.9	22 ± 1.5	2.1 ± 0.1
1030	9 ± 0.9	21 ± 0.6	27 ± 0.9	1.3 ± 0.3
1205	5.5 ± 1.0	47 ± 1.4	44 ± 0.8	1.3 ± 0.6
HNSCs	29 ± 2.6	12.4 ± 2.1	negative	1.8 ± 0.7
U87	negative	negative	negative	negative

Figure 1.5: Differentiation of GBM patient-derived cells. In this work, Galli et al. analyzed the multipotency of the GBM patient-derived cell lines 0627 (representative of fast-growing cells) and the slow-growing 0821. Immunofluorescence for neuronal (β-III tubulin (Tuj1); red in A, C, E, and G), glial (GFAP; green in B, C, F, and G) and oligodendroglial (GalC; red in D and H) markers are depicted. Cells indicated with arrows were co-labeled with neural and glial markers. The table shows the percentage of cells with positive staining for the indicated markers in several patient-derived glioma cell lines, plus human fetal neural stem cells (HNSC) and glioma U87. This is intended as a proxy to generate cells of the three major neural lineages. Adapted from [40].

U87 cells (a commercial glioma cell line established from decades) were never positive for any of these antigen, demonstrating that multipotency is a unique property of patient-derived GBM cell lines highlighting thus the major relevance of this type of material (Fig. 1.5). Moreover, the authors showed this type of cells as able to form tumors when xenografted in mice, even when challenged through serial transplantations. Soon after, Singh and Dirks demonstrated that only CD133+ cells were capable of initiating tumors in mouse brains, while CD133- were not [42]. Altogether, these papers clarified that the stem cell population confers tumorigenicity to GBM tumors and, moreover, represents the cellular fraction that endows glioma

with radioresistance: in *in vitro* cultures and transplants in immunocompromised mice, CD133+ GBM patient-dedrived cells survive ionizing radiation in increased proportions relative to most tumour cells [43].

This swift historical journey ends up in the omics era. Since the 2010s, with the advent of new technologies for bulk and single-cell sequencing (i.e. next-generation sequencing), a myriad of papers has flooded the scientific literature, providing the community with a tremendous amount of genomic, epigenomic, transcriptomic, and proteomic data that the world has never seen before. The most striking achievement is the The Cancer Genome Atlas (TCGA), a reference cancer genomics program, which molecularly characterized over 20,000 primary cancers. For glioblastoma, this strategy allowed to initially describe a robust gene expression-based molecular classification into Proneural, Neural, Classical, and Mesenchymal subtypes [44]. Aberrations and gene expression of EGFR, Neurofibromin 1 (NF1), and PDGFRα/IDH1 each define the Classical, Mesenchymal, and Proneural subtypes, respectively (Fig. 1.6A). Under therapy, Classical or Mesenchymal subtypes had significantly delayed mortality that was not observed in the Proneural subtype. Afterwards, the 2 most important papers that utilized next-generation sequencing in the field of GBM were published in 2013 and 2014. Brennan and colleagues from the TCGA Research Network, in addition to confirming the 4 subtypes, highlighted the striking inter-patient heterogeneity with an unbiased data analysis of more than 300 GBMs (Fig. 1.6B). The only recurrent mutation is in the EGFR locus, which they deeply characterized in a section of their work [45]. One year later, Patel and colleagues from A. Regev, B. E. Bernstein groups profiled 430 cells from 5 primary GBMs, which, in brief, heterogeneously fell within the 4 subgroups when a mathematical classifier categorized each single expression profile [46]. In other words, this work has shown the intra-patient heterogeneity of GBM: each cell is inherently variable in the expression of transcriptional programs related to proliferation, oncogenic signaling, stemness, hypoxia and immune response (Fig. 1.7). To expand these works, open source glioblastoma biobanks are available and characterized in their molecular subtypes [47].

These and other publications revealed the *multiforms* of GBM tumors in their genomic [48, 49], epigenetic [50, 51] and transcriptomic [52] profiles, which are mutating under therapy [53] and largely maintained when cultured *in vitro* [54]. I have begun the Introduction chapter by providing the 2021 WHO definition of GBM. To

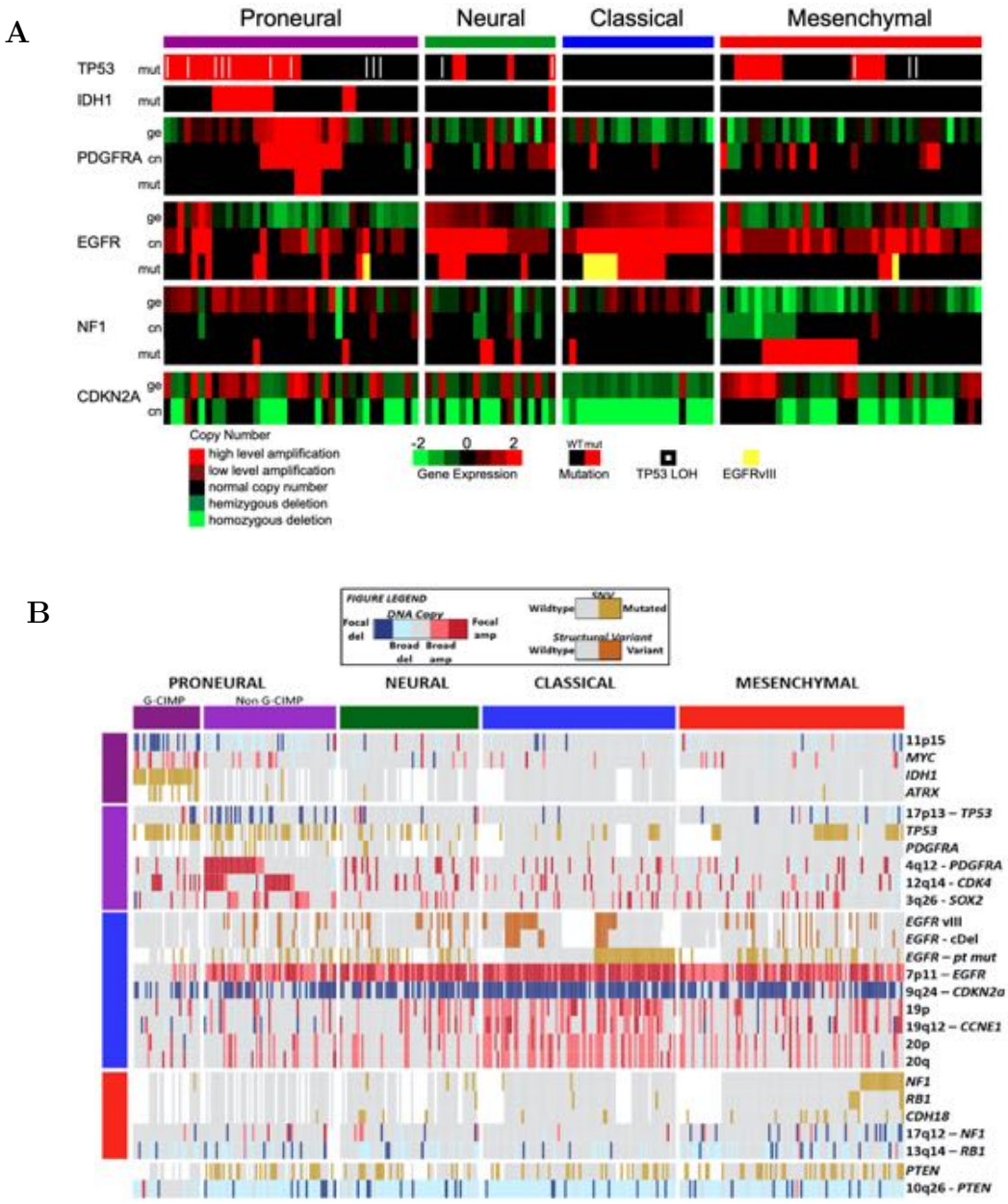

Figure 1.6: Integrated view of gene expression and genomic alterations across glioblastoma subtypes highlights inter-patient heterogeneity. (A) Gene expression data (ge) for 116 patient-derived samples with both mutation and copy number data. Mutations (mut) are indicated by a red cell, a white vertical line indicates loss of heterozygosity, and a yellow cell indicates the presence of an EGFR variant III mutation. Copy number events (cn) are illustrated by bright green for homozygous deletions, green for hemizygous deletions, black for copy number neutral, red for low-level amplification, and bright red for high-level amplifications. A black cell indicates no detected alteration. Adapted from [44]. (B) Genomic alterations and survival associated with five molecular subtypes of GBM - in the proneural phenotype, the Cytosine-Phosphate-Guanine Island Methylator Phenotype (G-CIMP) confers survival advantage. Expression and DNA methylation profiles were used to classify 332 patient-derived GBMs with available (native DNA and whole-genome amplified DNA) exome sequencing and DNA copy-number levels. Adapted from [45].

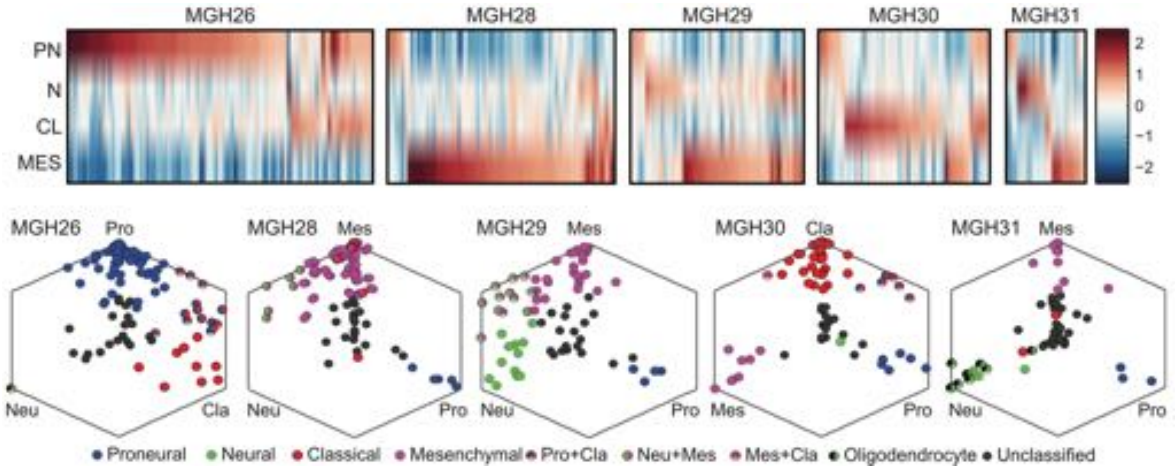

Figure 1.7: Intra-patient heterogeneity in GBM tumors. (A) Heatmap shows average expression of key genes involved in each subtype (rows) between cells grouped by the 5 patient-derived samples (columns). PN: proneural; CL: classical; MES: mesenchymal; N: neural. (B) GBM tumors contain the spectrum of 4 glioblastoma subtypes, as well as hybrid cellular states. Hexagonal plots depict classifier scores for all cells in each tumor. Each point corresponds to a single cell and is positioned along three axes according to its relative scores for the indicated subtype: the more radial its coordinate, the more it belong to the subtype it is pointing to. Cells corresponding to each subtype are indicated by flat color, while two colors represents hybrid cellular states. Adapted from [46].

square it up, two elements - unmentioned so far - require an explanation: Telomerase Reverse Transcriptase (TERT) promoter mutation and +7/-10 chromosome copy number changes [55, 56]. TERT encodes the catalytic subunit of the telomerase complex, and its repression plays a role in cellular senescence by progressively shortening the telomeres. In GBM, the TERT gene promoter is mutated, leading to abnormal cell proliferation [57]. Since the late '80s, the karyotypic analysis human gliomas revealed statistically significant differences in gains of chromosome 7 and losses of chromosome 10 [58].

To sum up, all these results provide a classification far more accurate than Bailey and Cushing for just a subset of brain tumors, yet the most lethal: these observations uncovered a picture that is more and more complicated, branches out in numerous directions and give hints for potential therapeutic solutions to GBM. As we get down to the patient reality, which are the therapies currently used in clinics?

1.1.3 A brief overview on surgery, therapies and survival from the discovery of GBM: where is the state of the art?

The earliest characterizations of brain tumors from the XIX century were followed by the first reported craniotomy in 1884, attempting to remove the tumor [59]. Unfortunately, the patient died after 1 month of meningitis and cerebral fungation. The surgeon, Rickman Godlee, never performed other craniotomies, but he opened up a large debate: were the high mortality associated with surgery, the difficulties in localizing the tumor, and the lack of expertise making the surgery worthwhile [60]? In fact, mortality caused by surgery laid between 33% and 43% up to 1900 - more than 600 operations of *putative* intracranial tumors were performed by 1899: there was no diagnostic tool at the time! So, even the clinicians favorable to surgery were cautious: nevertheless, they had no doubt that the best treatment for brain tumors was resection.

Harvey Cushing, the father of modern neurosurgery, laid out solid foundations through his dedication to technical perfection and publishing his results. Thanks to his work, the 30-day mortality decreased from 30-50% to 6% between 1901 and 1910 [60, 61]. His main contribution concerned intracranial pressure dynamics: he realized that the removal of a small piece of bone in the subtemporal lobe ("subtemporal decompression") as a mean of relief for the patient allowed a safer debulking when tumor resection was possible [62]. Howard Henry Tooth, from the National Hospital in London, published in 1912 the first series describing the pathophysiology and treatment of gliomas in his hospital. Tooth obtained detailed follow-up data from 177 patients over 10 years and reported an average survival of 10.1 months [63]. Notably, he suggested a clinically relevant classification scheme for brain tumors that were correlated with their average survival. This scheme laid the basis for the monograph published in 1926 by Bailey and Cushing (described in section 1.1.1 of this thesis) that, despite being qualitative and was not outlining an official grading system for brain tumors, finally helped surgeons in guiding their operations [22]. When Bailey and Cushing's published their monograph, the surgical community was fighting on the benefits of aggressive operations: Bailey, for instance, was supporting conservative treatments based on internal decompression, biopsy, and radiotherapy, believing that aggressive approaches procrastinated patient's survival *"long after the time when death would be a relief"* [60]. On the other hand, surgeons advocating for aggressive

treatments based on large resections believed that *"simple decompression without removal of the tumor is the worst possible thing to do for spongioblastoma"* [60]. Meanwhile, the introduction of the first diagnostic techniques did not resolve this debate. Ventriculography (an imaging technique based on the injection of contrast media replacing the cavities filled by the Cerebrospinal Fluid (CSF) that determines anomalies in the conformation of the CNS) [64] and angiography (X-ray, contrast-media based imaging that visualizes blood vessels) [65] enhanced the localization of tumors by visualizing the normal brain vasculature and the abnormal one caused by tumors, and surgeons rapidly realized that these tools could help in clinical planning, technique and outcome.

In 1935, Penfield, Elvidge, and Cone, surgeons from Montreal and New York, published the first monograph correlating patient survival with surgery and radiotherapy [66]. Average survival was 1 month without resection and 8.5 months with resection. The addition of radiotherapy allowed 31.8% of patients to survive at least a year and 13.6% beyond 15 months. In a period when other surgeons were performing the first brain hemispherectomies to treat malignant gliomas, this publication raised an additional ethical angle to look at brain surgeries:

"Can the patient after radical removal of the tumor return to his occupation or become an individual capable of taking care of himself, or does he just survive? And if just surviving, [is] ... the operation ... after all worthwhile except for the immediate effects of relieving intracranial pressure? My impression is that we should stop speaking of survival of whatever number of months but qualify it further by saying whether or not the patient is able to return to his active duties or at least take care of himself and not be a burden upon the family". [66]

After WWII the safety of surgical resection improved and became the fulcrum of GBM therapies. Two important multimodality studies established the relevance of the degree of resection and definitively introduced radiotherapy as a surgical adjuvant. In 1960, the results of the study by Roth and Elvidge [67] marked a clear correlation between patient survival and post-surgery radiotherapy (Tab. 1.1), which were confirmed in 1967 by Richard Jelsma and Paul Bucy [68]. Importantly, they introduced dexamethasone (a synthetic glucocorticoid medication used to prevent in-

flammation) as a pre- and postoperative supplement. From 1950 to 1961, operative mortality was 21%, after its introduction mortality decreased to 2.9%.

Therapy	N of patients	Average survival (months)
Resection	144	9.8
Resection + radio	160	17.4
Partial resection	67	8.2
Partial resection + radio	48	17.3
Total resection	93	10.9
Total resection + radio	96	17.4
Inoperable	8	1.4

Table 1.1: Results from the clinical study by Roth and Elvidge (1960) underline the importance of resection and radiotherapy for GBM.

Computed Tomography (CT) and Magnetic Resonance Imaging (MRI) constituted the greatest leap forward in terms of diagnostic tools for treating glioblastoma. After its development in the '60s [69], CT entered widespread clinical use in the '70s. The first time MRI was used to detect GBM was in 1981 [70], and it became widely-available in clinics since the late '80s [60]. In the meantime, during the late '70/early '80s, a series of studies showed positive results for chemoterapeutic compounds (particularly the alkylating agent BCNU, see section 1.1.2) on mean survival of patients with GBM (Fig. 1.8) [71, 72]. From the '90s, the introduction of stereotactic radiosurgery (the disruption of accurately selected portion of tissue utilizing ionizing radiation) and the positioning of biodegradable wafers for controlled BCNU release in the cavity formed upon tumor resection enabled more selective treatments of brain tumors, thus diminishing side effects on the patient [60]. Noteworthy is the introduction of the oral alkylating agent temozolomide, due to its safety profile and low systemic toxicity compared to BCNU: in 2005, Roger Stupp published the results of a phase 3 trial involving 85 institutions and 573 patients that showed that adjuvant temozolomide significantly extended median survival from 12.1 months, with radiation and surgery alone, to 14.6 months [73]. Because of this little achievement, the combined use of surgery, temozolomide and radiotherapy (hence named Stupp protocol) has become the gold standard for the treatment of glioblastoma. Temozolomide, along with BCNU (1977), implantable BCNU wafers (1997), lomustine (an

alkylating chemoterapeutic agent that, being liposoluble, crosses the Blood-Brain Barrier (BBB) and hence can be utilized for brain tumors; 1976), bevacizumab (a VEGF-A inhibitor hampering angiogenesis; 2009), is among the 5 pharmacologic agents that gained Food and Drug Administration (FDA) approval [60].

Nowadays, clinicians are treating glioblastoma with molecular-targeted therapies (whose greatest success is the correlation with a methylated MGMT promoter and longer patient survival [32], see section 1.1.2) and immunotherapies (both passive - involving the administration of *ex vivo* trained cytotoxic cells that target glioma-specific antigens, and active - stimulating the patient immune system to target the tumor) as complementary strategies to the chemo- or radiotherapies, aiming to find an adjuvant/neoadjuvant that is steadily safe and effective.

Many reviews, for example by McCutcheon and Preul [60], comprehensively illustrate the state of the art for GBM treatments. The discoveries in the XXI century are opening up a gigantic amount of solutions that are potentially transferable to clinics: some of them are nowadays granting the patient with circa 20 months of post-surgery survival. Despite we might be a small step closer to the holy grail,

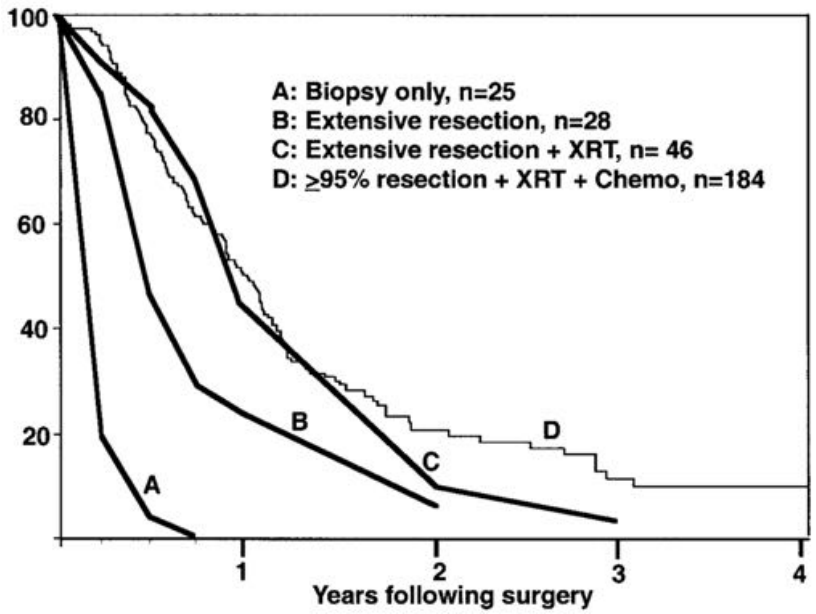

Figure 1.8: Kaplan–Meier survival plots for patients diagnosed with GBM. Curves A,B,C are historical data (1967) from [68], no MRI scans were available at that time. Biopsy only (A), extensive resection (B), and extensive resection followed by radiation therapy (C), data from the M. D. Anderson Cancer Center on patients with 95% resection (by volumetric MRI measurements) followed by both radiation therapy and chemotherapy (D). Adapted from [74].

major challenges remain for curing GBM: paramount is inter- and intra-tumoral heterogeneity (its *multiformity*), and recurrence is still on the podium: most of the therapies fail because GBMs regrow within a 2-cm margin of the resection area [75]. Recurrence is related to the diffusive nature of GBMs, which is fueled by a dominant phenotype that has been neglected so far: cell migration. Among the factors playing a key role in GBM recurrence, one of the most important is cell migration, which is a hot topic of this PhD thesis.

1.2 Importance of cell migration in GBM tumors

While discussing the histological results of his paper from 1938, H. J. Scherer brightly laid out the possibility of GBM migration outside its primary site:

"We have already called attention to the resemblance of certain secondary structures in gliomas to corresponding glial reactions. [...] These resemblances, however, do not indicate the cause or the genesis of these secondary structures. At present, two possibilities suggest themselves. Either there is a neoplastic transformation of the preësxisting glial cells [...], or a selective migration of tumor cells toward these respective preexisting structures." [24]

At that time there was no possibility to visualize cellular dynamics and its evolution overtime, yet, years later, the second possibility turned out to be true. Clinicians were indeed concerned about *"multicentric gliomas"* (i.e. tumors displaying intracranial lesions at several distant locations) since many years [76] and, in light of the frequent recurrences (Fig. 1.9), researchers shifted their interests towards GBM cell migration.

GBM cells rely on a peculiar motility mode to spread. Unlike other solid cancers, they do not intravasate in the lymphatic or blood stream to passively disseminate across organs, but they actively migrate along the pre-existing Secondary Structures of Scherer, which act as topographical cues providing guidance to cell motility [77]. (Fig. 1.4). In particular, GBM cells were found in the subarachnoid space underneath the meninx, along white matter tracts (i.e. thick axon bundles, such as the corpus callosum that connects the 2 hemispheres (Fig. 1.9E)), along the axonal neurons and, most importantly, on the abluminal side of brain blood vessels. It is yet unclear why intravasation events are so rare - it is estimated that less than 2% of GBM metastasize in distant organs [78], but there are several speculations. Firstly, GBM cells might find proper nutrients only within the brain, secondly, they might be unable of breaking the cell-to-cell junctions of the vessell wall, thirdly, patients might not survive enough to visualize GBM metastasis. Then, how do glioma cells interact with their surroundings?

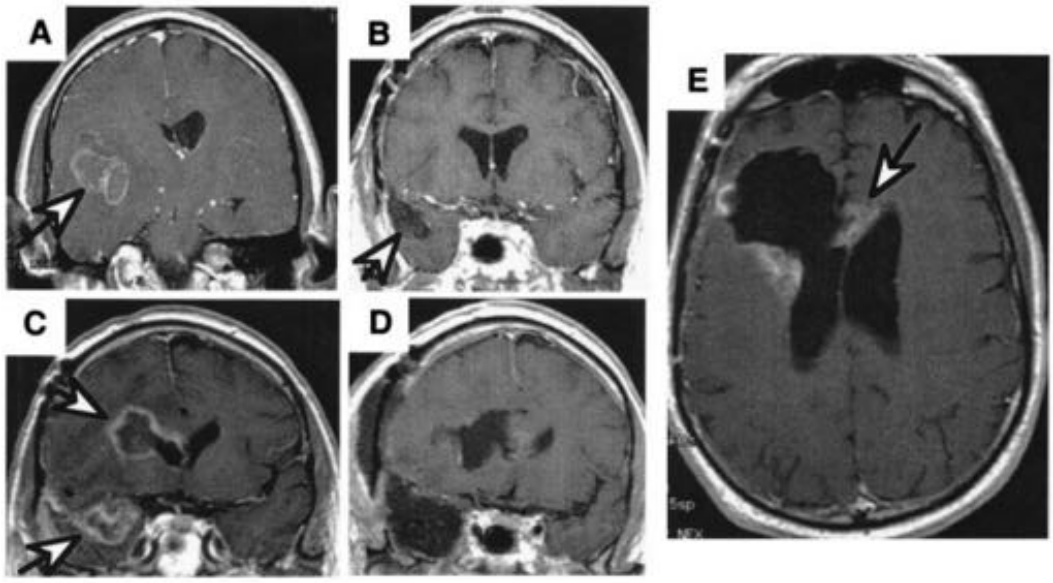

Figure 1.9: MRI scans of a patient affected by GBM illustrating the spread of the disease. (A) Presurgical scan, the GBM tumor is highlighted by the arrow in the left hemisphere. (B) MRI after surgery and radiation therapy showing "gross total resection" and clear resection cavity. (C) 6 months later, MRI showed recurrence both at the resection margin (bottom arrow) and a second GBM lesion (top arrow). (D) Post-resection MRI of the 2 recurrent tumors. (E) Scan 3 months later, showing the tumor recurring at the resection margin (left) and crossing the corpus callosum to the right hemisphere (arrow). Adapted from [74].

1.2.1 The brain parenchyma and its interaction with GBM cells

The brain parenchyma is the functional brain tissue, constituted by neurons and glial cells. These cells are surrounded by ECM: unlike other organs, the brain lacks the stiff fibrillar collagen matrix that constitutes many other compartments in the human body. Being constituted by proteoglycans of the lectican/hyalectan family (heavily glycosylated proteins acting as "backbone") that covalently bind to glycosamminoglycan chains ("functional groups", such as chondroitin sulfate and Hyaluronic Acid (HA)) and other binding partners like tenascins, the brain has a soft, gelatinous consistency [79, 80]. These molecules are secreted by glial cells, particularly by astrocytes and oligodendrocytes, and tightly fill the space surrounding all the brain cells [81]: many of them, like neurocan and brevican (both proteoglycans) and phosphocan (a chondroitin sulfate) promote cell migration [82]. Interestingly, immunohistochem-

istry of *in vitro* cultivated cells and *ex vivo* brain tumor specimens revealed how glioma cells secrete their own ECM that mainly consist of brevican and tenascins, particularly tenascin C [77, 83, 84].

In addition to exploiting the axons and white matter tracts as topographical guidance, glioma cells invade the brain parenchyma through a complex process orchestrated by molecular players that remodel both the surrounding microenvironment and the cell interior compartments. When cells interact with the outside, they attach to the surroundings via integrins, cadherins and neural cell adhesion molecules [77]. Integrins are cell-transmembrane, heterodimeric glycoproteins constituted by 2 subunits, α and β, which are non-covalently linked. 8 α and 18 β chains mix to constitute 24 distinct heterodimers, each having its own specificity for ECM proteins (e.g. laminins, fibronectin, collagen, vitronectin, fibrin) and cell receptors (NCAM,

Cell receptor	ECM/cell ligand	Expression in gliomas
α1β1	Type I and IV collagens, laminin	n.e.
α2β1	Type I and IV collagens	+-
α3β1	Laminins, type IV collagen	+
α6β1	Laminins	+-
α6β4	Laminins	+
α9β1	Tenascins, fibronectin	+
α5β1	Fibronectin	+- / n.e.
αvβ3	Vitronectin, laminin, thrombospondin, tenascins, type IV collagen, osteopontin, periostin	+
CD44	Hyaluronan, type IV collagen	+
ICAM-1	Hyaluronan, LFA-1	+
NCAM	NCAM, L1-CAM, neurocan	-
L1-CAM	L1-CAM, NCAM	+

Table 1.2: Cell-matrix and cell-cell adhesion molecules expressed in glioma cells compared with normal brain tissue. The third column indicates the expression in histopathological samples compared with normal human tissue: +- not altered, n.e. not expressed, + up-regulation, - down-regulation. Related references are indicated in [81]. The top group illustrates key members of the integrin family.

ICAM-1, L1-CAM, and VCAM-1). The key integrins expressed in gliomas are reported in 1.2. For example, the expression of αv subunit negatively correlates with motility, while β1 and α3 positively correlate, with β1 interacting with tenascin C [85, 86]. Furthermore, the dense ECM matrix can be an obstacle to invasion and bare cell adhesion is not enough for invasion purposes. To overcome this, glioma cells express a large number of Matrix Metalloproteinase (MMP) molecules that digest the ECM (for instance MMP1, MMP2 and MMP9) and other proteases like cathepsin-B [77, 85]: *in vitro*, the pharmacological inhibition of MMPs reduced invasion by glioma cell lines and human specimens with malignant gliomas in transwell assays (see section 1.4.4 for the transwell assay) [85, 87]. On the other hand, the actin-myosin complex is a motor that fuels migration from the inside of the cell, along with RhoA/Rac1, CDC42, Arp2/3 and members of the formin family [88, 89, 90, 91, 92]: their activity is coordinated with the aforementioned molecules to provide at the leading edge Focal Adhesion (FA) and ECM anchoring and, lastly, detachment of the cell trailing end [93]. For example, myosin II is essential for the migration of glioma cells through the narrow spaces of the ECM [94], while CD44 (a HA receptor) contributes to glioma invasion in the parenchymal space [95, 96].

1.2.2 The brain blood vessels and their interaction with GBM cells

The brain blood vessels constitute the main partner of GBM cells as they diffuse in the brain [97]. In particular, *ex vivo* studies demonstrated 2 key aspects of this interaction: firstly, bradykinin acts as an haptotactic cue for attraction of glioma cells towards blood vessels; secondly, when injected *in situ*, more than 85% of glioma cells migrate in contact with blood vessels [77, 98]. In the brain, the vascular tree is an incredibly dense network. It is estimated that it is more than 600 km long and covering an area of 10-20 m^2: no cells should be further than 25 µm from a capillary [99]. It is therefore likely for invading glioma cells to meet a branch of the vascular network: when this happens, they face a complex environment made of 2 basal laminae (Fig. 1.10A). The first one is formed by the endothelial cells and the overlying pericytes (cells that directly associate with the abluminal side of vessel tubes), while the second one (absent in capillaries) is constituted by the coupling of astrocytic endfeet with a blood vessel [100]. These basal laminae are enriched of

collagen I,III,IV,V, fibronectin and, most importantly, laminin [101, 102, 103]. Live imaging experiments have shown how migrating gliomas interact with the the blood vessels: as long as cells are in the parenchyma, they show a slow random migration coupled to a multipolar morphology, while they switch to an efficient linear motility coupled to an unipolar elongated morphology as soon as they face an arm of the vessel tree [94, 89, 105, 106]. During this process, glioma cells lift up the astrocytic endfeet, distrupt the continuity of the endothelial wall and the BBB integrity [107], displaying a remarkable plasticity [108] mostly reflected in their hydrodynamic mode of invasion. Infact, *in vivo* imaging of Green Fluorescent Protein (GFP) trensfected

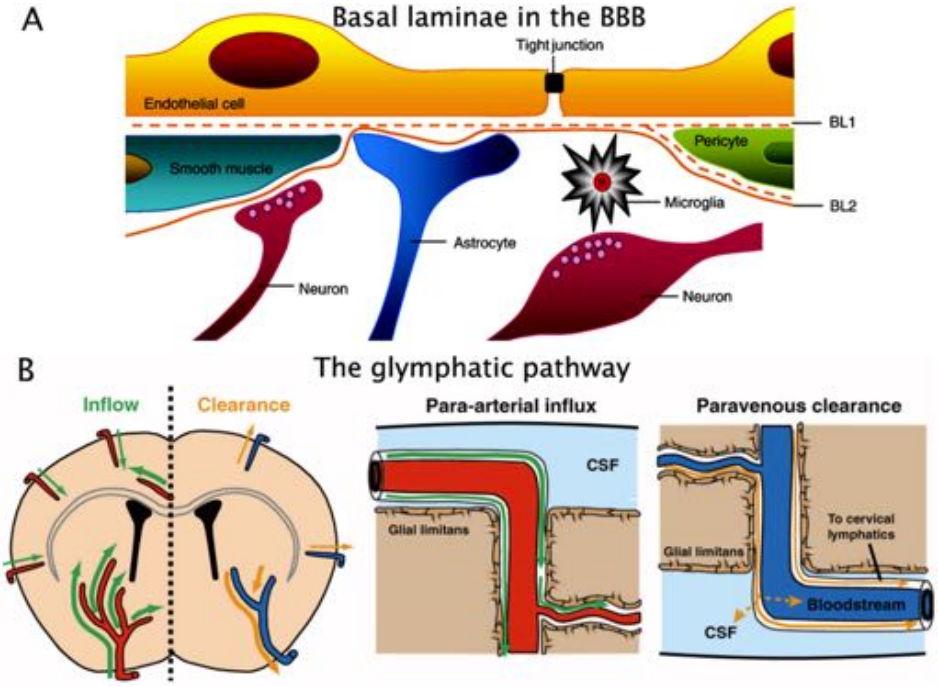

Figure 1.10: Basal laminae in brain blood vessels and schematic depiction of the glymphatic pathway. (A) The cell associations at the Blood Brain Barrier. In blood vessels, endothelial cells form tight junctions. Pericytes are distributed discontinuously along the vasculature and partially surround it. Endothelial cells and pericytes contribute to the local basement membrane which forms a distinct perivascular extracellular matrix (basal lamina 1, BL1), different in composition from the extracellular matrix of the glial endfeet bounding the brain parenchyma (BL2). Adapted from [100]. (B) In the glymphatic pathway, the cerebrospinal fluid (CSF) enters the brain along para-arterial routes, whereas interstitial fluid (ISF) is cleared from the brain along paravenous routes. From here, solutes and fluid may be dispersed into the subarachnoid CSF, enter the bloodstream across the postcapillary vasculature, or follow the walls of the draining veins to reach the cervical lymphatics. Adapted from [104].

cells transplanted in mice shows that they undergo periodic volume changes (as much as $\sim 33\%$) as their shape cycles between extensions and retractions [109].

Noteworthy is the putative interaction of glioma cells with the glymphatic system. The glymphatic system is a recently discovered macroscopic waste clearance system that utilizes a set of perivascular channels to promote efficient elimination of soluble proteins and metabolites from the CNS (Fig. 1.10B). According to this model, cerebrospinal fluid enters the perivascular spaces surrounding brain arteries, mixes with interstitial fluid and solutes in the parenchyma, and exits along perivascular spaces of draining veins [104, 110, 111]. Given that this space provides little physical resistance, the convection provided by this fluid movement might influence glioma migration. However, these are just speculations and the interaction of gliomas with the glymphatic system is yet to be elucitated [77].

1.2.3 GBM migration and stem cells: defining tumor niches

One of the most recent fields of the GBM literature is trying to integrate the importance of cell migration with the notion of GBM stem cells. As I have introduced in section 1.1.2, there is a crosstalk between stemness, heterogeneity and resistance to therapies. However, this crosstalk has to necessarily cope with migration, a hallmark of GBM. To this extent, the concept of GBM niche has become widespread in the scientific community. Niches are anatomically distinct regions fostering not only cancer cells, but also stem cells, feeding them with nutrients and providing shelter from therapies and immune surveillance [112, 113, 114]. Despite some authors have defined up to 5 GBM niches (perivascular, extracellular matrix, periarteriolar, perihypoxic, periimmune) [115], it is more commonly accepted the notion of 3 main niches: the perivascular niche, the invasive niche, and the hypoxic/perinecrotic niche (Fig. 1.11).

The perivascular niche (Fig. 1.11, middle) was the first to be conceptualized and, altough it includes various interaction modalities between blood vessels and tumor cells, its simplest form is depicted by glioma cells expressing nestin and CD133 that are directly associated with CD34-expressing (a cell-to-cell adhesion marker for blood vessel) endothelial cells [116]. The formation of this niche is a dynamic process that could unroll as follows: tumor cells invade along the vasculature in the so called co-option [97], lifting up astrocytic end-feet [107] and producing angiopoietin 1, 2 and VEGF [97, 117]. Finally, tumor cells that are expressing nestin and SOX2 (a

transcription factor for stemness maintenance) transdifferentiate from an avascular to a vascular state [118], also dissociating pericytes from the endothelium and degrading the ECM and the basal laminae. Vessels are thus leaky, dilated and surrounded by fibrin, typical of chronic hyperplasia. The BBB is therefore disrupted, and, being the pericytes dissociated, endothelial cells proliferate abnormally; sprouts of CD34-expressing endothelial cells grow from preexisting vessels: a distorted and irregular vascular tree arises and forms structures that reminds liver glomeruli [112].

Conceptually, the immediate extension of the perivascular niche is the invasive niche (Fig. 1.11, right), which is found in invasion areas showing tumor cell co-option as main mechanism of invasion. In contrast to the perivascular niche, the invasive niche displays a more functional vasculature and is associated with a different and more varied set of host brain cells. A census of the possible cell components, besides tumor cells, would include astrocytes, pericytes, microglia/macrophages, myeloid cells, fibroblasts, and neural stem cells [112, 113, 115, 119]. It is like being at

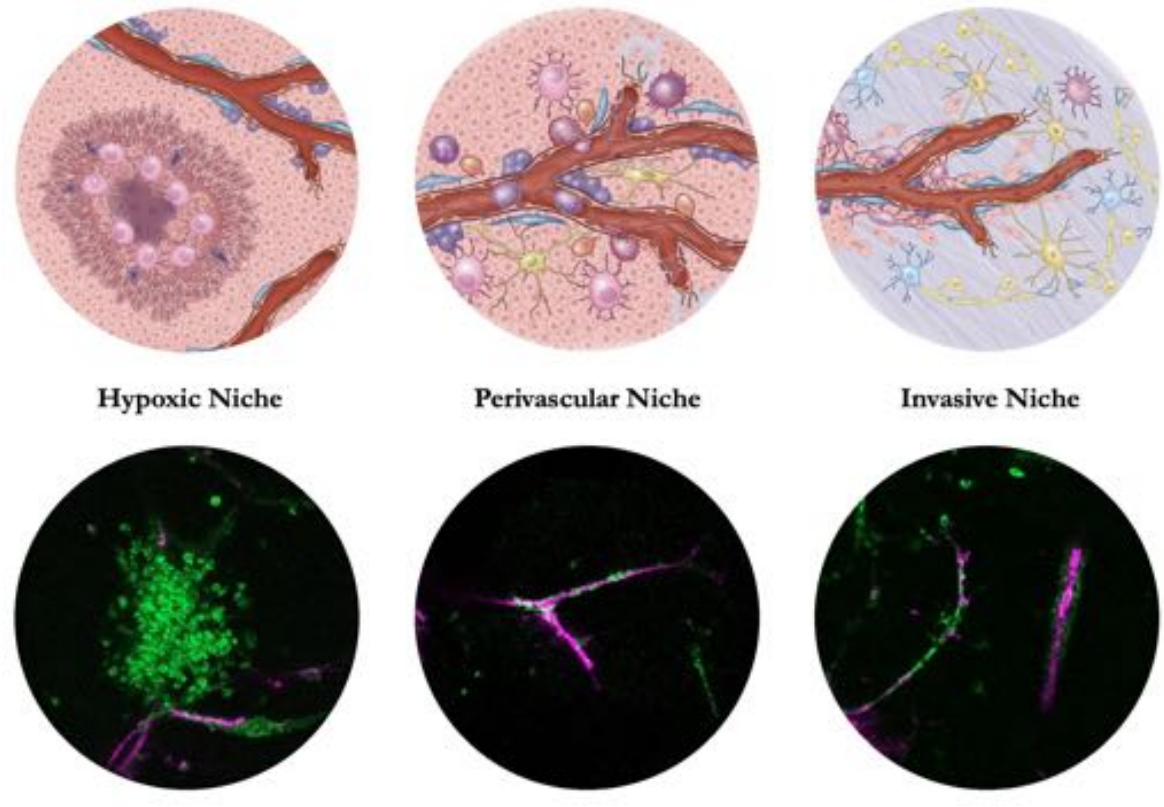

Figure 1.11: GBM migration and stem cell niches. Top: cartoons depicting the 3 main GBM stem cell niches. Bottom: snapshot from time lapse movies of rat C6 glioma (green) that, when overlaid *ex vivo* on murine brain slices (blood vessels are visible in magenta color), form structures reminding the GBM stem cell niches. Top is adapted from [113].

the frontline of an invasion, where tumor cells are not as integrated with the microenvironment as in the perivascular niche.

Finally, Li et al. were in 2009 the first to report the effects of hypoxia and low oxygen levels in GBM stem cells [120]. Exposure to a hypoxic environment induced expression of stem cell markers like SOX2, OCT4 and CD133 in glioblastoma cells, which indicate dedifferentiation of GBM cells into GBM stem cells. It was concluded that a hypoxic niche (Fig. 1.11, left) increased the expression of stem cell markers and of many Hypoxia-Inducible Factor (HIF). Functionally, the expression of HIFs results in production of pro-angiogenic growth factors and therefore induces angiogenesis [121]. HIF-1α and HIF-2α are particularly contributing to the stemness of CD133-expressing GBM stem cells, which morphologically respond to this necrotic environment by elongating their nuclei and aligning like palisades (it is hence common the notion of pseudopalisade as hallmark of GBM tumors [113]) in tidy rows around centers of tumor necrosis. Hypoxia and HIFs are pro-angiogenic factors that, ultimately, drive the transition and the formation of perivascular and invasive niches [115].

1.3 Importance of functional cellular networks in GBM tumors

The last patophysiological trait of GBM that I would like to introduce is a field that spinned-off since 2015 in a landmark study by Osswald and collaborators [122]. It founded the notion that brain tumors, rather than being uncurbed single cells abnormally proliferating or resembling organs that actively interact with their surroundings to grow [123, 124], interconnect into functional and resistant networks capable of extending ultra-long protrusions (up to circa half mm) that foster communication, proliferation, and resistance to therapies (Fig. 1.12).

A brain tumour network is described as a set of glioma cells forming a continuous syncytium that wires up all the members of the network via direct intercellular communication routes. Cells are thus sharing the cytoplasm and directly exchange soluble signals. As schematized in Figure 1.12A,B, during the last years, scientists proposed 2 types of functional networks, namely tumor-tumor networks [122, 125, 126, 127, 128] and tumor-neuron networks [126, 129, 130, 131].

Two main type of cell-to-cell connections have been identified in tumor-tumor networks (Fig. 1.12A): the Tumor Microtubes (TM) and the Tunnelling Nanotubes (TNT). TM are close-ended tubes identified via intracranial 2-photon microscopy of glioma stem cells transduced with fluorescent proteins [122]: they are utilized by the tumor to probe its surroundings, invade them and connect with tumor cells or other cell types such as neurons [126, 131]. On the other hand, TNTs are shorter-lived than TMs, thinner and open-ended [132, 133, 134]. TMs resembles neurite growth cones, which are processes expressed by neurons during development for pathfinding and synapse formation [122, 132]. Growth-Associated Protein 43 (GAP43) is a cytosolic protein expressed in axonal growth cones during neurodevelopment [135] and, intriguingly, it is enriched at the tip of TMs and its knock-down inhibited their formation [122]. When a TM successfully connect with a neighboring cell, this type of junctions are defined as gap junctions and, along with adherens junction, they mediate inter-cellular communication and network continuity [122, 128]. Connexin 43 (CX43) is the protein governing the stability of gap junctions and, when inhibited, brain tumor networks were discontinuous and tumor size was reduced [122]. In particular, the network continuity was assessed by labeling calcium ion and assessing its spontaneous propagation [122, 128].

Furthermore, functional and structural analysis characterized the nature of tumor-neuron interconnections (Fig. 1.12B). They are mediated by glutamatergic synaptic contacts on brain tumour cells that directly bridge glioma cells and neurons. These connections were recorded in about 10–30% of all tumour cells in pediatric and adult glioma types, particularly glioblastomas, both in animal models and in human tumours [126, 131]. These links are always monodirectional: neurons on the presynaptic, and glioblastoma on the postsynaptic side [126, 131]. Links in the other direction have never been reported. Patch clamp experiments revealed excitatory postsynaptic (glioblastoma side) currents relying on the α-Amino-3-hydroxy-5-Methyl-4-isoxazole

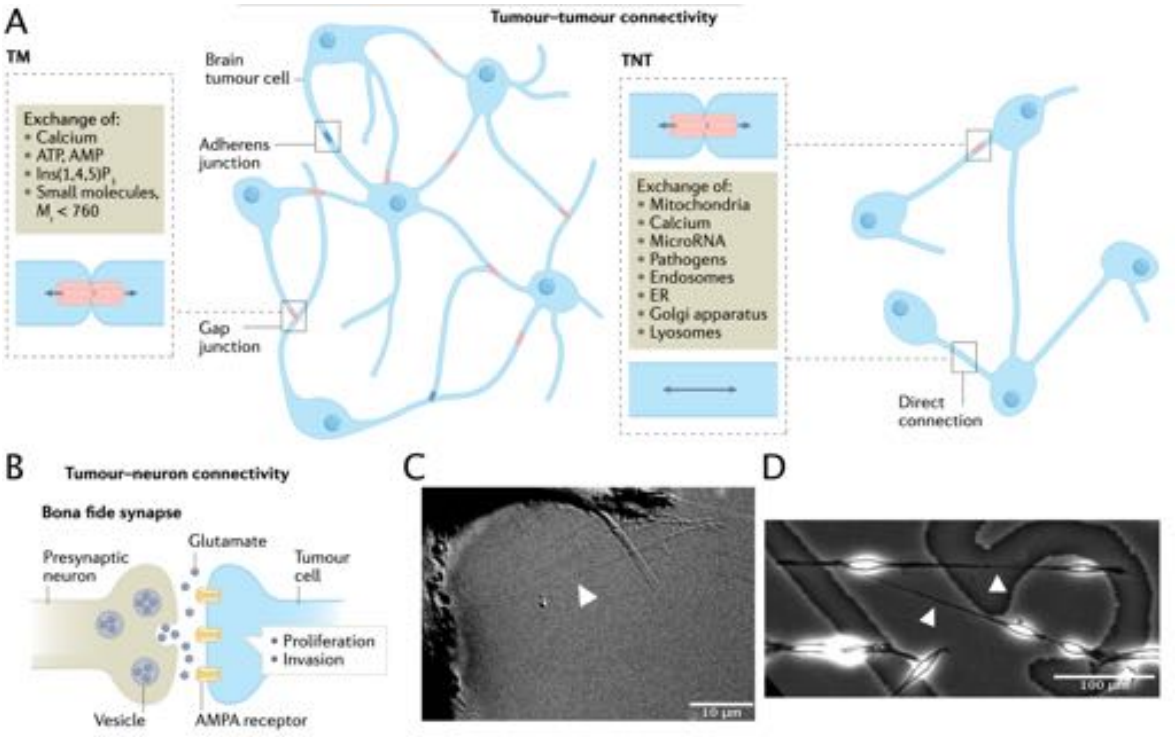

Figure 1.12: GBM tumors form functional and resistant networks. (A) Tumour microtubes (TM, top left) and tunnelling nanotubes (TNTs, top right) form connections having different roles. For instance, organelle trafficking has been recorded only in TNTs. TMs are connected by gap junctions and only small molecules (molecular weight < 760) pass through them. (B) Tumour–neuron junction: bona fide synapses can form between a presynaptic neuron and a post synaptic tumour cell; these are located mostly in TMs, where the neurotransmitter glutamate binds to the postsynaptic tumour cells and stimulates their proliferation and invasion. A,B are adapted from [132]. (C) High magnification Differential Interference Contrast image of patient-derived GBM cells forming structures that remind TNTs (arrowhead). (D) Low magnification Phase Contrast image of patient-derived GBM cells forming structures that remind TMs (arrowheads).

Propionic Acid Receptor (AMPAR). In addition, presynaptic-dependent (neuron side) slow inward currents were detected, hinting plasticity in this type of connections. The biological importance of the glutamatergic synaptic contact was proven with both genetic and pharmacological inhibitions of AMPAR that reduced glioma proliferation and invasion [126, 131].

Altogether, these works prove that GBMs are comparable to functional living organs and that, perhaps, the *reticular theory* sustained many years ago by Golgi for the CNS biology might be relevant, in some sense, to interpret GBM pathophysiology. However, it is still unexplored how the capacity of gliomas to form networks relates with their migration: is the capability to exchange intercellular signals correlated with cell motility? This might be another angle to tackle this disease and new experiments may shed some light on it.

1.4 *In vitro* tools to mimic GBM migration

So far, I have introduced the main pathophysiological traits of GBM, how this tumor integrates ECM and topographical cues provided by the Secondary Structures of Scherer and its capability to thrive as a functional and resistant network. However, how we comprehend the processing and integration of the extracellular stimuli by glioma cells to enable efficient migration strongly depends on the tools and methodologies that we develop. These tools permit us to dissect and replicate such stimuli in controllable and fairly reductionist *in vitro* systems (Fig. 1.13, 1.14). *"What we observe is not nature in itself but nature exposed to our method of questioning"*, wrote German physicist Werner Heisenberg, who figured out the uncertainty related to measurements in quantum physics [136]. Perhaps this concept can be applied in the biology/bioengineering area, in which the field of mechanobiology has significantly jumped in to build devices that mimic *in vivo* contexts. This is achieved by engineering biomaterials and biomimetic devices to accurately research the way glioma motility is affected by specific parameters [137, 138, 139, 140, 141, 142, 143, 144]. In the following section, I will describe which parameters can be tuned to study GBM motility and which have been the tools/devices developed so far to tackle this disease from a motility standpoint: experimental models vary from simple 2D cultures on glass/plastic to orthotopic implants of patient-derived GBM cell lines in immunocompromised mice, and each one has its pros and cons. Broadly, these systems help to tackle the four main extracellular interactions that impact cell migration: ECM composition, mechanical properties, topography/interfaces, and parenchymal cells.

Notably, regardless the *in vitro* system, the biological material utilized influences the relevance of the results. On one side, glioma cell lines (human or murine) established long ago and grown with serum constitutes a benchmarking material that is well-accepted in literature. On the other, they might have lost peculiar traits of native GBM tumors. Therefore, cell lines derived from patient samples and grown as spheroids with no serum are the best biological tool to study the biology of GBM tumors [145].

These cells can be utilized as tumor-spheres or as homogeneously dispersed single cells. Spheroids recapitulate the soluble cue gradients present in tumours, and spheroids with large diameters (> 500 µm) exhibit a hypoxic and sometimes necrotic core [146]. Glioma stem cells should be grown as tumor-spheres and, when the aim is

to use them in this form, this aspect is largely facilitating their manipulation. Adherent cells can be grown as tumor-spheres using microwells or the hanging drop method to aggregate cells into spheroids. Homogeneous dispersion of single cells, which are typically encapsulated during matrix gelation, enables evaluation of single-cell morphology, proliferation and colony growth [137]. Conversely, the use of tumor-spheres keeps a naïve microenvironment, useful to unveil the effects of external biochemical cues and helps in keeping GBM stemness [147].

1.4.1 Bioengineering the extracellular matrix: the role of chemical composition

ECM cues from the brain parenchyma are mostly related to its composition, which I described in subsection 1.2.1. Being the interplay between chemical and mechanical ECM cues two sides on the same coin, in this subsection I will briefly illustrate the former, while in the next one the latter.

The simplest system to study the effect of ECM chemical composition on GBM migration is 2D plastic/glass dishes functionalized with ligands normally found in the brain. It is then easy to coat such dishes with laminin, fibronectin or collagen that are daily used in biological laboratories. Despite this configuration is scalable, amenable to imaging, and can be used to explore cell proliferation, morphology, and motility, it is considered rudimental as it fails to recapitulate the brain architecture [137, 138]. By shifting to a 3D configuration, cells can be embedded in soft hydrogels (Fig. 1.13B), which require them to squeeze or degrade their surroundings. Materials used for 2D, such as collagen (usually isolated and purified from rat tails) [148, 149], matrigel (solubilized after being produced by mouse sarcoma cells) [116, 92] and HA (extracted and dehydrated from bovine vitreous humor) [150], can be employed in 3D setups. Collagen and matrigel are simple to use relative to materials requiring complex synthesis and contain various adhesive sites; however, their composition and the fibrillar nature of collagen do not recapitulate the nanoporous brain matrix rich in proteoglycans and glycosamminoglicans like HA. Additionally, matrigel composition is poorly defined chemically and exhibits batch-to-batch variability [137]. Differently, functionalization and crosslinking of Polyethylene Glycol (PEG) gels with respectively adhesive peptides and cleavable linkers and HA or gelatin-based biomaterials enable precise control over matrix composition [151, 137, 152]: similar studies in this

field showed that porous scaffolds either fabricated with Polycaprolactone (PCL) decorated with HA or with chitosan-alginate maintain stemness in GBM cells [153, 154]. Further studies could evaluate the yet unexplored effects of matrix viscoelasticity on GBM invasion [155, 156]. Other approaches utilize decellularized matrixes from porcine or human patients aiming to be as faithful as possible with respect to the *in vivo* ECM composition [157, 158]. However, protein structure is unavoidably denaturated and the availability of this type of samples is limited.

1.4.2 Bioengineering the extracellular matrix: the role of mechanics and mechanical gradients

The brain parenchyma is a major hindrance for invading glioma cells. In fact, its chemical composition arranges the material in nanopores 38-64 nm wide [159] that cells need to remodel [77, 85] and where they adapt their shape to squeeze through them [94, 109]. In this sense, Magnetic Resonance Elastography (MRE) (a subset of MRI that non-invasively extrapolates mechanical properties from tissues) measurements pinpointed the brain as a viscoelastic material [160] with a young's modulus ranging from hundreds of Pa to circa 10 kPa, with an average of 3 kPa [161]. Interestingly, atomic force microscopy data from inner limiting membranes (located at the retinal-vitreal junction and utilized *in vitro* as a CNS vasculature model) suggested that stiffness is higher at the perivascular region compared to the parenchymal side, hinting that a durotactic cue might guide glioma migration towards it [162]. Indeed, glioma migrate faster on stiffer fibronectin-coated polyacrylamide and 3D HA gels than on soft ones when seeded on flat surfaces with a precisely defined Young's modulus [152, 163]. Moreover, tumors remodel their surrounding environment and they generally increase its stiffness [140, 137] and, as the tumor grows, the area around it is confined and the intracranial pressure increases [140, 164].

The simplest system to bioengineer some of these mechanoproperties is the transwell (Fig. 1.13C). It consists of a porous membrane inserted in a multiwell plate that allow to study the capacity of cells to squeeze through it, mimicking the narrow pores in the brain parenchyma. In the case of GBM, it was utilized to validate how myosin II is necessary to successfully cross the membrane [94]. Other tools are the fabrication of surfaces made of synthetic Polyacrylamide (PA) gels [165, 166], silicone rubber [167] or Polydimethylsiloxane (PDMS) [168] featuring different physi-

ologically relevant stiffness (Fig. 1.13A). These materials can be coated with proteins contained in the brain, like laminin, collagen, or fibronectin. Cells can also be embedded in collagen or HA-based hydrogels whose stiffness is tunable by diluting the initial solution in known ranges (Fig. 1.13B). Certainly, these approaches can be elaborated with the functionalization or cross-linking of different peptides, as illustrated in the previous subsection, and engineered to reproduce stiffness gradients both in 2D and 3D [137, 169]. For example, microfluidic mixing of HA and gelatin precursor solutions at different concentrations results in 3D gelatin–HA gels with gradients of crosslinking density, in HA content (that ultimately modulated MMP9 expression) and, subsequently, in cell density [170]. 3D gels are usually attached to a glass surface, which causes a stiffness gradient along the Z axis: cells closer to the coverslip (tens of µm) navigate in a stiffer environment than those at the top of the gel (fractions of mm) [171]. This approach may also generate soluble chemical gradients, since an elevated hydrogel thickness exposes the cells to a low-nutrient, hypoxic environment, triggering the expression of VEGF, HIF-1 and a pro-angiogenic phenotype [172]. Therefore, these bioengineering platforms can be applied to study how GBM progression is affected by ECM composition, mechanics and soluble cues.

1.4.3 Bioengineering interfaces and topographical cues: the role of blood vessels and white matter tracts

As illustrated in section 1.2, glioma cells invade the brain along the Secondary Structures of Scherer that provide topographical guidance [2, 89, 97, 105, 106]. In particular, white matter tracts are arranged as tens-of-microns long fibers with diameters in the range of few microns/fractions of micron, while brain blood vessels are tubes whose diameter roughly spans between 5 and 50 µm [99, 100]. These structures are embedded within an ECM, thus forming an interface between 2 composite layers [80, 77, 137].

The concept of 2.5D materials is a peculiarity that characterizes the way this type of interfaces are engineered. 2.5D materials are formed by a 3D topology that is the result of interfacing multiple 2D topologies. In other words, a 2D pattern is initially fabricated and then some 3D-like constraints are applied. For example, Gritsenko and collaborators engineered an interface where glioma spheroids were spreading on an astrocyte monolayer that was confined in a soft hydrogel [173]. This setup

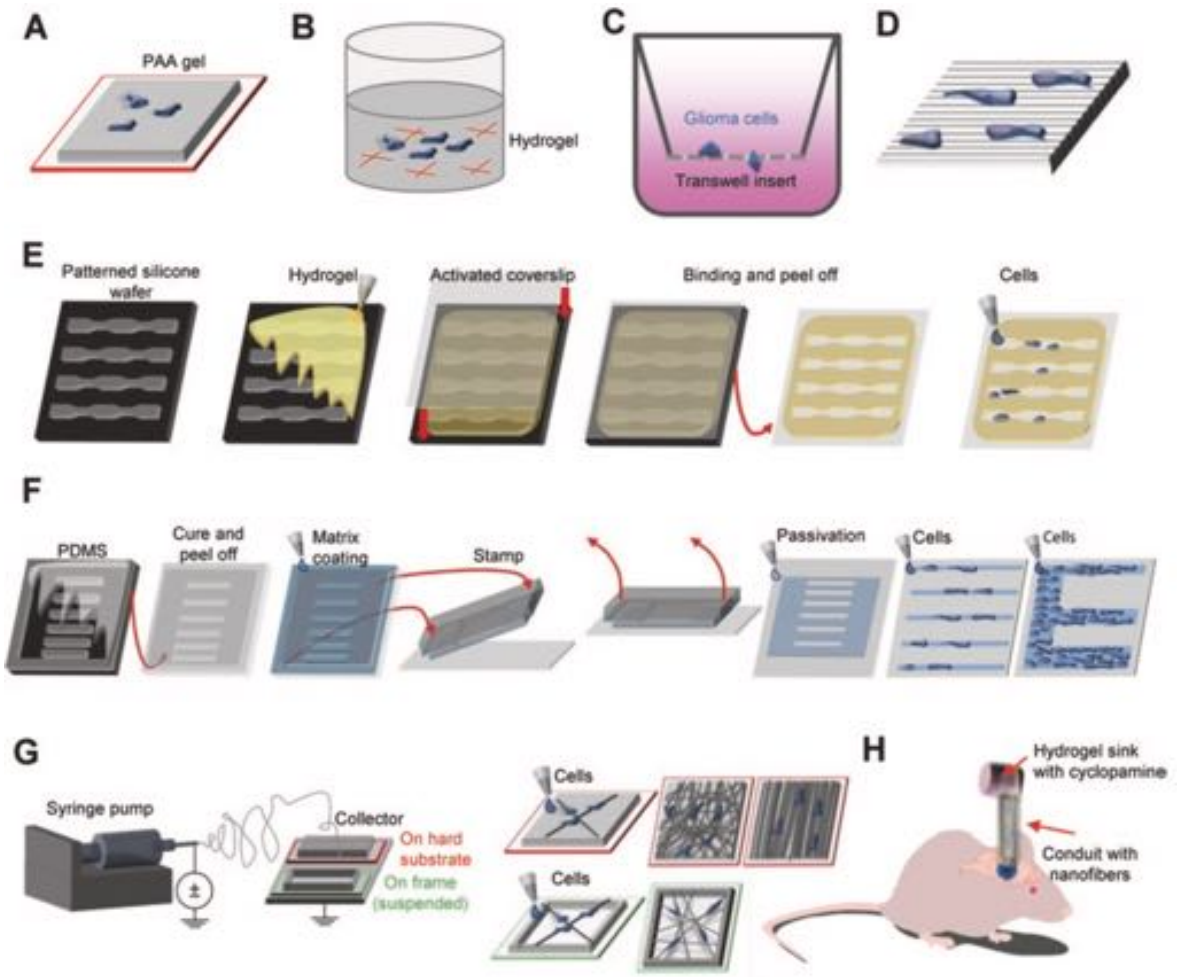

Figure 1.13: Overview of different mechanobiology techniques used to study mechanochemical and topographical cues for glioma motility. (A) 2D hydrogels to study the effect of substrate rigidity: cells are plated on top. (B) 3D hydrogels to study the effects of substrate rigidity and chemical composition: cells are embedded. (C) Transwell system to study chemoattraction and motility through a 3D matrix with known pore sizes. (D) Linear grooves to mimic white matter tracts. (E) Microchannels are obtained with soft litography and used to mimic blood vessels and white matter tracts upon confinement. (F) Microcontact printing to mimic blood vessels and white matter tracts. (G) Nanofibers obtained with electrospinning are used to mimic white matter tracts. They can be suspended or leant on a substrate. (H) Nanofibers in a device are coated with laminin and used to build up a glioma trap: when the device is implanted through the mouse skull, nanofibers attract glioma cells in a sink loaded with a cytotoxic drug. Adapted from [138].

simulated intraparenchymal invasion. A similar configuration can be obtained by sandwiching tumor cells between 2 hydrogel layers [174]. Engineering models of anatomical tracks typically include a linear, topographical feature on a 2D surface or encapsulated in a 3D matrix. Microchannels can confine the cells in narrow spaces

that model how they invade squeezing along a Scherer structure. In particular, microchannels were molded in a PA gel of a known stiffness to show how it synergizes with confinement to promote rapid movement of GBM cells (Fig. 1.13E) [175]. Alternatively, nanofibres can be used to study how aligned topographical guidance resembling the cues provided by white-matter tracts impacts of GBM migration (Fig. 1.13G). Interestingly, aligned fibres strongly promote rapid, linear migration [176, 177, 178, 92]. Nanofibers can be multilayered, with a core whose composition can be tuned to reproduce different mechanical properties, and the shell that provides a peculiar surface chemistry [177]. They can be also embedded in 3D gels: in Matrigel, when tumor cells encounter a fiber, they switch migration mode towards a faster and invasive phenotype [179]. Notably, nanofibers were used to build up a trap to kill U87 glioma cells *in vivo* (Fig. 1.13H). A conduit containing aligned, laminin-coated nanofibers was inserted inside the brain of glioma-bearing animals. The fibers were leading to an external sink filled with a collagen gel loaded with a cytotoxic compound: U87 cells were attracted by the fibers and migrated from the tumor core towards the external sink that successfully killed them [180].

To mimic topographical cues, one of the most straightforward techniques is micro-contact printing [168]. It allows to imprint proteins with a desired spatial geometry that, in GBM case, reproduce vessels of different diameters (Fig. 1.13F). We utilized this technique to show how cell density triggered antiparallel streams dependent on the formin FHOD3 in rat C6 cells seeded on stripes with various widths [91] and to show invasive behaviors dependent on the formin FMN1 in discrete populations of patient derived GBM seeded on gridded micropatterns. [92]. Linear grooves can be also utilized to study the influence of topographical linear guidance (Fig. 1.14D): in some studies, glioma cells (C6, U87, primary GBM) aligned and moved along the axis of the grooves, a phenomenon called contact guidance [181, 182, 183]. This technique has been proposed as clinical prognostic platform [181]. In another work, backside lithography was used to fabricate a tapered geometry that closely reminds the three-dimensionality, curvature and tubular structure of blood vessels [184].

Several methodologies combined the modeling of the BBB interface and the topographical linear cues provided by blood vessels. Hollow fiber tubes (Fig. 1.14B) allow to study the impact of shear stress on endothelial cells, monocyte extravasation in the brain, or drug screening [185, 186, 187]. Other techniques, relying on sacrificial layers, can be utilized to accurately bioengineer blood vessel (Fig. 1.14E-H): the idea

is that, once a hollow cavity is formed - typically within a soft gel - by sacrificing a removable material, endothelial cells are seeded to form an *in vivo*-like lumen. With single vessel patterning in soft matrices (by just removing a micro-rod once the hydrogel polymerized, Figure 1.14E) scientists studied invasion, intravasation of cancer cells and brain microvasculature disruption [188, 189, 190, 191]; viscous fingering (Fig. 1.14F) allowed live cell studies with a geometry really close to *in vivo* vessels [192, 193, 194]; thanks to micromolded vessel networks (hollow microchannel networks are patterned between two collagen layers, Figure 1.14G) angiogenic and thrombotic phenomena were studied [195]; a 3D printed carbohydrate glass that is dissolved via the chemical interaction with cell culture medium permitted to customize vessel geometry as a 3D network of hollow cavities inside a soft gel (Fig. 1.14H), which was lately seeded with endothelial cells [196]. In addition to techniques based on sacrificial layers, blood vessels can be 3D printed [197], or organotypic microvascular networks can be formed by Human Umbilical Vein Endothelial Cells (HUVEC) seeded in fibrin gels using microfluidic platforms (Fig. 1.14I) [198, 196] that included a functional BBB model as well [199].

In conclusion, several works showed that (non-)sophisticated techniques permit to decipher several chemo-mechanical interactions between GBM and Scherer's Structures and, in particular, that topographical cues intensely drive invasion and motility modes in GBM cells, which can be enhanced by other environmental signals, such as ECM composition and mechanics.

1.4.4 Bioengineering co-culture systems: the role of parenchymal cells

The most easy-to-use system to study the influence of parenchymal cells on GBM migration is the already mentioned transwell system (Fig. 1.14A). It can be used to study the chemotaxis of glioma cells toward a given attractant: for example, murine glioma initiating cells and patient-derived GBM stem cells were attracted towards endothelial cells or endothelial cell conditioned medium seeded on the bottom side of the insert [200, 201].

Gritsenko and collaborators from the group of P. Friedl showed how GBM spheroids spread at different paces onto monolayers of astrocytes cultured for different times, which may influence ECM accumulation or changes in astrocyte pheno-

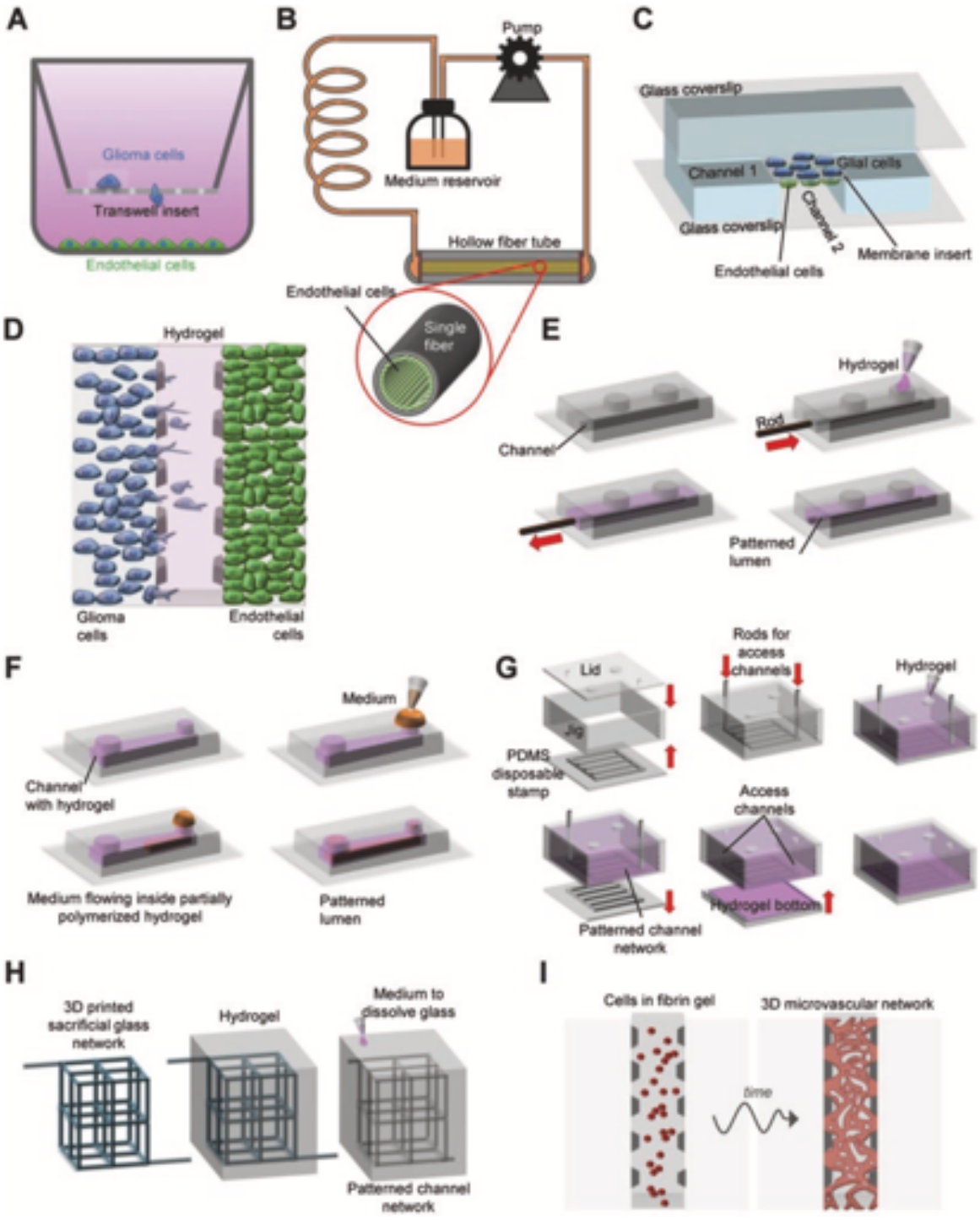

Figure 1.14: Overview of different mechanobiology techniques used to study how interfaces and co-culture systems affect glioma motility. Full caption in the next page.

type [173]. Co-culture settings similar to the transwell system can be engineered with microfluidics, which allow a tight control on mechanical, biophysical and chemical parameters: the influence of parenchymal cells such as astrocytes, pericytes, neurons and endothelial cells on GBM migration can be studied either by inserting membra-

Figure 1.14 Overview of different mechanobiology techniques used to study how interfaces and co-culture systems affect glioma motility. (A) Modified transwell system for co-cultures and chemoattraction: endothelial cells are below the insert, glioma on top and need to cross it. (B) Dynamic *in vitro* model utilizing hollow fiber tubes seeded with endothelial cells to recreate a blood vessel structure. (C) vessel-like microfluidic channels. The presence of a polymeric membrane mimics the vessel-parenchyma interface. (D) Compartmentalized microfluidic devices. (E) Patterning single vessels in an hydrogel matrix utilizing a removable microrod: the hollow cavity can be filled with endothelial cells. (F) Patterning single vessels in an hydrogel matrix utilizing viscous fingering. (G) Micromolded vessel networks. The cubic device is filled with an hydrogel that, once polymerized, leaves cavities as the disposable PDMS feature is peeled off from the bottom and replaced with a substrate. (H) 3D printed vessel networks. The 3D printed sacrificial layer is made of a bioengineered glass that dissolves in acqaueous media, leaving cavities in the hydrogel. (I) Organotypic microvascular networks. HUVECs self assemble into 3D microvascular nwtworks when embedded in functionalized fibrin gels. Adapted from [138].

nes that mimic vessel-to-parenchyma interface (Fig. 1.14C) [202], or by creating several compartments in the microfluidic chip (Fig. 1.14D) [199, 200] that can be scaled up in multiplexed devices [203]. Truong and collaborators showed that, in a compartmentalized microfluidic devices having 3 radial channels, GBM invasion from the inner channel is increased when endothelial cells were seeded in the outermost channel [204]. Similarly, a device with three parallel channels was conceived to study what happens to GBM cell in the presence of a vaso-occlusive event. The outside channels contained flowing medium and the centre channel contained a 3D matrix with homogeneously embedded GBM cells. As the flow was interrupted in a side channel to simulate vaso-occlusion, the resulting hypoxic gradient forced GBM tumour cells to migrate away from the occluded channel and form pseudopalisades [205]. Other co-culture systems that study the effect of necrosis and GBM migration in the presence of endothelial cells can be obtained with bioprinted, decellularized ECM containing embedded cells [158].

Eventually, glioma stem cells can be stimulated to grow as organoids that integrate several cell populations, recapitulating the original microenvironment. This is an approach opposite to the tight control that microfabrication techniques permit, since every cell population is free to spontaneously grow. Millimetres-sized, tumor-

like aggregates are thus obtained over the coarse of few months [147]. These methods permit to keep the original heterogeneity and the proportions of GBM cells versus the parenchymal ones and recapitulate well hypoxic gradients and the complexity of the native microenvironment. However, they fail in modeling GBM migration. It is indeed tough to get structures such as blood vessels and white matter tracts, other than being time-consuming and hard to scale up.

1.5 Hypotesis and goal

Since the late '90s/mid '00s microfabrication and mechanobiology techniques allowed scientists to fabricate a multitude of devices [141, 168]. With these devices the influence on GBM of many mechanical, chemical, topographical, cytological parameters was studied in great detail [137, 138].

During the course of this PhD thesis introduction, I have illustrated how cell migration [77, 140] and population heterogeneity [45, 46] play a crucial role on the recurrence of GBM tumors [43, 76] and why, therefore, it is important to tackle migration with biologically relevant samples that resembles as much as possible the original tumor [145, 147]. While migrating, GBM cells interact with topographical cues that serve as linear guidance, namely the Secondary Structures of Scherer [2]. Among these, the largest interaction seems to appear with the blood vessels: their abluminal side is exploited as invasive highway to colonize the whole brain [97, 98, 105].

However, how the interplay between diffusion and heterogeneity impacts on GBM migration is unclear: the holistic dissection of GBM migration with a fairly reductionist device that might be scalable and comprehend an imaging and analysis workflow that delivers quantitative outputs on cellular migration (i.e. the directed movement of a single cell or a group of cells in response to chemical and/or mechanical signals) and motility modes (i.e. the biophysical features that single cells and/or pools of cells adopt while migrating: shape, polarity, persistence, cell-to-cell interactions...) is the gap of knowledge that this PhD work aimed to fill. Indeed, integrating the pre-existing brain structures in a reproducible and 3D-like system often precludes optical accessibility, time profitability and analytical workflows. With the help of all the other members of Gauthier and Maiuri labs I developed SP2G, an easy, time-profitable method that integrates live cell imaging with a dedicated analysis workflow for comprehensively characterizing GBM migration and motility modes. This work has spinned off from the last publication of our lab, *"Adaptive mechanoproperties mediated by the formin FMN1 characterize glioblastoma fitness for invasion"*, which was accepted during the course of my PhD [92]. The imaging section of SPheroid SPreading on Grids (SP2G) indeed combines the gridded micropattern we proposed in [92], which resembles the network of topographical linear cues provided by the vasculature, with patient-derived spheroids that maintain GBM stemness and het-

erogeneity. The cells in the spheroid progressively spread out onto a naïve substrate allowing the study of cell-to-cell interconnections and GBM networks, which is another crucial feature of this tumor [122, 132]. SP2G analytical toolbox quantitatively describes GBM migration through area expansion, diffusivity, and boundary speed; and motility modes through collective migration, directional persistence, and hurdling. In this work I have kept the heterogeneity of the original tumors utilizing patient-derived samples maintained as GBM stem cells and, surprisingly, I found how heterogeneity in GBMs is reflected in cell migration and motility modes and I deeply characterized them using SP2G.

Chapter 2

Results

2.1 Spinning off from *"Adaptive mechanoproperties mediated by the formin FMN1 characterize glioblastoma fitness for invasion"*

This section includes results obtained in the first part of my PhD that were published in the paper *"Adaptive mechanoproperties mediated by the formin FMN1 characterize glioblastoma fitness for invasion"* [92]. In this work, I have contributed as second author and, among others, I brought expertise in 3D spheroid embedding assay and brain slice overlay assay which, despite having their own relevance, they were quite complicated and low-throughput *in vitro* setups for studying cell motility and invasion. Thus, they made us think on a spin-off work that could efficiently and systematically tackle GBM migration alone.

Most importantly, in this work we introduced the gridded micropattern as a mimicry of the brain blood vessel network (Fig. 2.1). Given that the vasculature represents the main topographical stimulus for glioma migration, the rationale that was followed in designing the grid was to reproduce the capillary network (width of the grid segment is 7 µm, similar to small capillaries; length is 75 µm) with a fairly reductionist pattern that could give decipherable cues for cell migration. In the lab, micropatterning techniques were well established and the use of linear stripes was utilized to study migration of rat C6 glioma cells [91]: the next move has been to superimpose 2 perpendicular sets of lines to create a grid.

In [92] we have introduced 3 GBM cell lines (namely NNI-11, NNI-21, and NNI-

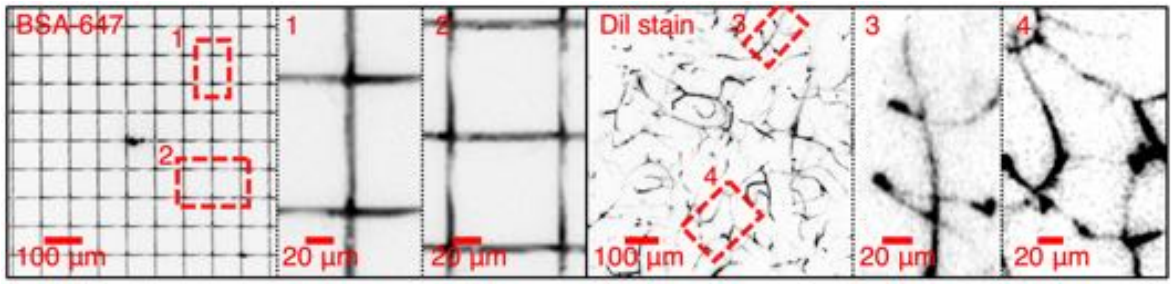

Figure 2.1: Gridded micropatterns mimic the brain blood vessel network. Pictures highlighting similarities between the laminin gridded micropattern (left, fluorescence is given by BSA-647 mixed with the laminin solution) and crisscross features in murine brain vasculature from ex vivo organotypic brain slices (Dil dye, intracardial injection). Each grid segment is 75 µm long and 7 µm wide.

24) isolated from patients and selected for their different invasive and proliferative behaviors, which were previously shown to be IDH-1/2 wild type [206, 207]. In xenografts, the NNI-11 developed tumors that were circumscribed and fast growing. In contrast, the 2 other cell lines, NNI-21 and NNI-24, were more diffusive: on microprinted lines they adopted a similar behavior, while on the grid the difference was striking: as the NNI-24 migrated persistently (i.e. with no changes in directional movement) and smoothly stuck to the micropattern, the NNI-21 adopted a stochastic and jumpy motion and frequently cut grid corners. The NNI-24 were hence named *gliders*, the NNI-21 *hurdlers* (Fig. 2.2A). Importantly, these cell lines were then used as a benchmark when validating SP2G.

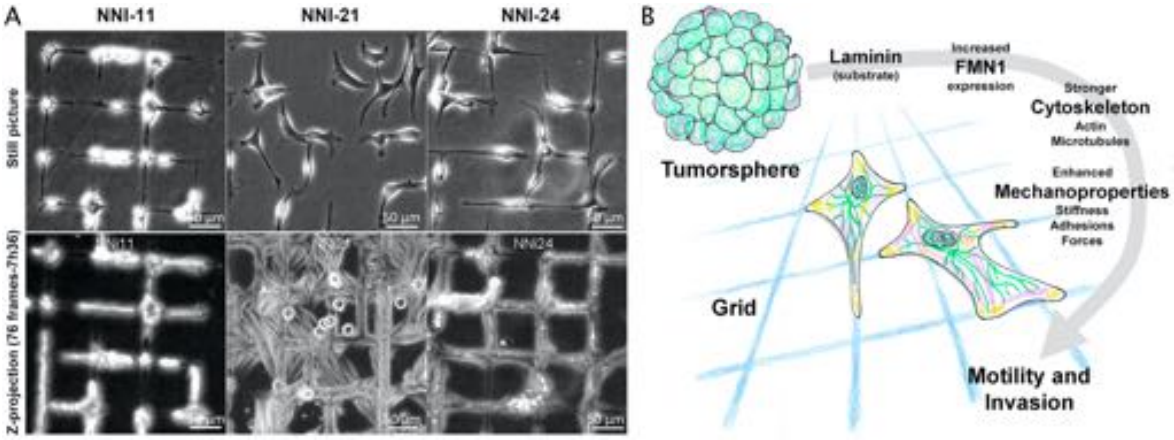

Figure 2.2: Motility on grids of patient-derived GBM cell lines. (A) Up: typical snapshot of NNI cell lines migrating on grids; down: time projections. (B) Summary of the findings in [92].

Briefly, the main findings of this work are summarized in Figure 2.2B: in the

most-motile cell line NNI-21, an increasing concentration of the laminin substrate induced an increasing expression in the formin FMN1 that, by regulating GBM mechanics from the microtubule lattice, enhanced the cell mechanoproperties (higher traction forces and cell's Young modulus, more higher number of focal adhesions). The enhanced mechanoproperties finally led to invasive motility and boosted cell migration, thus making the NNI-21 more fit for invasion. Conversely, the cell lines NNI-11 and NNI-24 developed lower mechanical forces on the substrate and were softer. In this paper, the phenotype caused by the formin FMN1 was studied with

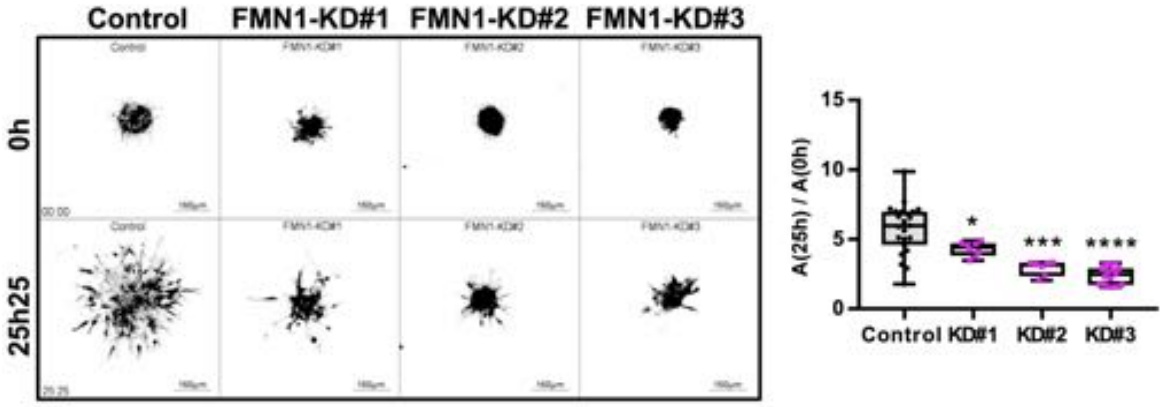

Figure 2.3: Spheroid embedding as validation of motility phenotypes. Analysis of movies of control and FMN1 knockdown spheroids invading matrigel: Z-projection of the GFP signal at time 0 (left, up) and 25 h 25 min (left, down). Quantification of area invaded by the cells (n = 23, 8, 7, and 15 spheroids). Error bars are Standard Error of the Mean (S.E.M.).

various migration/invasion assays, among which the spheroid embedding in 3D matrigel (Fig. 2.3) and the brain slice overlay assay (Fig. 2.4: here, spheroids were loaded on top of a brain slice that was cut *ex vivo* from a murine brain). We acquired time-lapse movies of control and spheroids knocked down with 3 Short Hairpin RNA (shRNA) embedded in matrigel over 25 h by confocal microscopy. In matrigel, control cells were moving rapidly, escaping of the spheroids, whereas FMN1-knockdown cells were trapped in the spheroids, protruding and retracting cell processes (Fig. 2.3). To further nail that FMN1 potentiated single-glioma-cell motility along blood vessels in the brain, spheroids were loaded on murine brain slices (Fig. 2.4A). As previously observed with other glioma cells [105], control single cells were moving in the brain tissue following linear tracks that were identified as blood vessels by immunofluorescence (Fig. 2.4B). At the opposite, knockdown cells were moving poorly (Fig. 2.4A), confirming that FMN1 promoted glioblastoma migration along brain

blood vessels. Altogether, these assays were meaningful for studying glioblastoma migration and they helped us to decipher the phenotype dictated by the formin FMN1. However, they lack some key aspects that led us to develop SP2G a simplest and more comprehensive methodology.

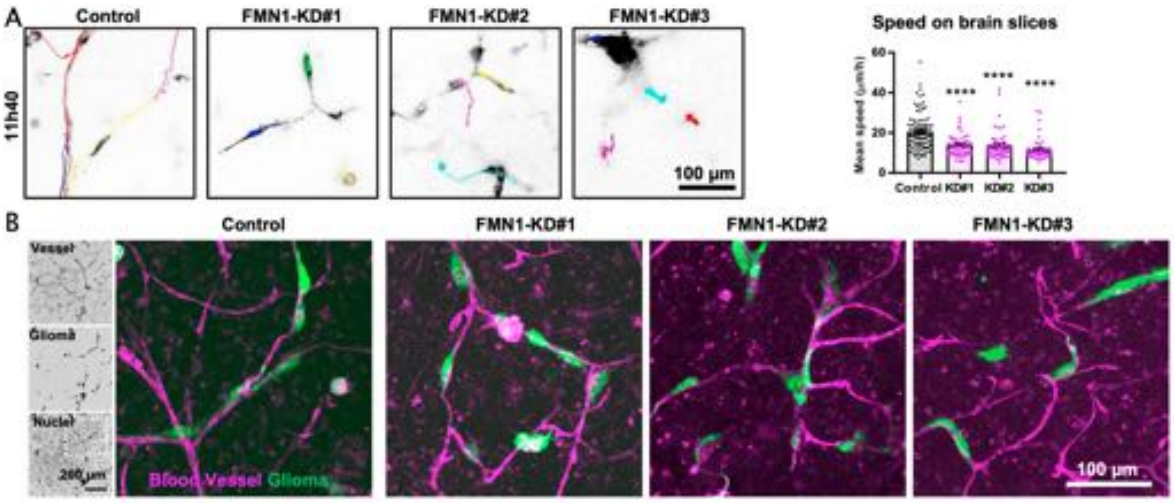

Figure 2.4: Brain slice overlay assay as validation of motility phenotypes. Analysis of movies of control and FMN1 knockdown spheroids invading brain slices. (A) Overlay of the manual tracks and the last image of the movie (left). Average of mean speeds (n = 95, 56, 56, and 55 tracks). Error bars are S.E.M. (B) Confocal images of *ex vivo* murine brain slices invaded by glioma cells (green, GFP) fixed and stained for tomato lectin (magenta) to label the blood vessels.

2.2 SP2G mimics glioblastoma invasion on brain blood vessels

The 3D spheroid embedding assay and brain slice overlay assay were poorly efficient in some aspects:

- ✘ 3D hydrogels lack anatomical cues essential for migration of gliomas;
- ✘ both the approaches are hard to scale up, reproduce, and are time-consuming;
- ✘ in both systems, optical accessibility and, in turn, quantification of biophysical parameters are often flawed;
- ✘ there are ethical issues when utilizing mice.

To tackle these cons and build up SP2G as a novel methodology, we decided to combine the grid micropattern with spheroids. As introduced in section 1.4, the use of spheroids leads to many advantages:

- ✓ bridges the gap between 2D and *in vivo* conditions;
- ✓ permit to study transitions from an aggregate to invasive cells;
- ✓ permit to study collective cell interaction;
- ✓ keeps stemness of GBM cell line;
- ✓ minimize manipulation for GBM stem cells as they are routinely kept in culture as suspended spheroids.

As spheroids are loaded on the gridded micropattern, the way they spread (SPheroid SPreading (SP2)) can be utilized as a proxy to study GBM migration and motility modes. To validate our SP2G assay, we surveyed 3D and 2D techniques where vessel-like topographical cues were present or not (Fig. 2.5). For this survey, we used rat C6 glioma since these cells migrate efficiently on host brain vasculature and, in literature, are a well-accepted benchmarking glioma cell line for validation purposes [105, 208]. We imaged SP2 in 5 different settings: mouse brain slices (Fig. 2.5A) [209], 3D hydrogels (6 mg/ml collagen I and 10 mg/ml Matrigel, Figure 2.5B,C respectively) [148], 2D flat substrates (coated dishes, Figure 2.5D) and gridded micropatterns (SP2-G, Figure 2.5E). Both, 2D flat substrates and gridded micropatterns were coated with laminin (10 and 50 µg/ml, respectively). As observed in Figure 2.5A-E, spheroids spread faster on 2D flat and gridded micropatterns (circa 8h for complete dissolution of the spheres) compared to 3D gels (> 24 h) and brain

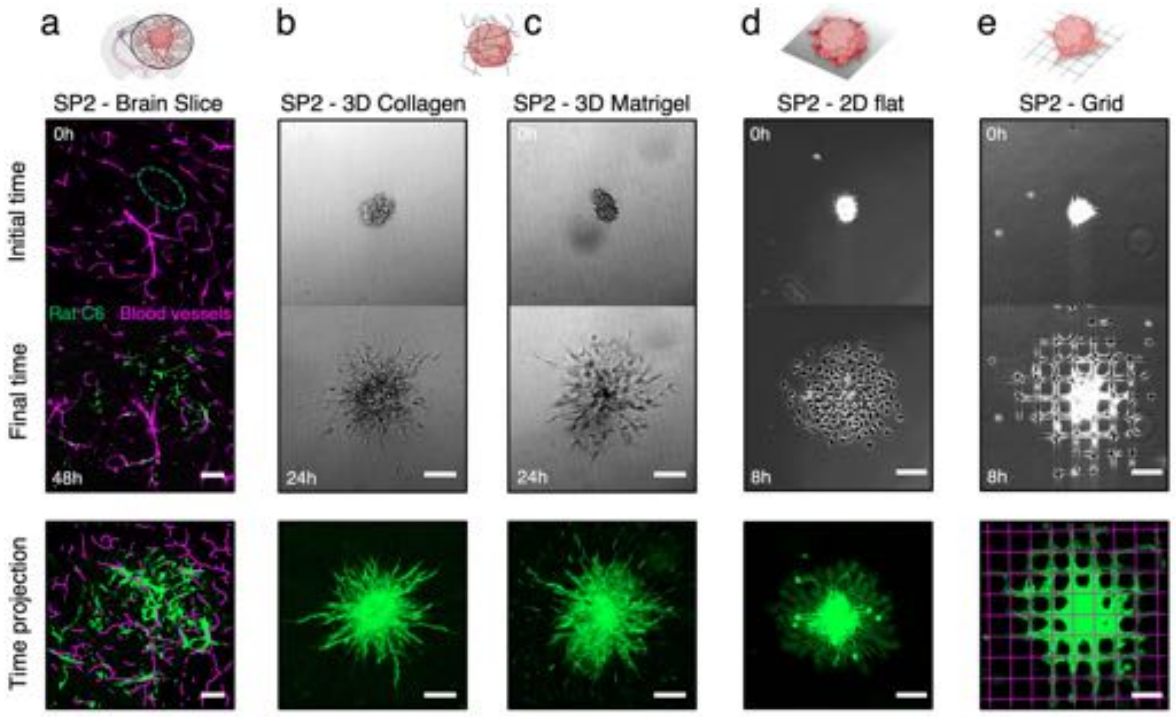

Figure 2.5: Comparison between *in vitro* setups hints at SP2G efficiently mimicking glioblastoma invasion on brain blood vessels. (A) SPheroid SPreading (SP2) of glioma rat C6 (green, DiOC6 dye) loaded on an *ex vivo* brain slice at 0 h and 48 h. The dashed oval roughly represents the initial area of the spheroid. The blood vessels are in magenta colour (Dil dye, intracardial injection). The time projection (maximum intensity firstly in Z, then in time) of C6 SP2 (green) is overlaid to the skeletonized blood vessels (magenta). (B) SP2 of glioma rat C6 embedded in 6 mg/ml collagen at 0 h and 24 h. The time projection (minimum intensity firstly in Z, then in time) is obtained from phase contrast. (C) SPheroid SPreading (SP2) of glioma rat C6 embedded in 10 mg/ml matrigel at 0 h and 24 h. The time projection (minimum intensity firstly in Z, then in time) is obtained from phase contrast. (D) SPheroid SPreading (SP2) of glioma rat C6 on 10 µg/ml laminin at 0h and 8 h (2D flat). The time projection (maximum intensity in time) is obtained from phase contrast. (E) SPheroid SPreading (SP2) of glioma rat C6 on 50 µg/ml laminin grid at 0h and 8 h. The time projection (green, maximum intensity in time from phase contrast) is overlaid to the skeletonized gridded micropattern (magenta). Bars in are 100 µm.

slices ($>$ 48 h). More importantly, time projections revealed that C6 cells aligned along the blood vessels in brain slices, while in 3D gels they invaded isotropically (Fig. 2.5A-C). Similarly, C6 cells aligned along the laminin grids when migrating on the micropatterns while on 2D-flat they spread out isotropically (Fig. 2.5D,E).

Spheroid spreading was quantified by measuring the areas of the spheroids at various time points relative to the area at the initial time point (24 h for 3D gels

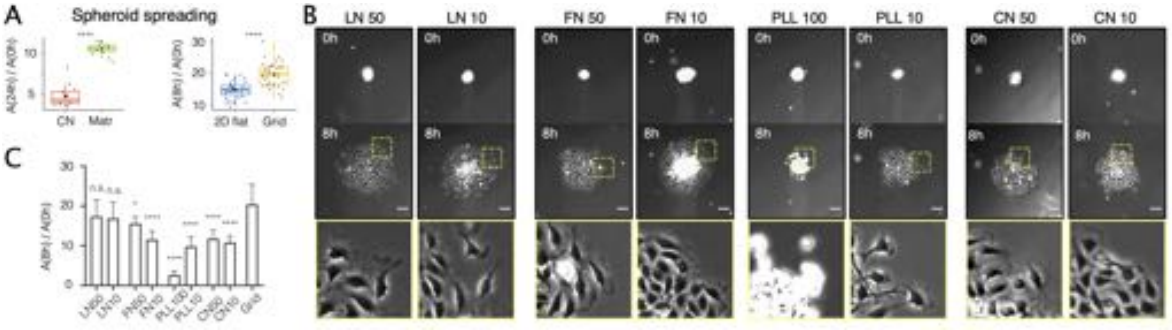

Figure 2.6: SP2G quantification and substrate. (A) Quantification of spheroid spreading in the *in vitro* systems tested in Figure 2.5 (n = 14, 15, 35, 35 spheroids). For the brain slice, results are not applicable, due to tissue opacity that scatters the signal at 0 h. Two-tailed unpaired t-test (****, p<0.0001). (B) SP2 of glioma rat C6 on coated 2D flat substrates at 0 h and 8 h. From left to right: Laminin (LN) at 50 and 10 µg/ml, fibronectin Fibronectin (FN) at 50 and 10 µg/ml, poly-L-lysine (PLL) at 1000 and 10 µg/ml, Collagen (CN) at 50 and 10 µg/ml. The dashed square is zoomed in the bottom panel. (C) Bar plot quantifying SP2 of the conditions depicted in (A). Data are reported as the area occupied by the maximum intensity projection at 8 h over the initial area. Bars are SD. n = 10, 7, 8, 6, 8, 8, 8, 8, 12 spheroids. One-way ANOVA, p<0.0001. Multiple comparisons: Grid vs LN50 / LN10 n.s.; Grid vs FN50 p=0.0133 (*); others p<0.0001 (****).

and 8 h for 2D and micropatterns, Figure 2.6A). Spheroid spreading in brain slices was not quantifiable due to tissue opacity and scattering of the GFP signal (Fig. 2.5A) that often blurred the spheroid profile. As observed in Figure 2.6A, spheroid spreading was higher in matrigel than in collagen (10.58 ± 0.75 and 4.76 ± 1.31, respectively; mean ± s.d.) and higher on grids than on 2D flat (19.73 ± 3.81 and 14.82 ± 2.70, respectively; mean ± s.d.). Moreover, on 2D flat, spheroid spreading was

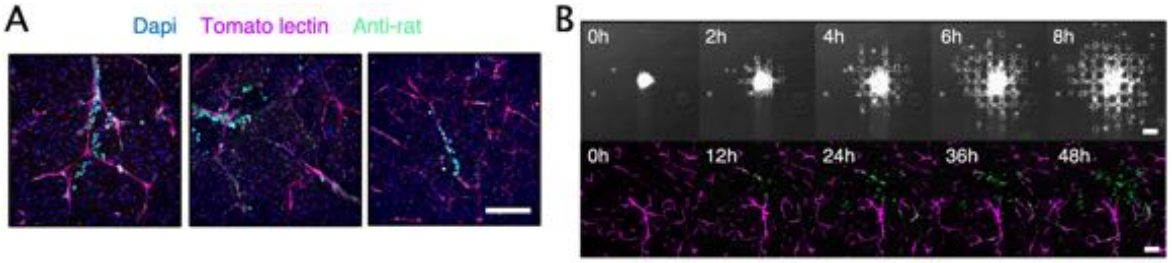

Figure 2.7: SP2G vs brain slice assay. (A) Organotypic brain slices immunostained for cell nuclei (DAPI, blue), blood vessels (tomato lectin, magenta), anti-rat (green, for rat C6 glioma) shows colocalization between the vasculature and glioma cells. Bar is 50 µm. (B) Comparison between SP2G and SP2 on brain slices, bar is 100 µm.

higher on Laminin (LN) than on Fibronectin (FN), Collagen (CN) or poly-L-lysine (PLL) (Fig. 2.6B,C), confirming laminin as the best matrix protein to study glioma motility [91, 92]. The staining of the blood vessels in brain slices and the gridded micropatterns revealed that the size of the linear tracks, the distances between the tracks and the junctions were similar, confirming our gridded micropatterns as an

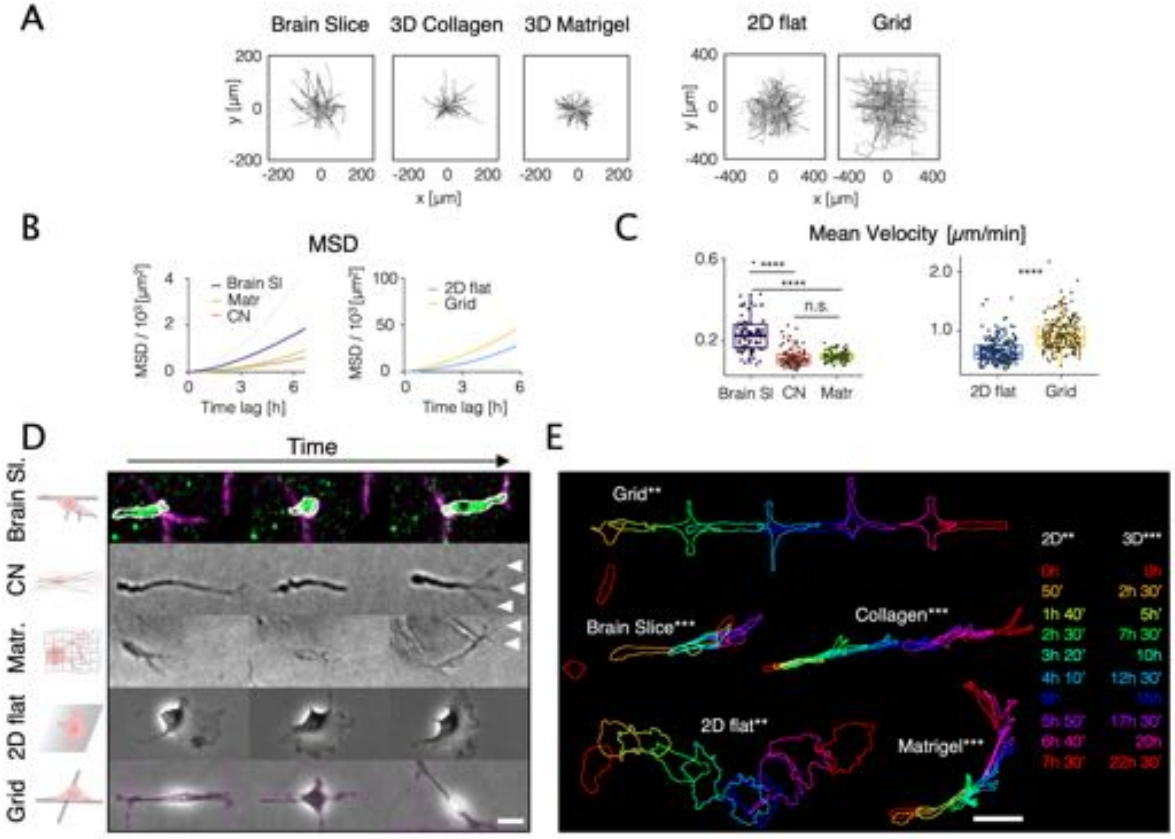

Figure 2.8: Single cell behavior in SP2G. (A) Cell trajectories in brain slice, 3D collagen, 3D Matrigel, 2D flat, and SP2G. (B) Mean Squared Displacement (MSD) plots obtained from single cell tracks in the *in vitro* systems tested in Figure 2.5 (n = 80, 95, 90, 216, 216 tracks; 5 to 7 tracks per spheroid. n = 2, 2, 2, 6, 6 independent experiments). Friedman test for Brain slice-Collagen-Matrigel ($p<0.0001$ in all the multiple comparisons), Mann-Whitney test for 2D-grid ($p=0.0001$). (C) Mean velocities of single cells. n = 80, 95, 90, 215, 215 tracks; 5 to 7 tracks per spheroid, each dot is a cell. One-way ANOVA. (D) Representative behavior of rat C6 single cells in the *in vitro* systems tested in Figure 2.5. For the brain slice, the cell is green (DiOC6 dye) and the blood vessels are in magenta (Dil dye). For the grid, the dashed magenta overlay corresponds to the contours of the micropattern. Bar is 20 µm. (E) Panel summarizing cell shapes for rat C6 cell motility in the *in vitro* systems tested in 2.5. Time is color-coded as indicated in the panel. ** is for the 2D setups (2D flat and Grid), *** is for the 3D setups (Brain Slice, Collagen, Matrigel). Bar is 50 µm.

excellent proxy to mimic brain blood vessel tracks (Fig. 2.1, 2.7).

We then compared single cell motility in the 5 settings (Fig. 2.8). We tracked single cells to evaluate their migration efficiency (Fig. 2.8A), represented as Mean Squared Displacement (MSD) in Figure 2.8B, mean velocity (Fig. 2.8C) and cell shape (Fig. 2.8D,E). When the experimental setup provided vessel-like topographical cues (Brain slices and grids, Figure 2.7B), cells migrated faster and further than the other experimental setups (collagen, Matrigel and 2D flat, Figure 2.8A-C) and showed comparable elongated shapes with "stick-slip" motility features (Fig. 2.8D,E) [210, 211]. At the opposite, in 3D hydrogels cells protruded multiple finger-like structures, likely due to the tangled complexity of the environmental cues (Fig.

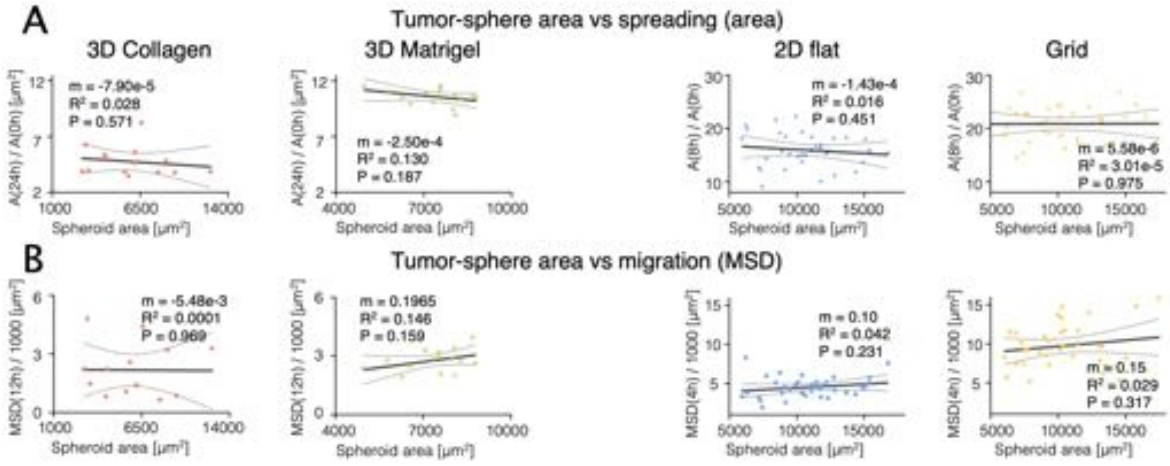

Figure 2.9: SP2G is independent from spheroid size, both considering area ratio and Mean Squared Displacement (MSD). (A) Linear regression plots shows no correlation between the spheroid area at the initial time point and its expansion, which is calculated as the ratio between the final area (obtained from maximum intensity projection) and the initial area. Each dot is a spheroid (n = 14, 15, 35, 35). For each graph, the line slope (m), the coefficient of determination (R^2) and the p-value (P) of the linear regression are reported. Pearson's r correlation coefficients, from left to right: -0.16, -0.36, -0.13, 0.01. (B) Linear regression fits show no correlation between the spheroid area at the initial time point and its expansion, which is calculated as the Mean Squared Displacement (MSD) sampled at 12 h (3D collagen and 3D matrigel) or at 4 h (2D flat and grid). Each dot is a spheroid (n = 14, 15, 35, 35) and MSD is calculated as the mean MSD of all the tracks belonging to a spheroid (5 to 7 tracks per spheroid). For each graph, the line slope (m), the coefficient of determination (R^2) and the p-value (P) of the linear regression are reported. Pearson's r correlation coefficients, from left to right: -0.01, 0.38, 0.17, 0.20. For this analysis, brain slice is omitted due to tissue opacity that scatters glioma GFP signal at the initial time points.

2.8D, arrowheads). On flat surfaces cells adopted a fan-like shape as previously described on homogeneous substrates [91, 94].

We then tested whether spheroid spreading and single cell motility were dependent on the original spheroid size. We plotted spheroid area ratio and MSD in function of the original spheroid area and, as indicated by the almost null slopes (m), the low coefficients of determination (R^2), the non-statistically significant p-values (P), and the low Pearson's correlation coefficients no correlation was found (Fig. 2.9).

Finally, we analyzed the performance of each technique with radar plots using an indexing system from 1 to 5 (poorest to best performance) for 7 key parameters in GBM motility analysis: time profitability, presence of linear topographic cues allowing stick-slip motility, experimental reproducibility, optical accessibility, 3D confinement, possibility to implement semi-automated analysis and *in vivo* mimicry (Fig. 2.10). As planned, SP2G system covered more requirements than all other systems, marking the highest score in 4 out of 7 parameters.

Figure 2.10: SP2G is independent from spheroid size, both considering area ratio and MSD. Radar plots summarizing experimental scores (1 to 5) of time profitability, presence of linear cues, experimental reproducibility, optical accessibility, possibility to develop analytical tools, three-dimensionality (3D) and *in vivo* mimicry for in the *in vitro* systems tested in Figure 2.5.

2.3 SP2G experimental setup and image analysis workflow

In light of the advantages emerged while proposing SP2G, we optimized the experimental protocol and tailored to it a semi-automated analysis workflow, which aimed to quantitatively describe cell migration and motility modes (Fig. 2.11). It is composed of 7 open-source ImageJ/Fiji macros, which ultimately delivers 6 outputs, 3 for evaluating cell migration:

1. migration area;
2. diffusivity;
3. boundary speed;

and 3 for characterizing the motility modes:

4. collective migration;
5. directional persistence;
6. hurdling.

In order to obtain a better cell segmentation and a stable readout in the analytical workflow, grids and spheroids, in the experimental part, were stained with fluorescent dyes and spreading was imaged by fluorescence and phase contrast microscopy (Fig. 2.11A). Briefly, as spheroids reached circa 100 µm in diameter (most often in 5 days after passaging), we functionalized Petri dishes with the grid micropattern and spheroids with the fluorescent dye (Dil stain). The same day the time-lapse movies was acquired. Spheroids were loaded in the Petri dishes and after 15 min we began with the imaging. For the image analysis, we divided our SP2G workflow (Fig. 2.11B) in 2 main steps: one for characterizing cell migration (outputs 1 to 3), one for characterizing cell motility modes (outputs 4 to 6).

2.3.1 Characterization of cell migration with SP2G

The first step processes the raw data semi-automatically and characterizes cell migration with the outputs #1 (migration area, A(t)), #2 (diffusivity, D(t)) and #3 (boundary speed, v(t)). This is achieved by combining the binarized images of the grids and the spreading spheroids in order to construct a polygon that connects the grid nodes traveled by the spheroid invasive front at each time point. A time-lapse

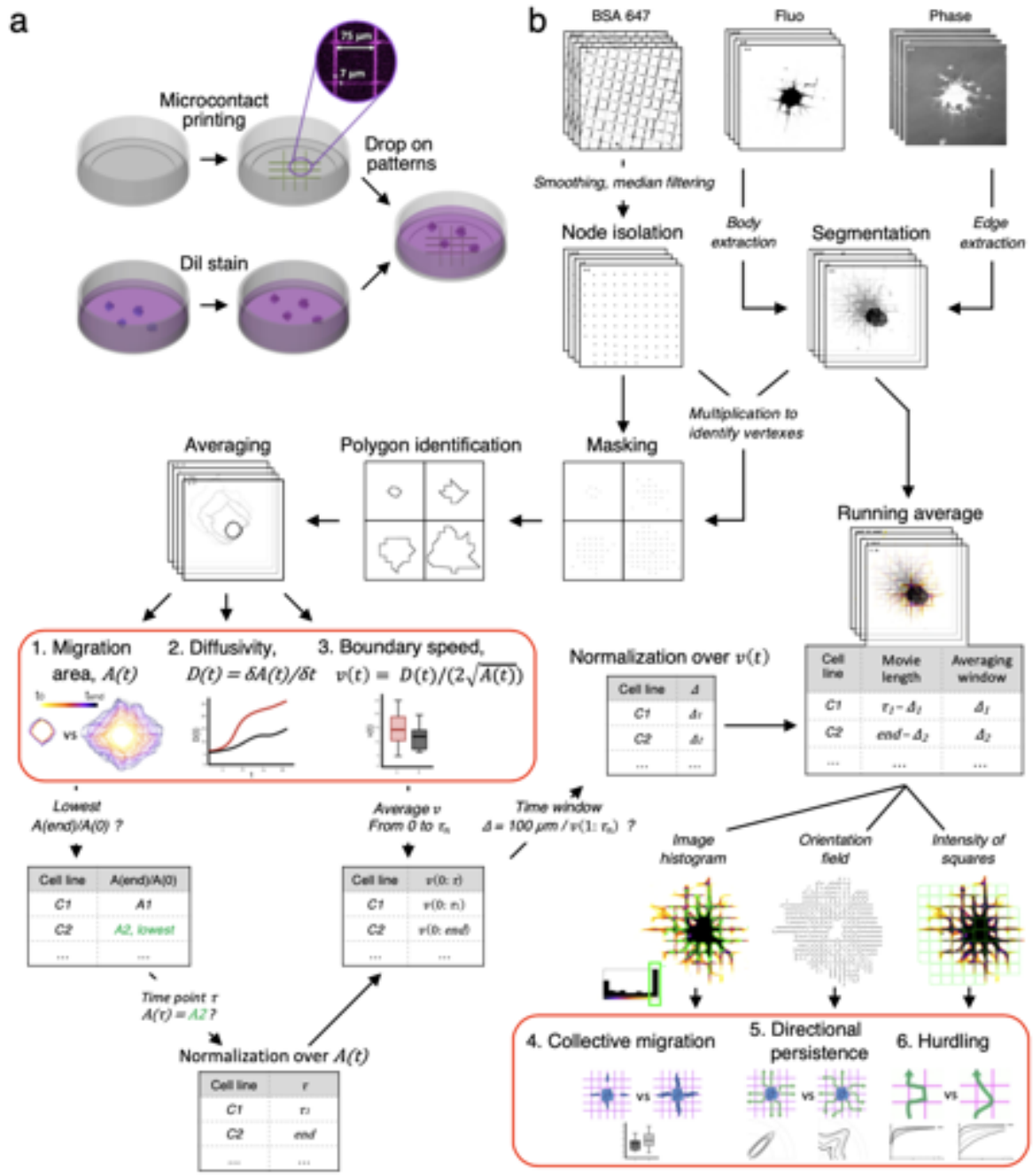

Figure 2.11: SP2G experimental setup and image analysis workflow. (A) Experimental setup at a glance. The spheroids and gridded micropattern are both fluorescent to facilitate tracking. Finally, the spheroids are leant on the grid and a time-lapse movie is acquired. (B) Image analysis workflow. SP2G segments the spheroid and grid in binary images that are multiplicated to isolate the grid nodes covered by the invasive boundary. Thus, SP2G reconstruct a polygon tracking the SP2 in time and several polygons are then averaged. To visualize migration area A(t) (output #1), the time trend is projected and color-coded. SP2G then obtains spheroid diffusivity D(t) by differentiating A(t), and from D(t) it gets the spheroid boundary speed v(t) (outputs #2 and #3, see Supplementary Appendix). When SP2G characterizes the motility modes of multiple conditions, it needs a normalized A(t) and v(t). To normalize over A(t), a time step τ has to be identified, where A(τ) / A(0) is equal

(Continued caption) to the minimum A(end) / A(0), which corresponds to the cell line C2. Therefore, each condition has its τ, such that A(τ) / A(0) is constant among all the conditions. In the slowest-motile cells τ = end and all the movies are then cut at τ. Furthermore, Δ normalizes over the boundary speed and corresponds to the time window to complete 100 µm. Δ is calculated in the interval 1:τ, so each condition is endowed with its own Δ, which is larger as cells are slower. SP2G creates Running Average (RA) movies by shifting Δ in the interval 1:τ. Each movie is τ – Δ frames long, covers the same area on average and each frame embeds information on the cell's footprint in the last Δ frames taken to complete 100 µm. SP2G characterizes the cell motility modes by extrapolating features from the RA movies: it thresholds the area (outlined in green) of pixels belonging to the last bin of the histogram to obtain collective migration (output #4), it evaluates the image orientation for directional persistence (output #5), and samples the intensities of the grid squares (passivated areas, highlighted in green) for hurdling (output #6).

of a growing polygon representing the leading edge of the invading cells is then automatically generated for each spheroid. Outputs #1-3 for cell migration are extrapolated as follows:

- an average migration area A(t) per cell line (> 10 spheres per cell line) is represented by firstly aligning the baricenters of the polygons, and subsequently by extrapolating the mean radial coordinates of all the polygons at each time point (Fig. 2.11B, output #1: it is a graphical display item, it quickly shows how the area occupied by the cells has evolved overtime and the time is color-coded as shown).

- The corresponding numerical values (1 trend per spheroid) are smoothed and then differentiated in time to obtain values for diffusivity D(t) (Fig. 2.11B, output #2: the trends are the rate at which cells occupy their surrounding area, and always expressed in μm^2/min and calculated at each time point).

- Then, boundary speed v(t) (Fig. 2.11B, output #3) is derived from the following formula

$$v(t) = \frac{D(t)}{2\sqrt{A(t)}} \tag{2.1}$$

that expresses how quickly the invasive boundary of the spreading spheroid advances in its surrounding area. It is expressed as a monodimensional rate (µm/min), which facilitates the interpretation of the results for the cell migration community and can be intended as measurement of "average single-cell speed" (see "Materials and methods" chapter and Supplementary Appendix for computational details and derivation of the formula).

Finally, all D(t) and v(t) trends are mediated in order to obtain average time trends D(t) and v(t).

2.3.2 Characterization of cell motility modes with SP2G

The second step of SP2G analysis works on the binarized images of spheroids and grids. It provides 3 additional numerical outputs that characterize cell motility modes (Fig. 2.11B, red box in the left): collective migration (output #4: the higher the values, the more cells migrate as collective strands; vice-versa if the spheroid expands as singlets), directional persistence (output #5: the higher the values, the more cell stay on the same direction; vice-versa if cells turn frequently) and hurdling (output #6: the higher value the more cells are cutting angles. This is a concept we introduced in [92] and quantifies how cells *hurdle* over the grid angles: it can be interpreted as an hallmark of invasivity). Importantly, only motile cells are considered for motility modes analysis. To categorize motile and non-motile cells, we imposed a threshold that is based on the average boundary speed: if higher than 100 µm / 8 h (0.231 µm/min) cells are categorized as motile, if lower as non-motile.

The characterization of motility modes is based on RA movies obtained from the binary masks of the spreading spheroids. We defined the time window to complete 100 µm as Δ, which is calculated as 100 µm / $\bar{v}$, being $\bar{v}$ the mean v(t) in time. When studying a stand-alone condition, RA movies are generated by shifting Δ and are long 96 – Δ frames (8 hours sampled every 5 min returns 96 frames: this is the conditions we applied in acquiring all the time-lapse movies throughout this work). However, when comparing the motility modes of conditions with specific A(t), D(t) and v(t), SP2G requires normalization over migration area and boundary speed in order to avoid results biased by different cell speeds. To normalize over migration area, a time step τ has to be identified, where A(τ) / A(0) is equal to the minimum A(end) / A(0). Thus, each condition has its own τ, such that A(τ) / A(0) is constant

among all the conditions. Furthermore, Δ normalizes over the boundary speed and is calculated in the interval 1:τ. Each condition is endowed with its own Δ, which is larger as cells are slower. Each movie is $\tau - \Delta$ frames long, covers the same area on average and each frame embeds information on the cell's footprint in the last Δ frames. These steps are highlighted in the lower part of Figure 2.11B.

The analysis of image features in the RA movies provides numerical outputs for cell motility modes (Fig. 2.11B, red box in the bottom right).

- SP2G extrapolates collective migration by thresholding the region belonging to the last bin of the RA histogram (Fig. 2.11, output #4, green area). Cells migrating collectively forms long strands that protrude from the spheroid, thus giving rise to higher values when averaged in the RA (Fig. 2.12A). The larger this area, the higher the ratio with the total area occupied by the cells (values are between 0 and 1). Strikingly, the numerical outputs of SP2G reflect the collective migration in simulated data of moving particles in which we imposed 3 collective-migration regimes (continuous, pseudo-continuous, and diffusive) and 3 speed regimes (Fig. 2.12B-D).

- SP2G computes directional persistence by evaluating the image orientation (Fig. 2.11, output #5). Due to its orientation, the grid provides 2 preferential directions for the cell path: 0°, 90°. Therefore, cells that are capable of turning necessarily leave their footprint along 45° and 135° (the least-preferred directions), thus increasing orientation values along these directions. Given that there are 180 orientation values (1 per direction, sampled every 1°) that thus constitute an Orientation Field (OF), we reasonably assumed that the spheroid spreading is isotropic: if the center of the spheroid is placed at the origin of an xy reference system its spreading is uniform over the 4 quadrants. Therefore SP2G averages the values 0-90, 1-91, 2-92, etc. and gets 90 values. SP2G then calculates directional persistence (DP in equation 2.2) as the ratio between orientation values in the neighborhoods of preferential (0° and 90° after the averaging) and least-preferred (45° after the averaging) directions:

$$DP = \frac{OF[0°] + OF[1°] + OF[2°] + OF[3°] + OF[87°] + OF[88°] + OF[89°]}{OF[42°] + OF[43°] + OF[44°] + OF[45°] + OF[46°] + OF[47°] + OF[48°]} \tag{2.2}$$

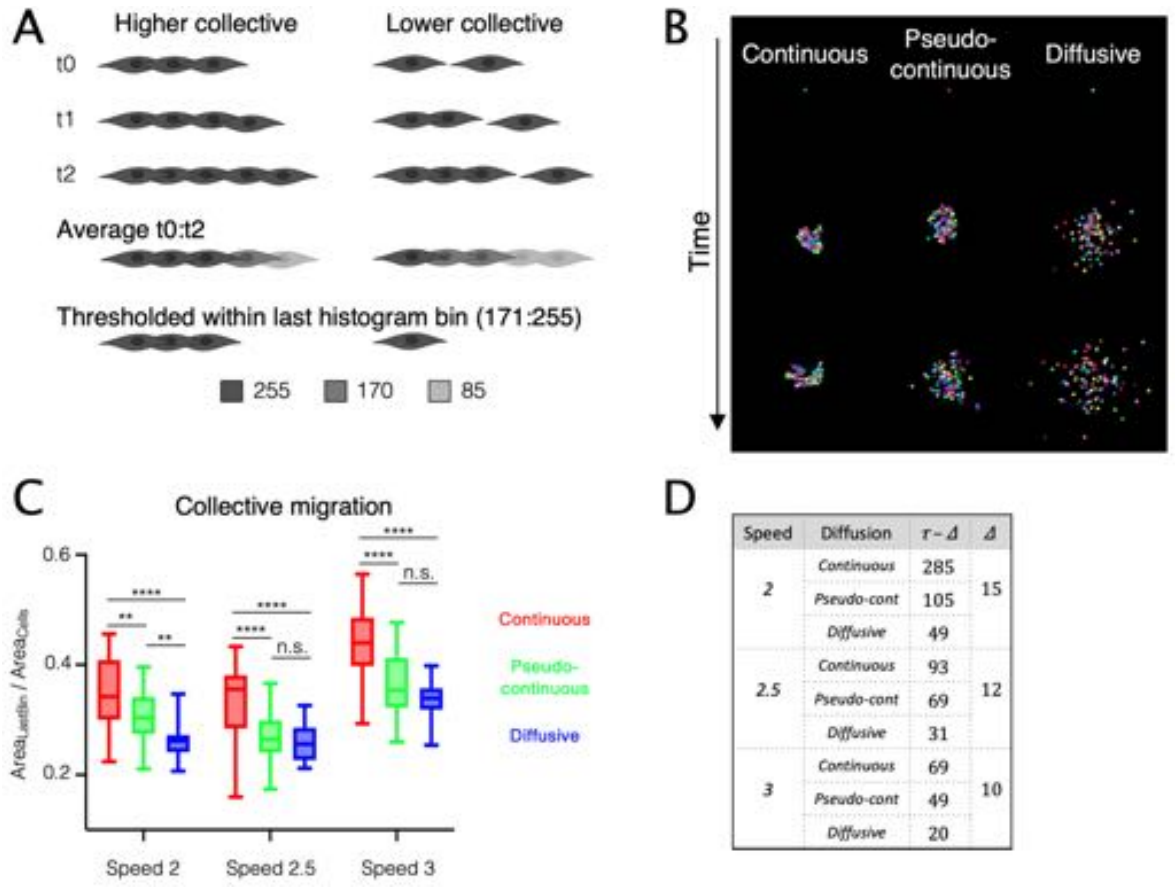

Figure 2.12: SP2G: validation for collective migration algorithm. (A) Schematic representation of the rationale behind the calculation of collective migrations. As cells migrate as strands, they give rise to higher values in the average images that, when thresholded, form an higher area. (B) Simulated data of 100 round particles (radius=5 pixels) diffusing with constraint (Continuous, 100% probability of being attached to a neighbor), partial constraint (Pseudo-continuous, 90% probability of being attached to a neighbor), or no constraint (Diffusive, simple diffusion). Data were generated over 300 time frames at 3 speed regimes, with mean 2, 2.5, 3 pixels per frame and standard deviation 2, 2.5, 3 pixels, respectively (9 conditions overall). The example depicts the example with speed=3±3 pixels per frame. (C) Collective migration for data simulated as in (B). (D) The table summarizes the selected τ and Δ. Δ was chosen so as to its product with speed equals 30. One-way ANOVA, n=30 simulations per condition.

- Finally, SP2G calculates hurdling by sampling the intensity of the grid squares (Fig. 2.11, output #6; see Supplementary Appendix). The rationale behind this analysis is that the cells more capable of cutting corners leave high intensity values in the grid squares, while those sticking to the micropatterned grid do not.

SP2G computes time trends for outputs #4-5-6, but, for the sake of simplicity, we

reported in all the results that will follow the values averaged across spheroids from the last frame of RA movies.

a. Migration area, A(t). *Semi-automated step.*					
Place raw data in a folder. Raw data can be:	• Several bio-format files (e.g. 1 per condition) • .tif files (1 per spheroid) placed in a sub-folder	Run code *"Main: Polygon Tracking and Segmentation"*. Inputs: raw data. Outputs are:	1 folder per raw data file, in which 1 subfolder per sample contains:	• Binarized grid • Binarized cells • Polygonal shape • Binarized grid nodes • .avi movie • .txt file (debugging)	• Run code *"Average Polygon"*. Input: *polygonal shape.* → • Output: graphical representation for A(t)
b. Diffusivity, $D = \delta A(t) / \delta t$; Boundary speed, $v(t) = D(t) / (2\sqrt{(A(t))})$. *Automated step.*					
Run code *"Polygon Area Measurement"*. Input: *polygonal shape.* Outputs, in the same .csv file :	• Migration areas A(t) (absolute and relative to t_0) • Smoothed A(t) • Diffusivity D(t) • Boundary speed v(t)				
c. Extrapolate τ and Δ from mean A(t) and $v(t)$. *Semi-automated/User step.*					
• τ normalizes over migration area. It is the time step when the mean A(t) reaches the lowest A(final_time) among the experimental conditions to compare. • Δ normalizes over boundary speed. It is the time window taken by the cells to travel 100 μm. If Δ < 8h, cells are considered motile. Δ must be lower than τ. *See supplementary file 1, it can be utilized as template.*					
d. Collective migration and Directional Persistence. *Automated step.*					
Run code *"Collective migration and Directional Persistence"*. Input: *binarized cells*. Output:	Collective migration and Directional Persistence values in .csv file (mean and indexed by spheroid name. All values indexed by time point.)				
e. Hurdling. *Semi-automated step.*					
Run code *"Hurdling"*. Input: *binarized cells* and *binarized grid*. Outputs:	• Average Intensities (1 value per square) + Mean Average Intensity (1 value) in .csv file, for relative hurdling calculation. • Average intensities (1 value per square) normalized over the maximum value of the dataset in the same .csv file, for visualizing the cumulative distribution. All values indexed by time point. *See supplementary file 2.*				

Table 2.1: Table summarizing SP2G quantitative outputs and how to obtain them.

Table 2.1 summarizes quickly which ImageJ/Fiji macro returns which output, the key passages to perform and what inputs they need. A brief introduction on the 7 ImageJ/Fiji macros follows.

0. **Make ROI Grid**. It is not strictly necessary for the completion of the analysis workflow, though is strongly advised. It is a semi-automated process and requires as input a fluorescent image of the grid micropattern, then returns to the user a Region Of Interest (ROI) outlining the grid micropattern (ROI_GRID). ROI_GRID is going to be useful to mask the grid micropattern in case, when running the other codes, its segmentation fails, or when analyzing images devoid of fluorescence.

1. **Main. Polygon tracking and segmentation**. It is the main piece of analysis. It is a semi-automated process and requires as input the raw data (either in .tif format or any BioFormat, which are microscope proprietary formats, e.g. .lif from Leica). It returns as many folders as the fields of view contained in

the raw data, that is 1 field of view per spreading spheroid. Each folder has the name of the series/.tif and contains 6 files:

- a binarized image of the spreading spheroid (.tif);
- a binarized image of the grid (.tif);
- a binarized stack of the grid nodes (.tif);
- a binarized image of the tracking polygon (.tif);
- a representative movie of the tracking (.avi);
- a .txt file (for debugging).

All the folders are contained in a main folder dedicated to the results (1 main folder per raw data file), which is created by SP2G in the same location of the raw data files.

2. **Average polygon**. With this fully-automated code SP2G browses all the main folders containing the single-spheroid subfolders and returns 3 outputs:

   - 1 temporal stack visualizing the average polygon (.tif file);
   - 1 temporal stack visualizing the average polygon standard deviation (.tif file);
   - 1 image where the average temporal stack is color-coded (.tif file).

3. **Diffusivity and Boundary speed**. This is the first macro that lets the user have numerical outputs and extrapolates 1 .csv file per cell line/condition containing the following time trends, 1 time trend per spheroid:

   - Raw area;
   - Area ratio, normalized over the first value;
   - Smoothed area;
   - Diffusivity;
   - Boundary speed.

4. **Collective migration and Directional persistence**. This code is fully automated and it calculates collective migration and directional persistence. Their values are saved in a .csv file, and are time trends, 1 time trend per spheroid

(the top row is the initial time). Briefly, the RA movie is generated from the spheroid binary mask and utilized to extrapolate collective migration and directional persistence. Each frame of the RA movie is calculated by averaging Δ frames, and the movie is capped at the τ^{th} frame (the final movie is τ - Δ frames long).

Directional persistence is calculated through the function "OrientationJ distribution" of the OrientationJ plugin, which returns the OF. As explained previously, it performs the ratio between the direction of least resistance to cell migration (i.e. the ones provided by the grid segments) and the direction of most resistance (the one a cell has necessarily to face when undergoing a directional change).

Collective migration (CM in equation 2.3) values are obtained by thresholding each frame of the RA within the last histogram bin, that necessarily spans up to 255 (the maximum value of an 8-bit image). The ratio

$$CM = \frac{\#Counts[Lastbin]}{\#TotalCounts} \tag{2.3}$$

returns numerical values for collective migration. Background pixels are set to NaN.

The values for both the parameters are saved in a .csv file (1 time trend per spreading spheroid).

5. **Hurdling**. This macro is semi-automated and returns values for hurdling in a .csv file. Upon generating the RA movie, SP2G samples the mean intensity of each square of the grid micropattern. At the end of the analysis SP2G saves a .csv file that contains:

   - The mean intensity values from all the squares in all the images, normalized over the maximum value of the dataset. These values are meant to be plotted as a cumulative distribution: the lower its initial slope, the higher the hurdling.
   - The average intensity value at each time point. These values are obtained by averaging the mean intensity values of all the squares over the total number of squares, and this process is iterated in time.

All the details and step-by-step instruction can be found in the supplementary appendix.

2.4 SP2G quantifies migratory tactics adopted by glioblastoma cells

In order to test how faithfully our SP2G *in vitro* protocol and the dedicated analytical tools could characterize cell migration and cell motility modes, we had to necessarily utilize as biological background some patient-derived, glioblastoma cell lines whose behavior was known. This could permit to define a benchmark for the performance of SP2G. Therefore, we examined the spreading of 3 GBM cell lines known to migrate with different modes on grids from our previous work *"Adaptive mechanoproperties mediated by the formin FMN1 characterize glioblastoma fitness for invasion"* [92]: the NNI-11 (high proliferative, non-motile), NNI-21 (most-motile, *hurdlers*) and NNI-24 (motile, *gliders*).

As observed in Figure 2.13, we confirmed their migratory behavior with initial experiments based on SP2G: within the same time window (4h) the most motile NNI-21 migrated out further away than the NNI-24 and NNI-11. Time projections quickly revealed how the NNI-21 had the most aggressive motility mode in light of how frequently they cut angles. However, no precise quantification is permitted just by adopting this simple approach and the profound dissection of motility modes still remain elusive.

In order to visualize the key points of the representative time-lapse movies, we created colored micrographs that highlight the cell edge at 4 time points (Fig. 2.14, Right): 0 h (purple), 2.5 h (blue), 5 h (green), 7.5 h (red). Furthermore, in the phase-contrast picture (middle) a representative ROI is meant to visualize cell migration in the same 4 time points (the grid micropattern is superimposed in magenta colour), while the left section displays the RA movie from the same image for the motility modes (Fig. 2.14, Middle and Left).

When quantifying cell migration, SP2G created a bigger average polygon for the

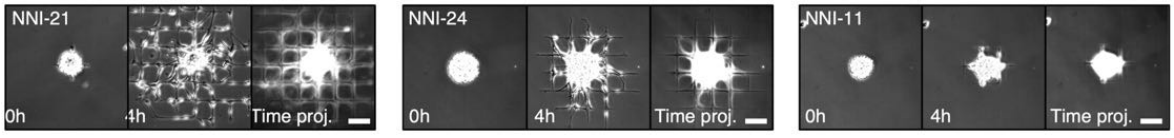

Figure 2.13: SP2G at 0 h, 4 h, and time projections (maximum intensity, phase contrast) of patient-derived glioblastoma cells from NNI-21, NNI-24, NNI-11 GBM cell lines. Bars are 100 µm.

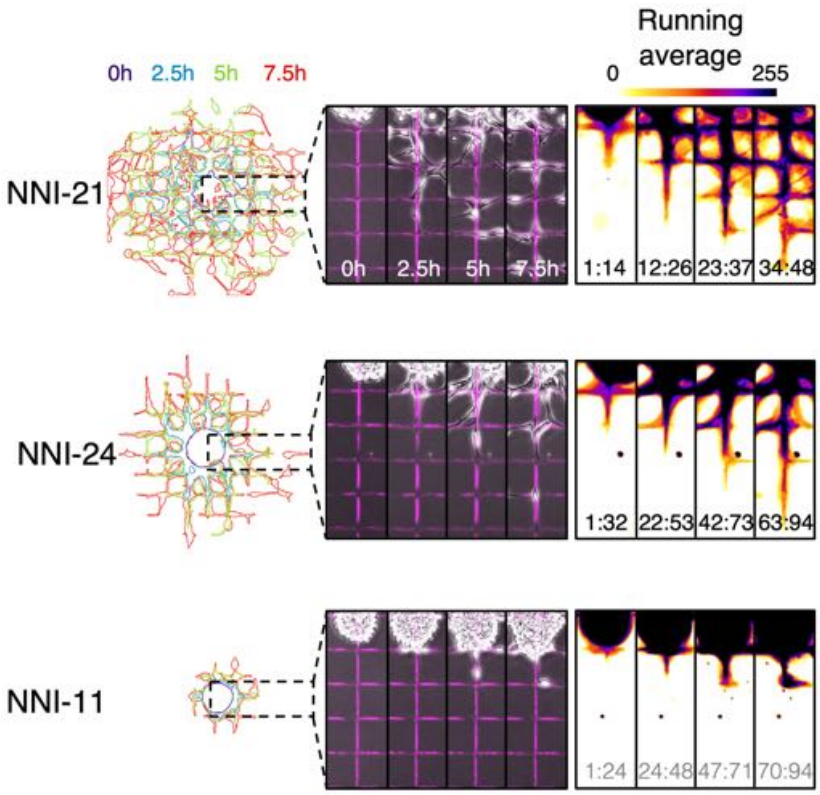

Figure 2.14: Benchmarking SP2G with NNI-21, NNI-24, NNI-11 GBM cell lines. (Left) Micrograph highlighting cellular edges at 4 time points (0h, 2.5h, 5h, 7.5h) as the spheroid spreads. Time is color-coded as indicated. Here 3 cell lines are tested and ranked from most to least invasive: NNI-21, NNI-24, NNI-11 (n = 10, 11, 13 spheroids. n = 2, 2, 2 independent experiments). (Middle) Insets displaying cellular morphology at 0h, 2.5h, 5h, 7.5h. (Right) Insets displaying the RA of the same ROI than (Middle). Image intensity is color-coded as indicated. The 4 insets are regularly spaced within the length of the RA movie. The time window Δ constituting the corresponding RA frame is indicated at the bottom of each inset: for the non-motile cells is by default in grey colour and created with $\tau = 94$, $\Delta = 24$.

NNI-21, then NNI-24 and NNI-11 (Fig. 2.15). This graphical output was reflected in a greater diffusivity (Fig. 2.16A; $D_{\text{NNI-21}}$(3h 30') = 1585 ± 282 µm^2/min, $D_{\text{NNI-24}}$(3h 30') = 324 ± 204 µm^2/min, $D_{\text{NNI-11}}$(3h 30') = 91 ± 103 µm^2/min; mean ± s.d.) and a greater boundary speed (Fig. 2.16B; $v_{\text{NNI-21}}$(0 : 3h 30') = 1.54 ± 0.3 µm/min, $v_{\text{NNI-24}}$(0 : 3h 30') = 0.72 ± 0.2 µm/min, $v_{\text{NNI-11}}$(0 : 3h 30') = 0.19 ± 0.07 µm/min; mean ± s.d.). Only the NNI-21 and the NNI-24 passed the threshold for motile cell lines (Fig. 2.16C), then the next step was to characterize their motility modes.

In accordance with our previous observation [92], the NNI-21 cells were migrating in a stochastic and jumpy motion that was reflected in a low directional persistence

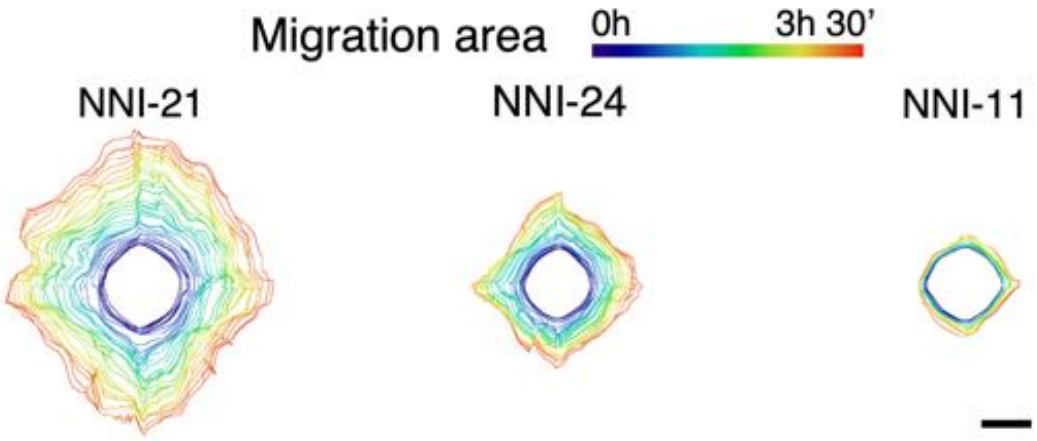

Figure 2.15: Average polygon visualizing migration area for NNI-21, NNI-24, NNI-11. Its expansion in time is color-coded as indicated. Bar is 100 µm.

(3.6 ± 0.7, NNI24: 8.5 ± 2.6, Fig. 2.17B) and in high hurdling (Fig. 2.17C). Hurdling was visualized with a Cumulative Distribution Function (CDF): lower slopes indicate more hurdling (i.e. more cutting-corner behavior and bridging over the passivated areas). In order to render hurdling in numbers, we divided the average square intensity of the NNI-21 by the one of the NNI-24, returning a relative value of 2.08. In general, the average square intensity of the most hurdling is divided by the others so as to have numbers > 1. Moreover, the NNI-24 displayed higher collective migration than NNI-21 (0.33 ± 0.07 and 0.22 ± 0.04, respectively; Fig. 2.17A).

As next step we studied how SP2G could be sensitive to external perturbations.

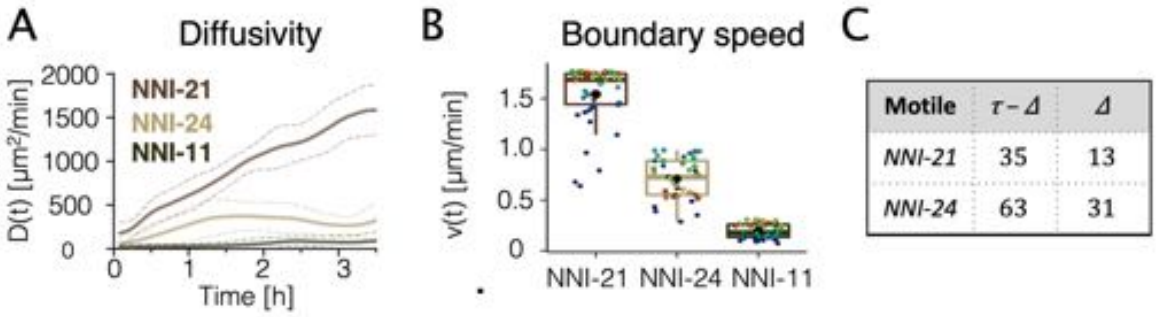

Figure 2.16: Diffusivity and boundary speed for NNI-21, NNI-24, NNI-11. (A) Diffusivity over 3 h 30' ($p<0.0001$, Kruskal-Wallis test). Dashed lines are the standard deviation. Dunn's multiple comparison test: $p<0.0001$ for all. (B) Mean boundary speed over 3h 30'. Each dot represents a time-point and is color-coded as in Figure 2.15 ($p<0.0001$, Kruskal-Wallis test). Dunn's multiple comparison test: $p<0.0001$ for all. (C) Table highlighting motile cell lines (faster than 100 µm / 8 h = 0.21 µm/min), their corresponding Δ (number of frames needed to travel 100 µm) and τ - Δ (number of frames in the RA movie).

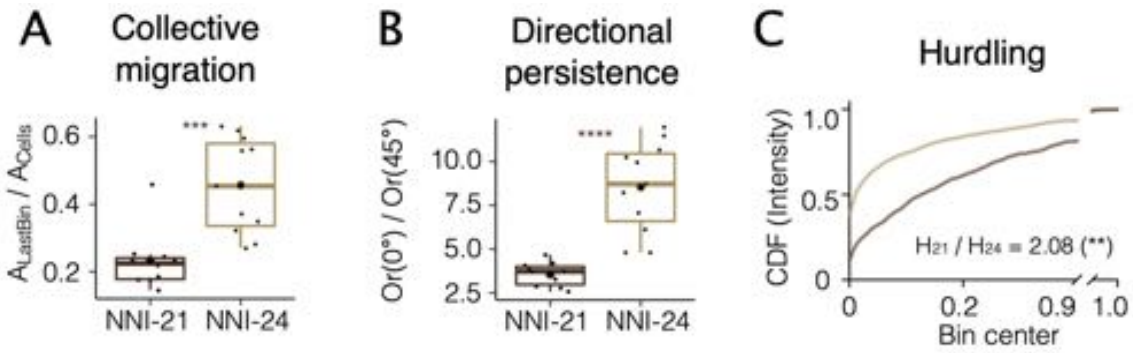

Figure 2.17: Motility modes for NNI-21 and NNI-24. (A) Collective migration for the motile NNI-21 and NNI-24. It is visualized as the ratio between the area covered by the pixels belonging to the last bin of the histogram and the total number of pixels covered by the cells ($A_{LastBin}$ / A_{Cells}). Each dot represents a spheroid. p=0.0004, two-tailed unpaired t-test. (B) Directional persistence for the motile NNI-21 and NNI-24. It is visualized as the ratio between the orientation along 0° and along 45° (Or(0°) / Or(45°)). Each dot represents a spheroid. p<0.0001, two-tailed unpaired t-test. (C) Hurdling is visualized as the CDF of the normalized mean intensity of the grid squares (image intensity is sampled in each square). p=0.0032 (**), Kolmogorov-Smirnov test. The ratio indicates the relationship between the average mean intensities (the sum of the mean intensity from all the squares divided by the total number of squares) of the 2 cell lines. All the bars are 100 µm. In all the boxplots, the middle horizontal line represents the median and the black dot is the mean value.

Given that the NNI-21 were the most migratory and the most aggressive cell line among the 3 tested so far, we focused on NNI-21 spheroids while applying a set of cytoskeleton-perturbing drugs. We recorded the effects for the Arp2/3 inhibitor CK666, the myosin II inhibitor blebbistatin, the microtubule poison nocodazole, and the actin poison latrunculin-A, each at 2 different concentrations (Tab. 2.2).

For the sake of simplicity, I reported in Figure 2.18 only the milder treated

Drug	Conditions tested		
CK666	Control	100 µM	200 µM
Blebbistatin	Control	10 µM	20 µM
Nocodazole	Control	0.1 µM	1 µM
Latrunculin-A	Control	0.3 µM	1 µM

Table 2.2: Summary of the conditions tested with cytoskeleton-perturbing drugs (NNI-21). Each experiment has its own independent control.

condition, ranked from the least to the most effective (i.e. NNI-21 are ranked from the most to the least motile condition). From the pictures, it emerged how CK666 poorly inhibited migration and the hurdling motility mode of the NNI-21, while under Blebbistatin and Latrunculin-A treatments cells seemed more compacted (i.e.

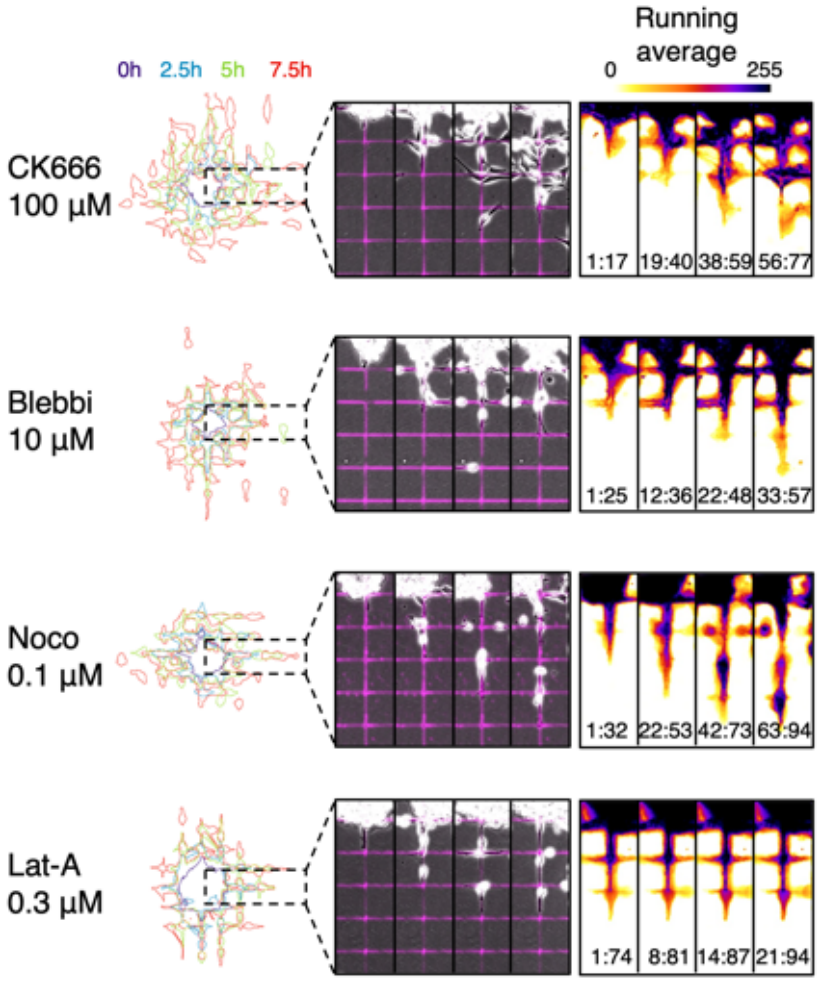

Figure 2.18: Testing SP2G with cytoskeleton-perturbing drugs. (Left) Micrograph highlighting cellular edges at 4 time points (0h, 2.5h, 5h, 7.5h) as the spheroid spreads. Time is color-coded as indicated. Here 12 conditions are tested with the cell line NNI-21 (CK666 100 and 200 µM (n= 16, 14 spheroids), blebbistatin 10 and 20 µM (n = 16, 14), Nocodazole 0.1 and 1 µM (n = 20, 12), latrunculin-A 0.3 and 1 µM (n = 26, 16), plus their respective control conditions (n = 25, 12, 16, 21)). n = 2 independent experiments per condition. The 4 conditions under milder treatments are visualized. They are ranked from most to least invasive: CK666 100 µM, blebbistatin 10 µM, nocodazole 0.1 µM, latrunculin-A 0.3 µM. (Middle) Insets displaying cellular morphology at 0h, 2.5h, 5h, 7.5h. (Right) Insets displaying the RA of the same ROI in (Middle). Image intensity is color-coded as indicated. The 4 insets are regularly spaced within the length of the RA movie. The time window Δ constituting the corresponding RA frame is indicated at the bottom of each inset.

more collectively migrating) and with thin, elongated cell bodies.

Graphical and numerical outputs helps to describe NNI-21 migration in all the conditions (Fig. 2.19): while CK666 100 µM did not significantly decrease diffusivity with respect to the control condition, all the other drugs were inhibiting migration and a dose-dependent response was clearly visible (Fig. 2.19B), particularly

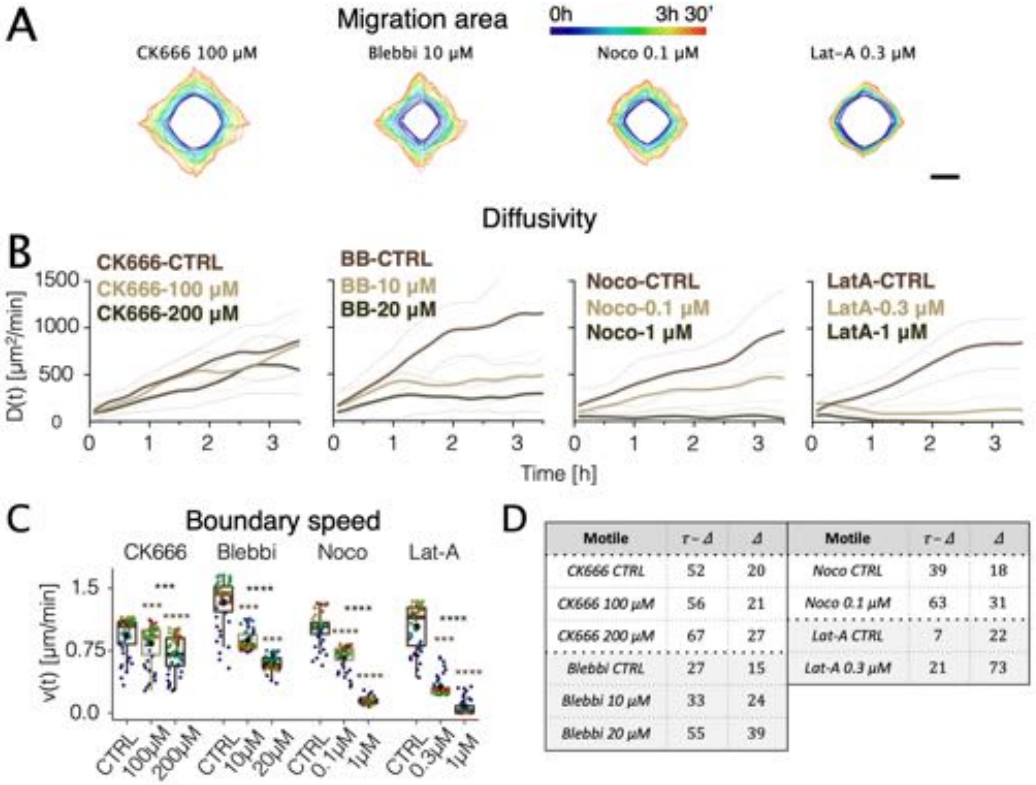

Motile	τ - Δ	Δ
CK666 CTRL	52	20
CK666 100 µM	56	21
CK666 200 µM	67	27
Blebbi CTRL	27	15
Blebbi 10 µM	33	24
Blebbi 20 µM	55	39

Motile	τ - Δ	Δ
Noco CTRL	39	18
Noco 0.1 µM	63	31
Lat-A CTRL	7	22
Lat-A 0.3 µM	21	73

Figure 2.19: SP2G detects the different migratory tactics upon inhibition of Arp2/3, myosin II, microtubules and f-Actin.. (A) Average polygon visualizing migration area. Its expansion in time is color-coded as indicated. Bar is 100 µm. (B) Diffusivity over 3 h 30' (from left to right: p=0.0003, p<0.0001, p<0.0001, p<0.0001 Kruskal-Wallis test). Dashed lines are the standard deviation. Dunn's multiple comparison test: CK666: CTRL vs 100 and 100 vs 200 n.s, CTRL vs 200 p=0.0002; others: p<0.0001 for all, except CTRL vs lat-A 0.1 µM p=0.0007. (C) Mean boundary speed over 3h 30'. Each dot represents a time-point and is color-coded as in (A) (p<0.0001, Kruskal-Wallis test for all). Dunn's multiple comparison test. The middle horizontal line represents the median and the black dot is the mean value. The stars above each treated condition compare it against the control, the stars in middle-top compare the 2 treated conditions. *** means p<0.001, **** means p<0.0001. (D) Table highlighting motile cell lines (faster than 100 µm / 8 h = 0.21 µm/min), their corresponding Δ (number of frames needed to travel 100 µm) and τ - Δ (number of frames in the RA movie).

when looking at boundary speed (Fig. 2.19C). Under blebbistatin, nocodazole and latrunculin-A spheroid spreading was decreased by at least a factor 2 (Fig. 2.19B). CK666 didn't alter any of the 3 motility modes (Fig. 2.20), while blebbistatin and

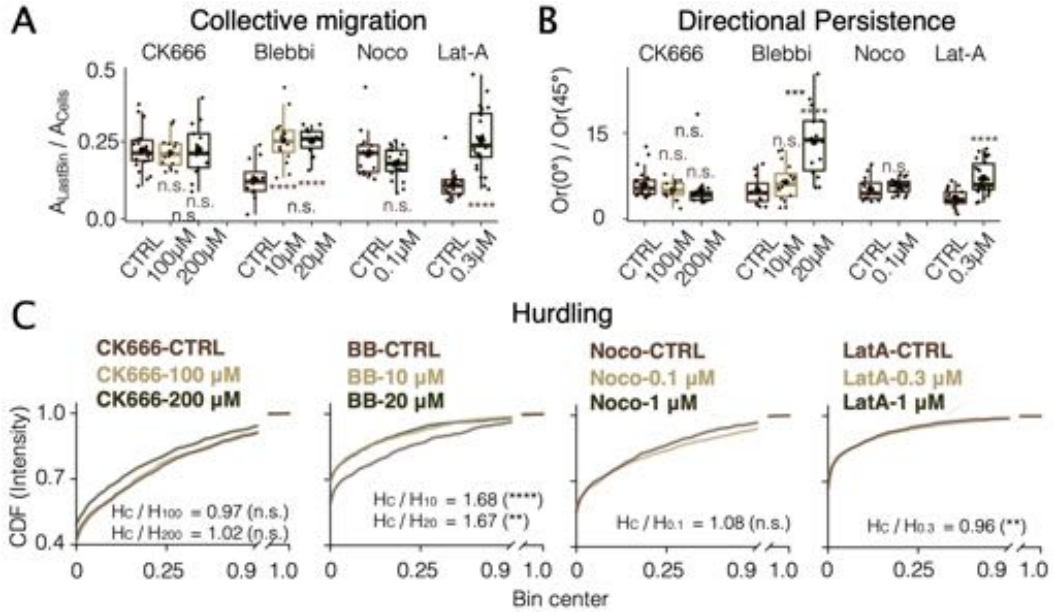

Figure 2.20: SP2G detects the different motility modes upon inhibition of Arp2/3, myosin II, microtubules and f-Actin.. (A) Collective migration for the motile conditions. It is visualized as the ratio between the area covered by the pixels belonging to the last bin of the histogram and the total number of pixels covered by the cells ($A_{LastBin}$ / A_{Cells}). Each dot represents a spheroid. One-way ANOVA for CK666 (n.s.) and blebbistatin (****) with Dunn's multiple comparison test. t-test for nocodazole and latrunculin-A. (B) Directional persistence for the motile conditions. It is visualized as the ratio between the orientation along 0° and along 45° (Or(0°) / Or(45°)). Each dot represents a spheroid. One-way ANOVA for CK666 (n.s.) and blebbistatin (****) with Dunn's multiple comparison test. t-test for nocodazole and latrunculin-A. (C) Hurdling is visualized as the CDF of the normalized mean intensity of the grid squares (image intensity is sampled in each square). The ratio indicates the relationship between the average mean intensities (the sum of the mean intensity from all the squares divided by the total number of squares) of the most hurdling against the others, in parenthesis the results of Kolmogorov-Smirnov tests: CK666-CTRL vs CK666-100 p=0.9926 (n.s.), CK666-CTRL vs CK666-200 p=0.6828 (n.s.), BB-CTRL vs BB10 p=5.3505e-05 (****), BB-CTRL vs BB-20 p=0.0019 (**) , Noco-CTRL vs Noco-0.1 p=0.3499 (n.s.), LatA-CTRL vs LatA-0.3 p=0.0087 (**). In (A) and (B), the middle horizontal line represents the median and the black dot is the mean value. The stars above each treated condition compare it against the control, the stars in middle-top compare the 2 treated conditions. *** means p<0.001, **** means p<0.0001.

latrunculin-A increased collective migration (Fig. 2.20A) and persistence (Fig. 2.20B) and decreased hurdling (Fig. 2.20C). Nocodazole didn't affect collective migration and directional persistence but slightly decreased hurdling (Fig. 2.20).

We then exposed SP2G to finer perturbations by stamping the gridded micropatterns coated with various laminin concentrations (400, 200, 100, 50, 25, 12.5, 6.25 µg/ml) and a blank condition (no laminin, only fluorescent dye) (Fig. 2.21). Spheroids didn't adhere in the blank and at lowest laminin concentration (6.25 µg/ml). Although a detailed look at phase contrast pictures is insufficient to detect differences (Fig. 2.21A-C), SP2G strikingly detected 3 regimes in NNI-21 migration: 400-200 µg/ml, 100-50 µg/ml, 25-12.5 µg/ml, which were the only 3 couples non-statistically significant (Kruskal-Wallis test) when performing Dunn's multiple comparison tests of diffusivity and boundary speed (Fig. 2.21E,F). SP2G measured no differences when analyzing the motility modes, except when comparing hurdling at 400 µg/ml and 12.5 µg/ml, probably because the same cell line is not affected by this subtle perturbation (Fig. 2.21H-J). Altogether, these results showed SP2G as capable of characterizing inter-patient heterogeneity in cell migration and under fine biochemical perturbations. Therefore, we were wondering whether we could also utilize SP2G as a tool for describing intra-patient heterogeneity in cell migration and motility modes starting from patient-derived, low passage samples.

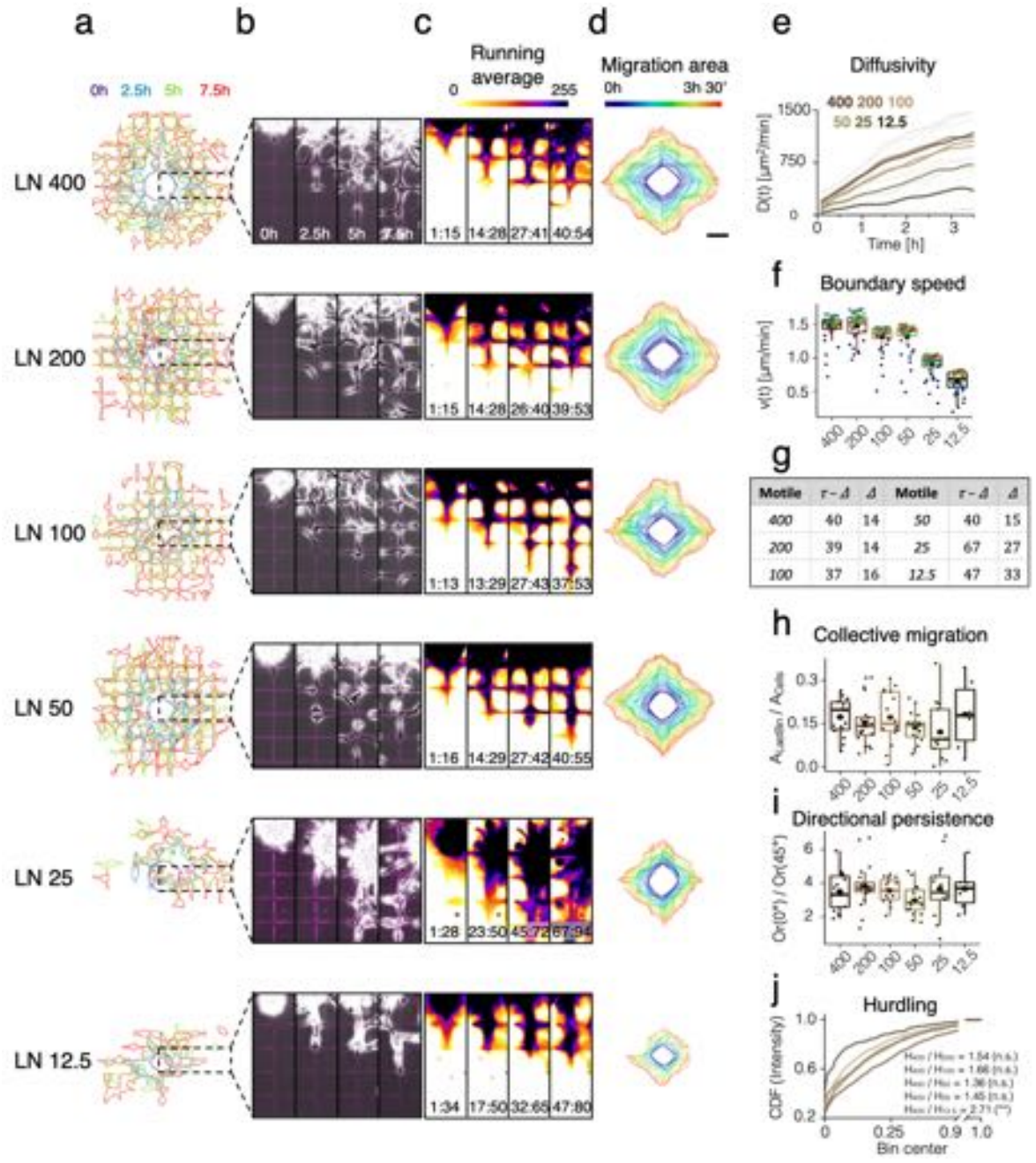

Motile	τ - Δ	Δ	Motile	τ - Δ	Δ
400	40	14	50	40	15
200	39	14	25	67	27
100	37	16	12.5	47	33

Figure 2.21: SP2G detects the different migratory tactics upon changes in laminin concentration on the substrate. (A) Micrograph highlighting cellular edges at 4 time points (0h, 2.5h, 5h, 7.5h) as the spheroid spreads. Time is color-coded as indicated. Here 6 conditions are tested: the gridded micropattern was printed with LN at 400, 200, 100, 50, 25, 12.5 µg/ml (n = 17, 20, 16, 17, 13, 6 spheroids). They are ranked from most to least LN concentrated. n = 3 independent experiments per condition. (B) Insets displaying cellular morphology at 0h, 2.5h, 5h, 7.5h. (C) Insets displaying the RA of the same ROI in (B). Image intensity is color-coded as indicated. The 4 insets are regularly spaced within the length of the RA movie. The time window Δ constituting the corresponding RA frame is indicated at the bottom of each inset. (D) Average polygon visualizing migration area. Its expansion in time is color-coded as indicated. (E) Diffusivity over 3 h 30' ($p<0.0001$,

Kruskal-Wallis test). Dashed lines are the standard deviation. Dunn's multiple comparison test: 400 vs 25 / 12.5, 200 vs 25 / 12.5 and 100 / 50 vs 12.5 $p<0.0001$; 100 / 50 vs 25 and 25 vs 12.5 $p<0.05$; others n.s. (F) Mean boundary speed over 3h 30'. Each dot represents a time-point and is color-coded as in (D) ($p<0.0001$, Kruskal-Wallis test for all). Dunn's multiple comparison test: 400 vs 25 / 12.5, 200 vs 25 / 12.5 and 100 / 50 vs 12.5 $p<0.0001$; 100 vs 25 $p=0.0001$; 200 vs 100 $p=0.0086$; 400 vs 100 / 50 and 200 vs 50 $p<0.05$; others n.s. (G) Table highlighting motile cell lines (faster than 100 µm / 8 h = 0.21 µm/min), their corresponding Δ (number of frames needed to travel 100 µm) and τ - Δ (number of frames in the RA movie). (H) Collective migration for the motile conditions. It is visualized as the ratio between the area covered by the pixels belonging to the last bin of the histogram and the total number of pixels covered by the cells ($A_{LastBin}$ / A_{Cells}). Each dot represents a spheroid. One-way ANOVA (n.s.) with Dunn's multiple comparison test (all n.s.). (I) Directional persistence for the motile conditions. It is visualized as the ratio between the orientation along 0° and along 45° (Or(0°) / Or(45°)). Each dot represents a spheroid. One-way ANOVA (n.s.) with Dunn's multiple comparison test (all n.s.). (J) Hurdling is visualized as the CDF of the normalized mean intensity of the grid squares (image intensity is sampled in each square). Kolmogorov-Smirnov test. The ratio indicates the relationship between the average mean intensities (the sum of the mean intensity from all the squares divided by the total number of squares) of the most hurdling (LN400) against the others, in parenthesis the results of Kolmogorov-Smirnov tests: LN400 vs LN200 $p=0.4496$ (n.s.), LN400 vs LN100 $p=0.1976$ (n.s.), LN400 vs LN50 $p=0.4496$ (n.s.), LN400 vs LN25 $p=0.2659$ (n.s.), LN400 vs LN12.5 $p=0.0054$ (**). All the bars are 100 µm. In all the boxplots, the middle horizontal line represents the median and the black dot is the mean value.

2.5 SP2G reveals heterogeneity in the migratory tactics adopted by glioblastoma sub-populations isolated from patient-derived cell lines

Heterogeneity in GBM has been characterized both inter- [45] and intra-patient [46]. As introduced in section 1.2 of this PhD thesis, these 2 landmark papers pinpointed how GBM tumors are diseases with intrinsic properties that differ not only from patient to patient, but from cell to cell within the same tumor. Apart from correlation between patient survival in the Cytosine-Phosphate-Guanine Island Methylator Phenotype (G-CIMP) in the proneural subtype and between MGMT DNA methylation status and response to radio/chemotherapeutic treatments in the classical subtype, GBM tumors never share a universal biomarker or mutation, despite EGF-Receptor is the only gene locus often displaying focal amplification across patients. Similarly, cells in the same tumor express diverse transcriptional programs related to oncogenic signaling, proliferation, complement/immune response, and hypoxia, sharing only a continuum of stemness-related expression states that endows GBM with resistance to therapies by repairing DNA damages caused thereof [43]. Furthermore, heterogeneous GBM displayed difference in their genomic [48, 49], epigenetic [50, 51] and transcriptomic [52] profiles, which are mutating under therapy [53] and largely maintained when cultured *in vitro* [54]. This literature confirmed how sub-populations do exist in GBM tumors and possess different molecular signatures: whether this heterogeneity is reflected in cell migration and motility modes is still unknown.

Using SP2G, we *de novo* characterized 2 patient-derived GBM cell lines (the GBM7; and GBM22). Intriguingly, we were able to respectively test 5 and 6 of their sub-populations, which we isolated from the original heterogeneous bulk. We initially tested the GBM7 bulk and we observed a pool of motile cells tearing apart the initial spheroid into 3 daughter spheroids, as if motile cells were carrying *"hitchhiking"* non-

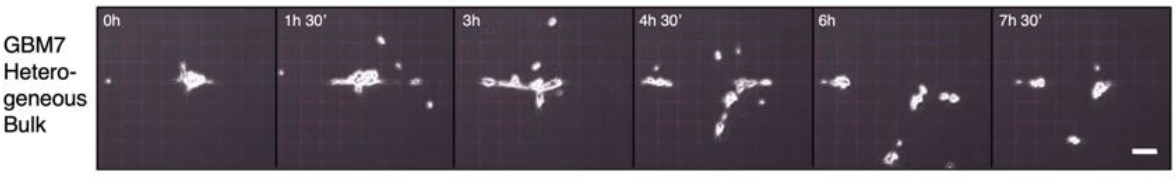

Figure 2.22: SP2G at the indicated time-points of the patient-derived cell line GBM7 heterogeneous bulk.

motile cells (Fig. 2.22). This observation suggested that the GBM7 cell line might be composed of different cell populations.

To test this hypothesis, we performed serial dilutions of the heterogeneous GBM7 bulk in 96-well plates such that in the last row we had 1 cell, in the last-last row 2 cells, then 4 cells, 8, 16, 32, 64, and 128 (12 replicate-wells per density). Given that we maintained GBM cells in stem, non-adherent conditions as spheroid aggregates, we assumed that the presence of 1 spheroid was originated from a single mother cell that gave rise to a clonal sub-population. Conversely, the presence of 2 or more spheroids entailed that originally there were 2 or more cells, potentially diverse. In this case the content of that well was discarded. With this method we then isolated several sub-populations and analyzed their phenotype with SP2G. From the GBM7 cell line, we analyzed 3 motile sub-populations (from most to least motile: #09, #01, #07) and 2 non-motile (#03, #02) (Fig. 2.23).

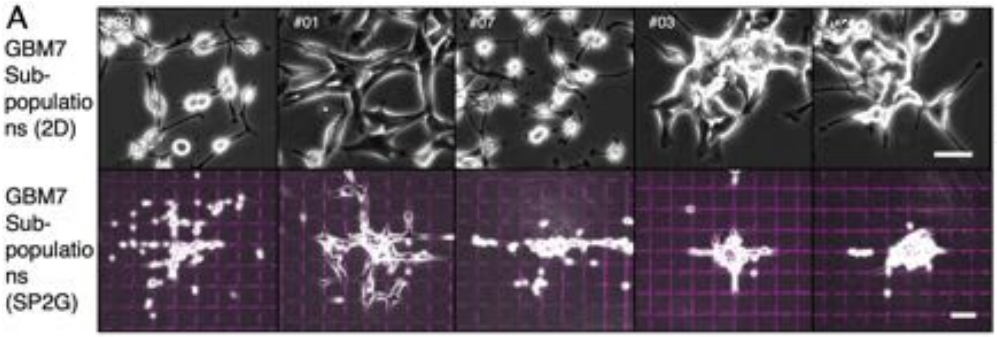

Figure 2.23: SP2G at the indicated time-points of the patient-derived cell line GBM7 sub-populations. (A), Phase-contrast pictures of the GBM7 sub-populations #09, #01, #07, #03, #02 cultured in petri-dishes (top, bar is 50 µm). SP2G at 8 hours (bottom, bar is 100 µm). (B) Table highlighting the motile sub-populations (faster than 100 µm / 8 h = 0.21 µm/min) upon testing with SP2G, their corresponding Δ (number of frames needed to travel 100 µm) and τ - Δ (number of frames in the RA movie).

In the motile clones, the easiest-to-spot differences can be seen just by looking at cell morphologies (Fig. 2.23A). Cells from #09 and #07 had small cell bodies that rounded up in correspondence of the nucleus and two thin long processes. Differently, cells from #01 had a bulkier morphology, they looked flatter and more evenly spread, being their lamellipodia much larger than #09 and #07. The non-motile clones clustered in islands, with #03 aggregating in adherent spheroids. In particular, #03 had a bulky shape and larger processes than #02, which seemed able to extend longer and thinner lamellipodia.

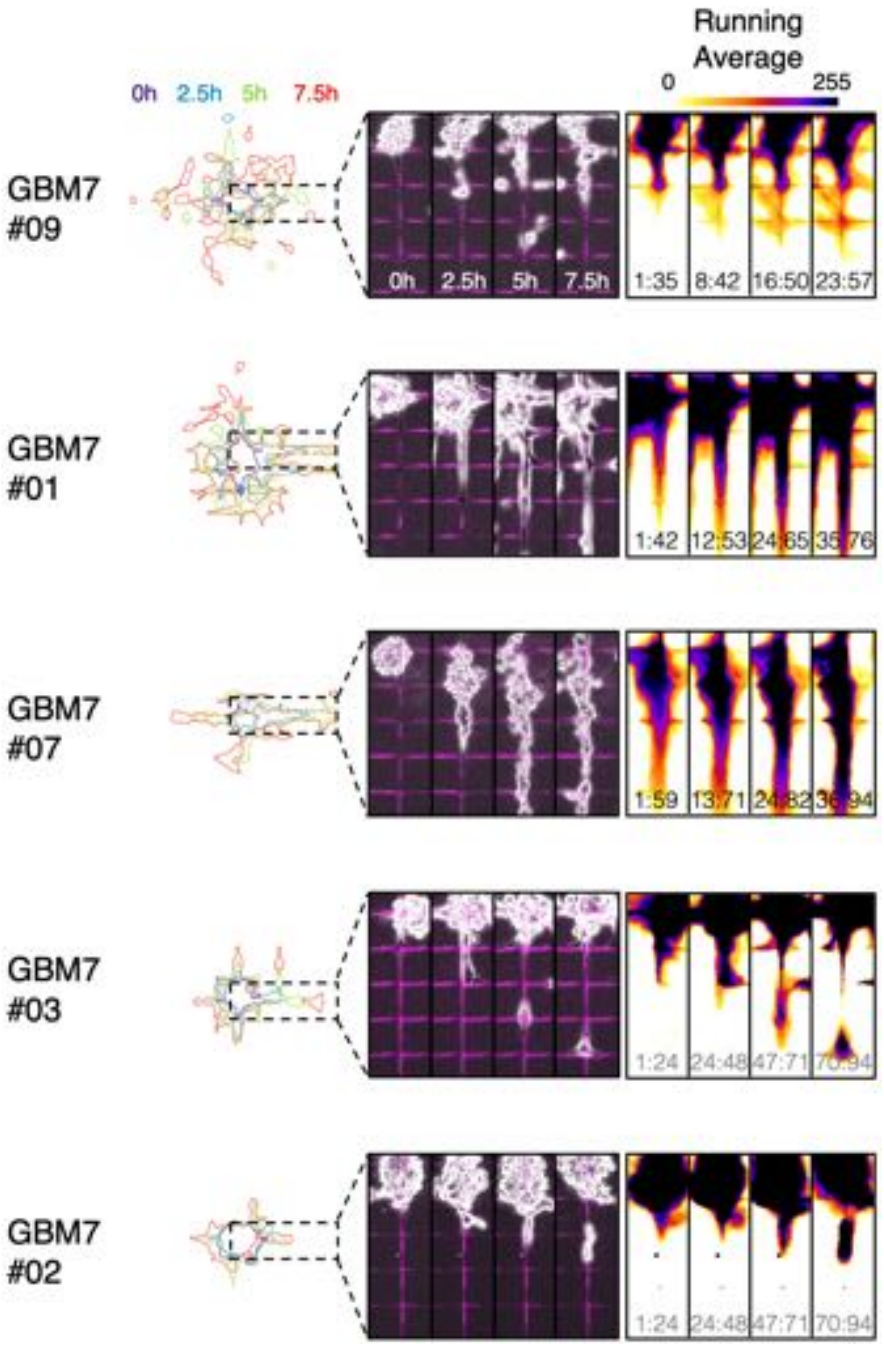

Figure 2.24: SP2G reveals heterogeneity in the migratory tactics adopted by glioblastoma sub-populations isolated from the GBM7 patient-derived cell line. (Left) Micrograph highlighting cellular edges at 4 time points (0h, 2.5h, 5h, 7.5h) as the spheroid spreads. Time is color-coded as indicated. Here 5 cell lines are tested and ranked from most to least invasive: #09, #01, #07, #03, #02 (n = 22, 23, 20, 22, 22 spheroids. n = 3 independent experiments each). (Middle) Insets displaying cellular morphology at 0h, 2.5h, 5h, 7.5h. (Right) Insets displaying the RA of the same ROI in (Middle). Image intensity is color-coded as indicated. The 4 insets are regularly spaced within the length of the RA movie. The time window Δ constituting the corresponding RA frame is indicated at the bottom of each inset: for the non-motile cells is by default in grey colour and created with $\tau = 94$, $\Delta = 24$.

When tested with SP2G, the 5 sub-populations exhibited different behaviors, particularly in the motile ones (Fig. 2.24). As highlighted by the micrographs in Figure 2.24-Left, #09 migrated out of the spheroid as small single cells that homogeneously covered its surroundings, while #01 and #07 formed hundreds-of-microns long strands that were directly in contact with the spheroid. This feature is clearly evident when visualizing the RA movie (Fig. 2.24, Right) Among these, #01 displayed a more epithelial phenotype capable of bridging the gaps of the grid, in line with the flatter and bulkier single-cell morphology (Fig. 2.23A), while the strands in #07 were irregular buds in which the single cells seemed more rounded-up.

As a further validation of this migration behavior, we then tested the 5 populations in the brain slice assay and, strikingly, the motility behavior reflected the results obtained with SP2G (Fig. 2.25). Spheroids from #09, #01, #07 invaded the brain slice, with #01 forming collective strands as in SP2G *in vitro* setup. Due to tissue opacity, it is hard to deduce conclusions about the motility modes from #09 and #07. Nevertheless, #03 and #02 were poorly motile, similarly to the results obtained from SP2G.

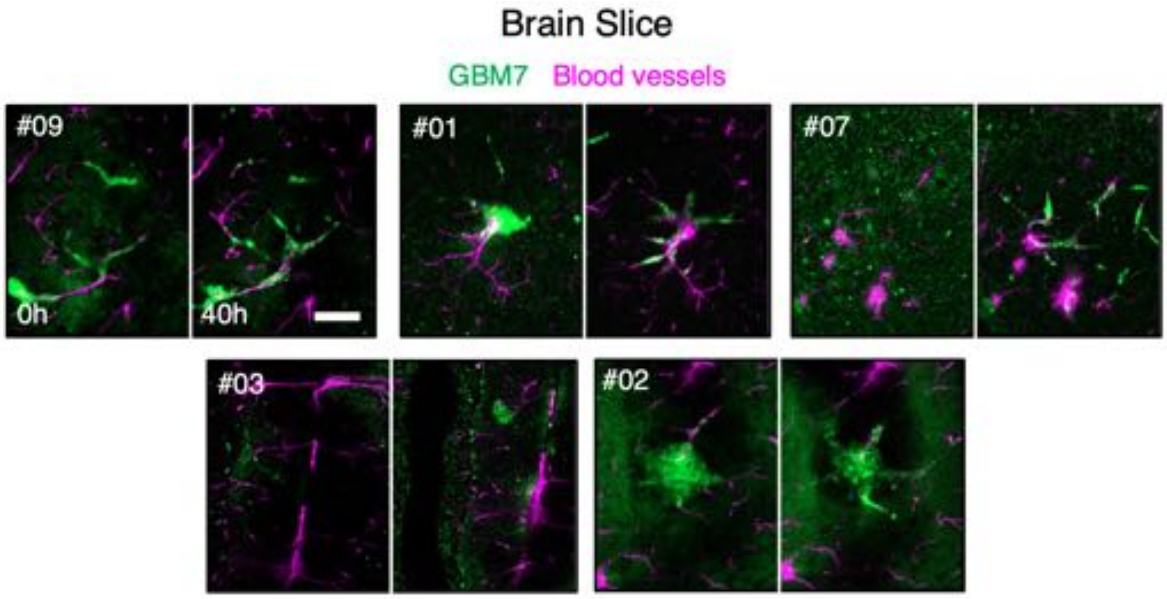

Figure 2.25: Speroid Spreading of GBM7 sub-populations (green, DiOC6 dye) lent against an *ex-vivo* brain slices. The blood vessels are in magenta colour (Dil dye, intracardial injection). 2 time points per sub-population are shown, 0 h and 40 h. From left to right, top: #09, #01, #07. From left to right, bottom: #03, #02. Bar is 100 µm.

The graphical and numerical outputs by SP2G for characterizing cell migration are summarized in Table 2.3 and in Figure 2.26.

	#09	#01	#07	#03	#02
D(3h 30') [µm^2/min]	363 ± 245	273 ± 197	178 ± 128	36 ± 64	34 ± 41
v(0 : 3h 30') [µm/min]	0.58 ± 0.15	0.38 ± 0.12	0.35 ± 0.08	0.12 ± 0.03	0.17 ± 0.04

Table 2.3: Summary of the numerical outputs provided by SP2G for cell migration of the GBM7 sub-populations. D(3h 30') is the value of diffusivity sampled at 3h 30', v(0 : 3h 30') is the boundary speed averaged in the interval 0 : 3h 30'. Data are expressed as mean ± s.d.

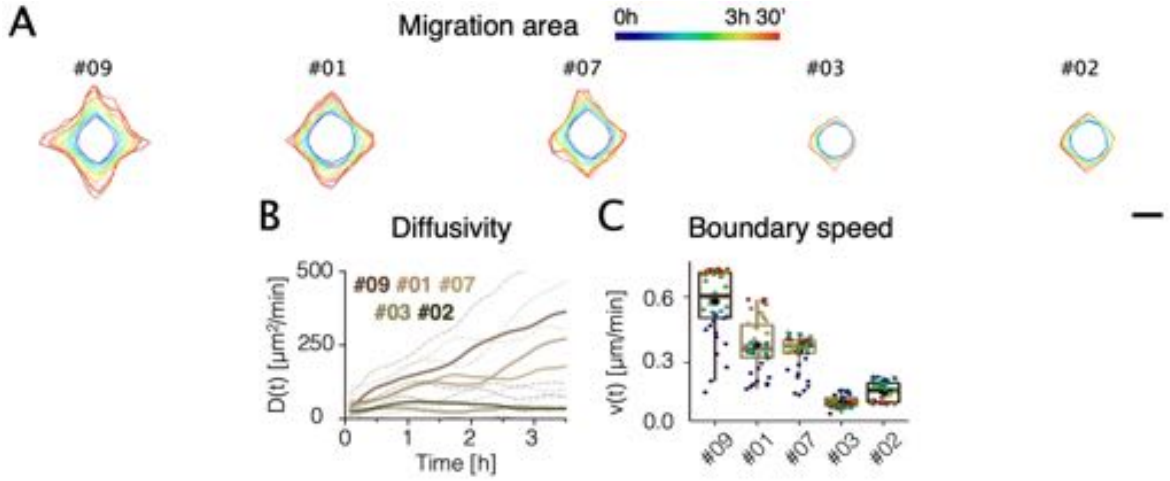

Figure 2.26: SP2G detects differences in the migration of GBM7 sub-populations. (A) Average polygon visualizing migration area. Its expansion in time is color-coded as indicated. Bar is 100 µm. (B) Diffusivity over 3 h 30' ($p<0.0001$, Kruskal-Wallis test). Dashed lines are the standard deviation. Dunn's multiple comparison test: #09 vs #03 / #02, #01 vs #03 / #02, #07 vs #03 / #02 $p< 0.0001$; others n.s. (C) Mean boundary speed over 3h 30'. Each dot represents a time-point and is color-coded as in (A) ($p<0.0001$, Kruskal-Wallis test). Dunn's multiple comparison test: #09 vs #03 / #02, #01 vs #03 / #02, #07 vs #03 / #02 $p<0.0001$; #09 vs #01 $p=0.0054$; #09 vs #07 $p=0.0013$; others n.s. The middle horizontal line represents the median and the black dot is the mean value.

When analyzing the motility modes, SP2G detected lower collective migration values in clone #09 compared to the other sub-populations, in line with the considerations made when describing the micrographs in Figure 2.24-Left. Similarly, clone #01 was the most hurdler. SP2G detected no significant changes in directional persistence between the 3 motile clones (Fig. 2.27).

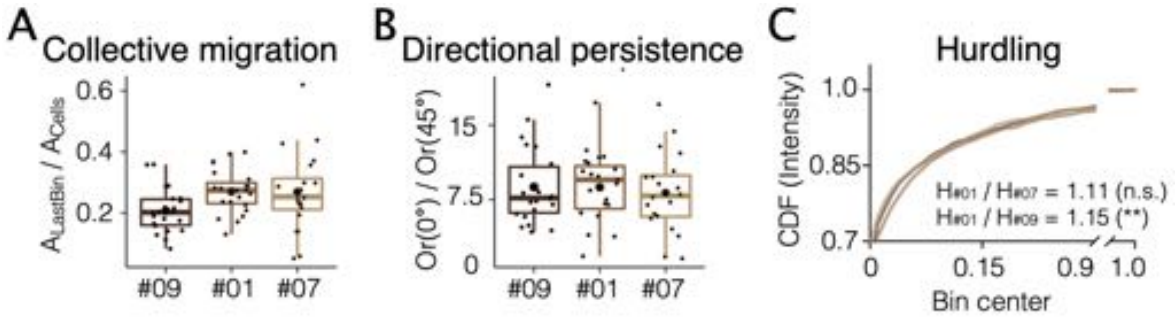

Figure 2.27: SP2G detects differences in the motility modes of GBM7 sub-populations. (A) Collective migration for the motile #09, #01 and #07. It is visualized as the ratio between the area covered by the pixels belonging to the last bin of the histogram and the total number of pixels covered by the cells ($A_{LastBin}$ / A_{Cells}). Each dot represents a spheroid. p=0.0458, ordinary one-way ANOVA. Multiple comparisons all n.s. (#09 vs #01 p=0.0696; #09 vs #07 p=0.0903). (B) Directional persistence for the motile #09, #01 and #07. It is visualized as the ratio between the orientation along 0° and along 45° (Or(0°) / Or(45°)). Each dot represents a spheroid. n.s, ordinary one-way ANOVA. Multiple comparisons all n.s. (C) Hurdling is visualized as the CDF of the normalized mean intensity of the grid squares (image intensity is sampled in each square). The ratio indicates the relationship between the average mean intensities (the sum of the mean intensity from all the squares divided by the total number of squares) of the most hurdling (#01) against the others. The results of Kolmogorov-Smirnov tests between #01 vs #07 p=0.7992 (n.s.), #01 vs #09 p=0.0087 (**) are indicated in parenthesis. In all the boxplots, the middle horizontal line represents the median and the black dot is the mean value.

With the same technique described at the beginning of this section we isolated 4 motile and 2 non-motile sub-populations from the GBM22 heterogeneous bulk. The GBM22 heterogeneous bulk, when tested with SP2G, did not break apart into various small spheroids as the GBM7 case. However, the pictures in Figures 2.28 highlights how smaller cells are at the invasive front, while other bulkier and flatter

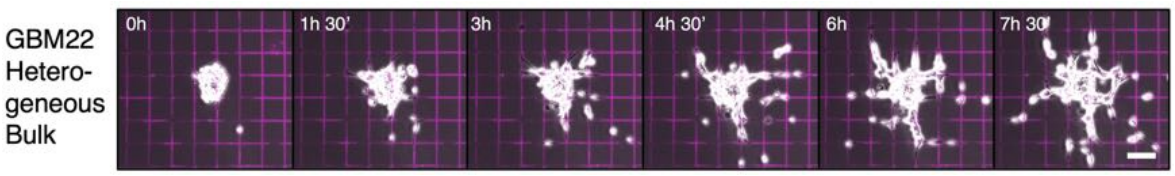

Figure 2.28: SP2G at the indicated time-points of the patient-derived cell line GBM22 heterogeneous bulk.

remained closer to the spheroid.

When we isolated the sub-populations with serial dilutions in 96-well plates and plated them on 2D flat substrates, we recorded how cells from #14-#19-#01 had small cell bodies and thin long processes, while cells from #08 formed several cell-to-cell interconnections. Cells from #16 and #07 grew as islands, and #07 clumped in spheroids and from #16 cells looked flatter and more spread than the other sub-populations (Fig. 2.29).

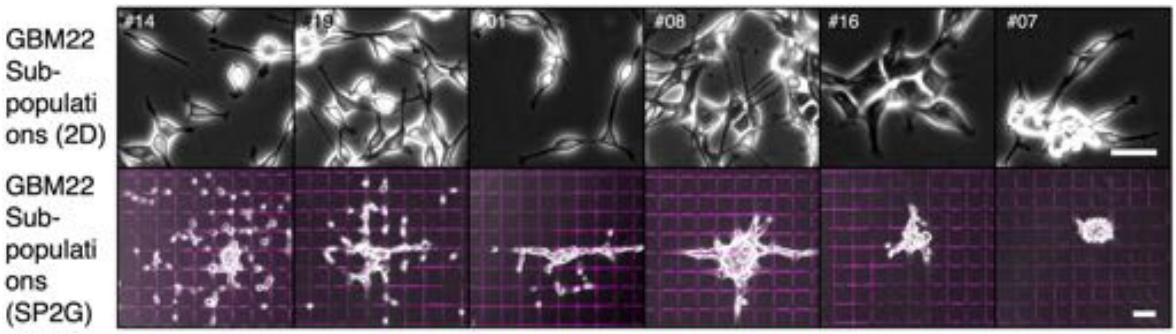

Figure 2.29: SP2G at the indicated time-points of the patient-derived cell line GBM22 sub-populations. (A), Phase-contrast pictures of the GBM22 sub-populations #14, #19, #01, #08, #16, #07 cultured in petri-dishes (top, bar is 50 µm). SP2G at 8 hours (bottom, bar is 100 µm).

We then proceeded at testing with SP2G the batch of sub-populations isolated from the GBM22.

A quick look at the micrographs (Fig. 2.30,Left) readily shows how #14 is the most motile sub-population, evenly covering the surroundings of the spheroid as a set of small and stochastically moving cells. #19 seem to be similar in morphology and motility modes, its migration rate looks smaller though. As pointed by RA pictures (Fig. 2.30,Right), #01 and #08 look like forming collective strands, with #08 capable of protruding long cell-to-cell interconnections that, in #01, are more irregular as cells grows as disorganized bunches. #16 and #07 did not move in SP2G conditions.

As SP2G provided numerical outputs, it detected a clear trend from the most motile until the non-motile population when quantifying diffusivity and boundary speed (Fig. 2.31). The numerical outputs are summarized in Table 2.4.

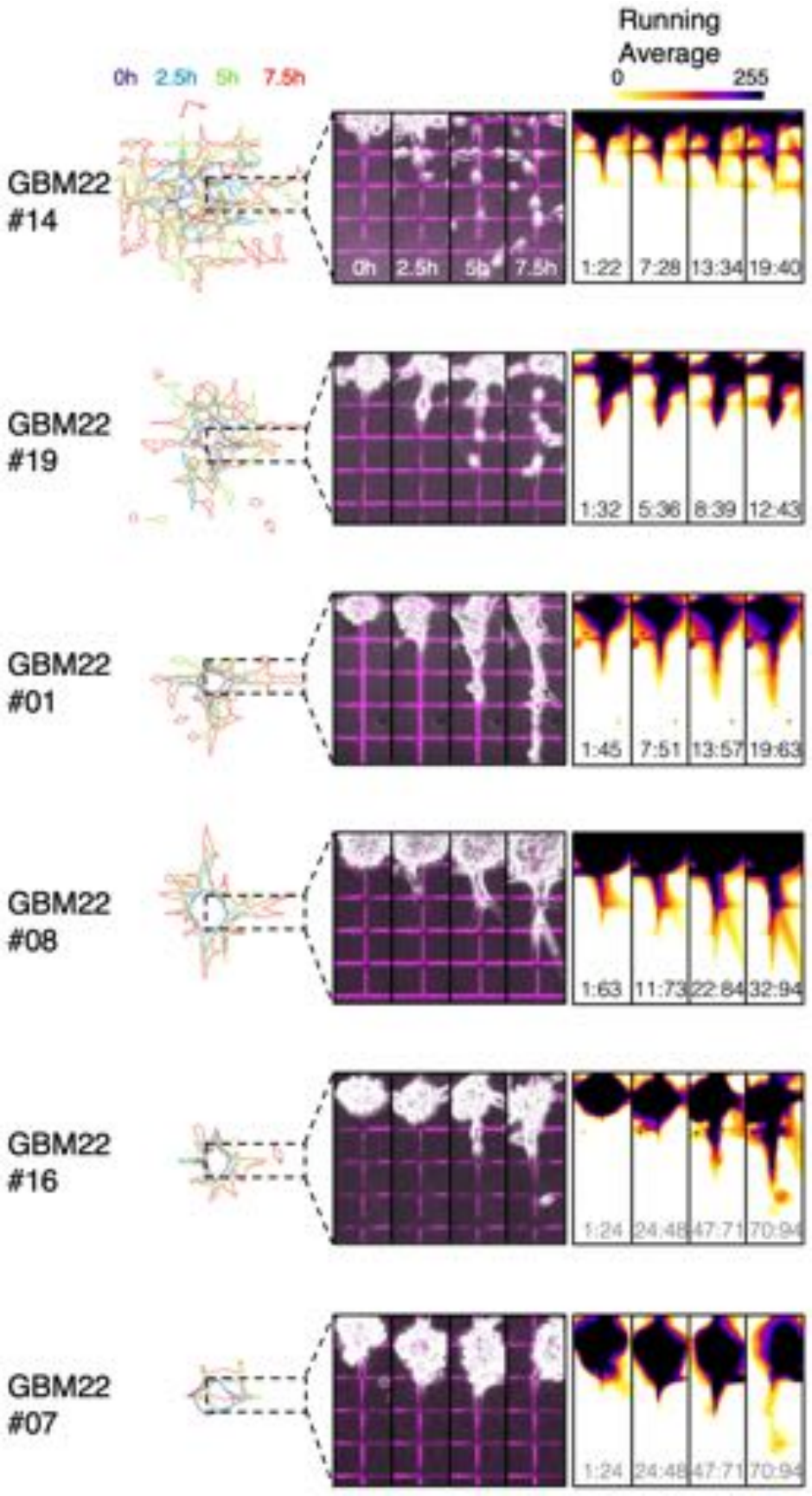

Figure 2.30: SP2G reveals heterogeneity in the migratory tactics adopted by glioblastoma sub-populations isolated from the GBM22 patient-derived cell line. Full caption is displayed in the next page.

Figure 2.30: SP2G reveals heterogeneity in the migratory tactics adopted by glioblastoma sub-populations isolated from the GBM22 patient-derived cell line (continued). (Left) Micrograph highlighting cellular edges at 4 time points (0h, 2.5h, 5h, 7.5h) as the spheroid spreads. Time is color-coded as indicated. Here 6 cell lines are tested and ranked from most to least invasive: #14, #19, #01, #08, #16, #07 (n = 15, 15, 14, 15, 13, 11 spheroids. n = 2 independent experiments each). (Middle) Insets displaying cellular morphology at 0h, 2.5h, 5h, 7.5h. (Right) Insets displaying the RA of the same ROI in (Left). Image intensity is color-coded as indicated. The 4 insets are regularly spaced within the length of the RA movie. The time window Δ constituting the corresponding RA frame is indicated at the bottom of each inset: for the non-motile cells is by default in grey colour and created with $\tau = 94$, $\Delta = 24$.

	#14	#19	#01	#08	#16	#07
D(3h 30') [µm^2/min]	985±315	440±222	220±128	108±67	34±49	26±32
v(0 : 3h 30') [µm/min]	0.98±0.31	0.65±0.20	0.41±0.15	0.27±0.03	0.13±0.03	0.11±0.02

Table 2.4: Summary of the numerical outputs provided by SP2G for cell migration of the GBM22 sub-populations. D(3h 30') is the value of diffusivity sampled at 3h 30', v(0 : 3h 30') is the boundary speed averaged in the interval 0 : 3h 30'. Data are expressed as mean ± s.d.

For motility modes, SP2G classified #08 as the most collectively migrating population (Fig. 2.32A), coherently with the RA pictures in Figure 2.30-Right. As illustrated while describing the micrographs of Figure 2.30-Left, #14 was quantified as as the most hurdling (Fig. 2.32C). Finally, SP2G detected #01 as the most persistent (Fig. 2.32B), in line with the long strands that forms as the spheroid spreads (Fig. 2.30).

In conclusion, these results showed that sub-populations hidden in patient-derived samples spanned a range of motility comparable to those from different patients (Fig. 2.16) and that we developed a tool capable of detecting differences in cell migration and motility modes as several samples are tested with it.

Next, we hypothesized whether these differences in intra-patient cell motility and motility modes could be reflected in their transcriptional profile and hence we investigated their bulk RNA expression.

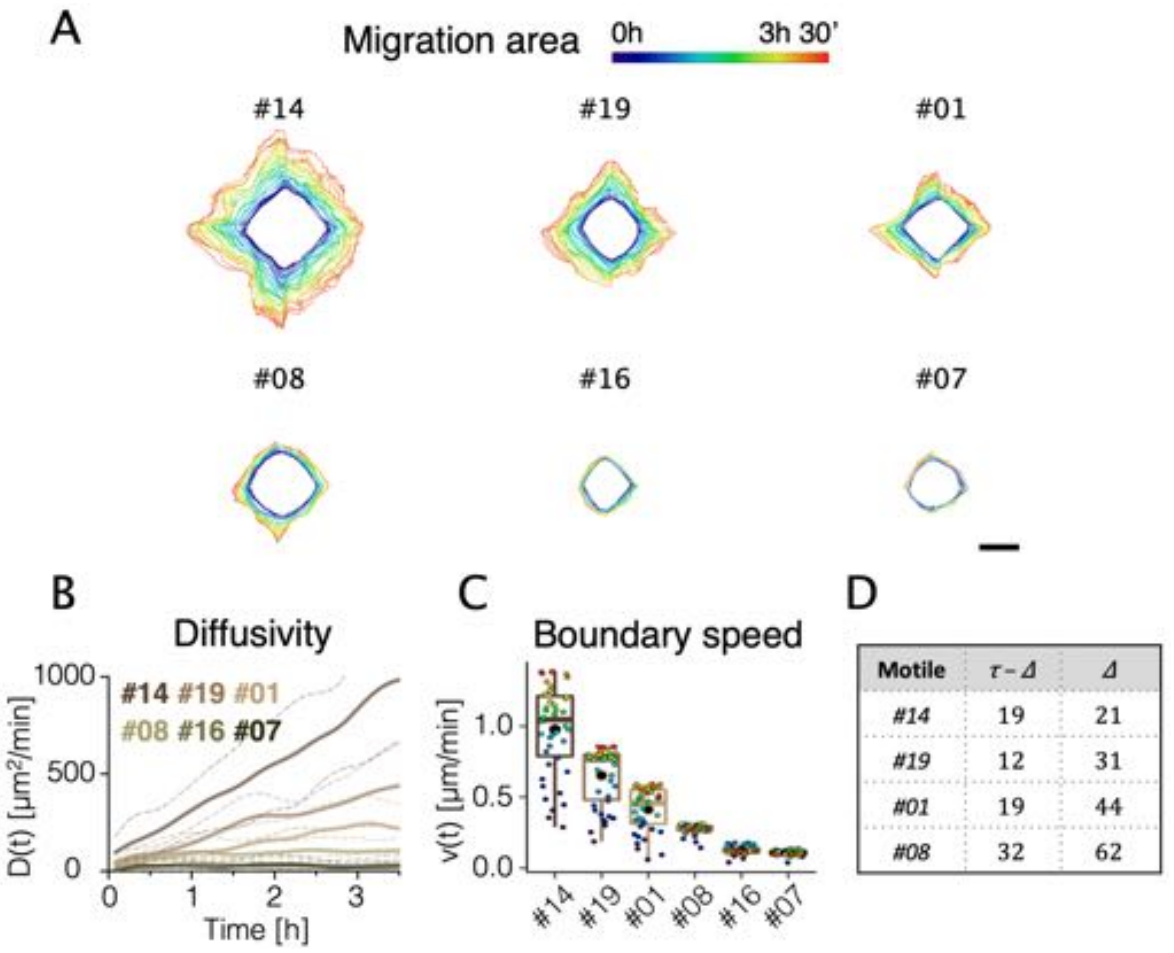

Figure 2.31: SP2G detects differences in the migration of GBM22 sub-populations. (A) Average polygon visualizing migration area. Its expansion in time is color-coded as indicated. Bar is 100 µm. (B) Diffusivity over 3 h 30' ($p<0.0001$, Kruskal-Wallis test). Dashed lines are the standard deviation. Dunn's multiple comparison test: #14 vs #01 / #08 / #16 / #07, #19 vs #16 / #07, #01 vs #16 / #07, #08 vs #16 / #07 $p<0.0001$; #19 vs #08 $p=0.0051$; others n.s. (C) Mean boundary speed over 3h 30'. Each dot represents a time-point and is color-coded as in (A) ($p<0.0001$, Kruskal-Wallis test). Dunn's multiple comparison test: #14 vs #01 / #08 / #16 / #07, #19 vs #16 / #07, #01 vs #16 / #07, #08 vs #07 $p<0.0001$; #19 vs #08 $p=0.0001$; #08 vs #16 $p=0.0017$; others n.s. (D) Table highlighting the motile sub-populations (faster than 100 µm / 8 h = 0.21 µm/min), their corresponding Δ (number of frames needed to travel 100 µm) and τ - Δ (number of frames in the RA movie). In all the boxplots, the middle horizontal line represents the median and the black dot is the mean value.

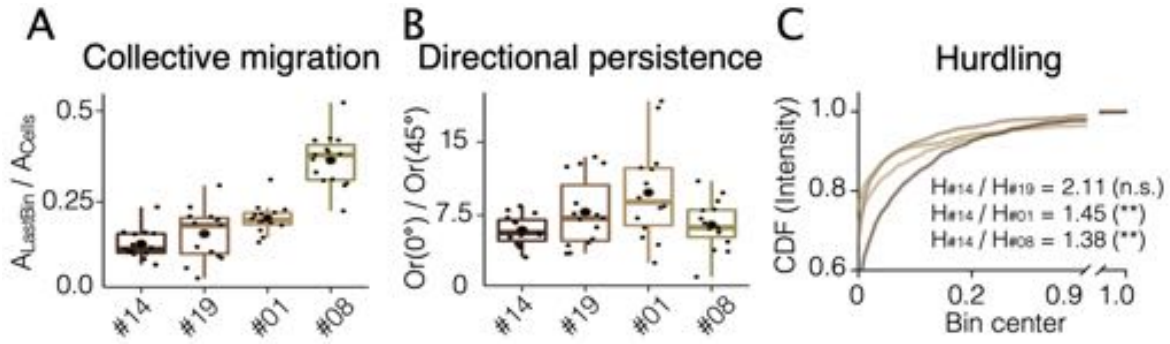

Figure 2.32: SP2G detects differences in the motility modes of GBM22 sub-populations. (A) Collective migration for the motile #14, #19, #01 and #08. It is visualized as the ratio between the area covered by the pixels belonging to the last bin of the histogram and the total number of pixels covered by the cells ($A_{LastBin}$ / A_{Cells}). Each dot represents a spheroid. $p<0.0001$, ordinary one-way ANOVA. Multiple comparisons: #08 vs #14 / #19 / #01 $p<0.0001$; #01 vs #14 $p=0.0085$; others n.s. (B) Directional persistence for the motile #14, #19, #01 and #08. It is visualized as the ratio between the orientation along 0° and along 45° (Or(0°) / Or(45°)). Each dot represents a spheroid. $p=0.0134$, ordinary one-way ANOVA. Multiple comparisons: #01 vs #08 / #14 $p<0.05$; others n.s. (C) Hurdling is visualized as the CDF of the normalized mean intensity of the grid squares (image intensity is sampled in each square). Kolmogorov-Smirnov tests: #14 vs #19 $p=0.0715$ (n.s.), #14 vs #01 $p=0.0019$ (**), #14 vs #08 $p=0.0011$. The ratio indicates the relationship between the average mean intensities (the sum of the mean intensity from all the squares divided by the total number of squares) of the most hurdling (#14) against the others. In all the boxplots, the middle horizontal line represents the median and the black dot is the mean value.

2.6 Transcriptomic analysis of GBM7 sub-populations validates intra-patient heterogeneity highlighted with SP2G

To further characterize the sub-populations from our glioblastoma patient-derived samples and gain insights in the molecular players that might differentiate the clones that composed the original heterogeneous bulk, we extracted the RNA from the 5 sub-population isolated from the cell line GBM7. We hence profiled their transcriptional landscape using RNA-sequencing (RNA-seq), having as ultimate goal to correlate their transcriptional profile with their motile phenotype.

When working with RNA-seq data, it is challenging to simultaneously visualize tens of millions of reads in a single graph on a single graph. Therefore, we adopted a dimension reduction approach, Principal Component Analysis (PCA), and each sub-population was projected in the resulting feature space. Interestingly, we found that the motile group (clones #01, #07 and #09) and the non-motile one (clones #02, #03) occupied distinct regions in the feature space (Fig. 2.33), suggesting that the 2 groups might have different molecular signatures that correlated with their motile behavior.

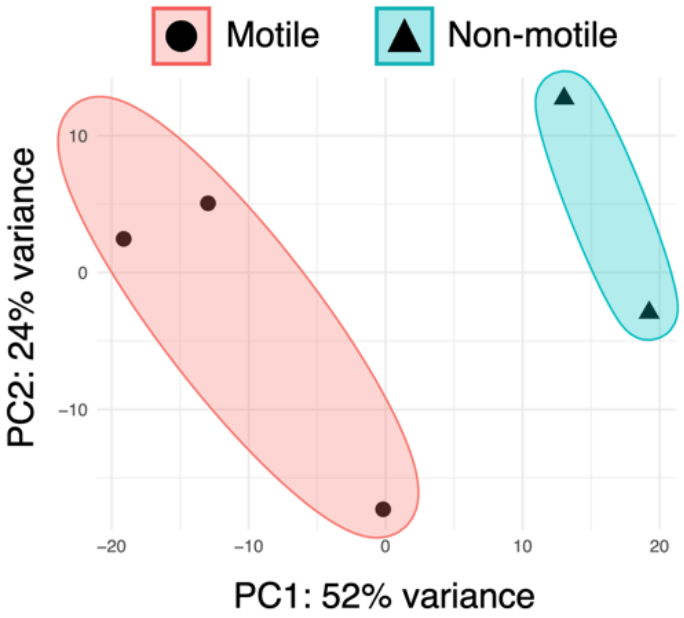

Figure 2.33: PCA showing segregation of the 5 GBM7 sub-population in motile (red) and non-motile (blue) groups.

To further investigate this aspect, we performed Gene Set Enrichment Analy-

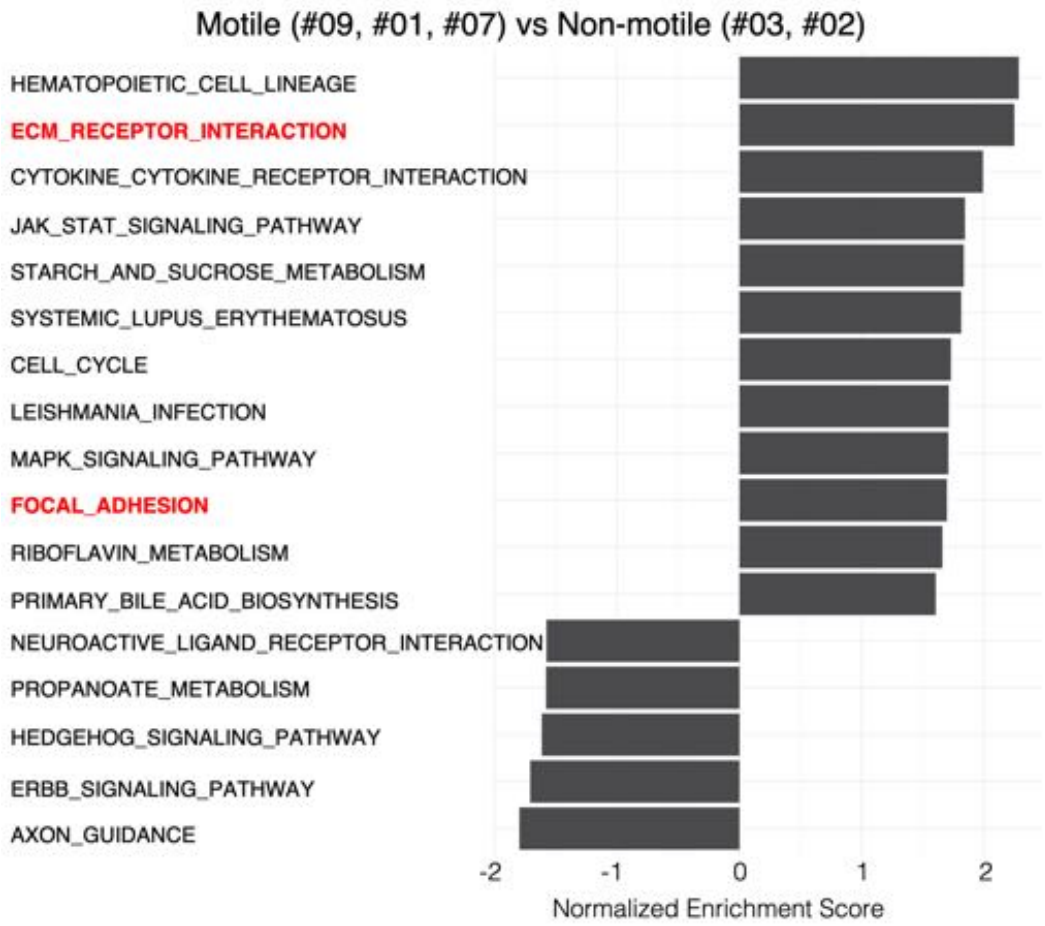

Figure 2.34: GSEA of differentially expressed genes in the motile group (#09, #01, #07) vs non-motile ones (#03, #02). GSEA was performed using the Kyoto Encyclopedia of Genes and Genomes (KEGG) gene set in the GSEA molecular signatures database. Moderated t-statistic was used to rank the genes. Reported are Normalized Enrichment Scores of enriched pathways.

sis (GSEA) of differentially expressed genes in motile versus non-motile conditions, which, among others, showed enrichment in the ECM-receptor interaction and FA pathways (Fig. 2.34). Both of these pathways are related with cell motility that, in general, is driven by interactions with ECM and FA expression [77, 140].

Therefore, we hypothesized that the expression of key integrins could differentiate between motile and non-motile sub-populations. To this extent, z-score of expression levels of integrin genes extrapolated from RNA-seq data indicated that the laminin-binding integrins (particularly ITGA1, ITGA3, ITGA6) were enriched in the motile clones compared to the non-motile. Conversely, the fibronectin-binding integrins were either poorly expressed or uncorrelated to the motility behavior of the cells (Fig. 2.35). These results were confirmed by quantitative PCR (qPCR) analysis, showing

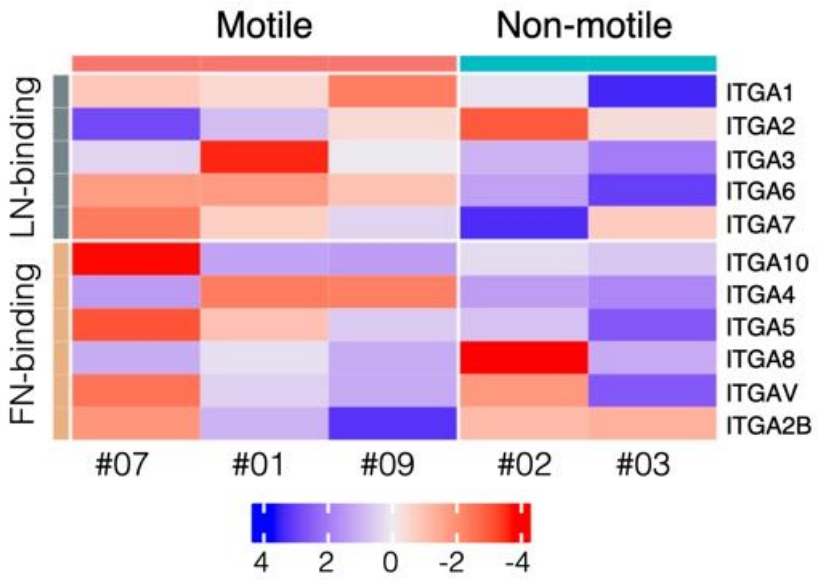

Figure 2.35: Heatmap representing z-score of expression levels of integrins. Laminin-binding integrins (ITGA1,2,3,6,7,10) are enriched in the motile clones.

that the laminin-binding integrins ITGA3 and ITGA6 were highly enriched in the motile clones while the fibronectin-binding integrin ITGAV was not (Fig. 2.36).

To gain insights at the protein level, we confirmed the results from the RNA level by western blot (Fig. 2.37): the protein level of the laminin-binding integrin ITGA6 were much higher in the motile #09, #01, #07 than in the non-motile #03, #02, whereas the fibronectin-binding integrin ITGAV were constant throughout the 5 clones.

Taken together, these results validate the motile versus non-motile classification made with SP2G and provide insights on the molecular determinants that character-

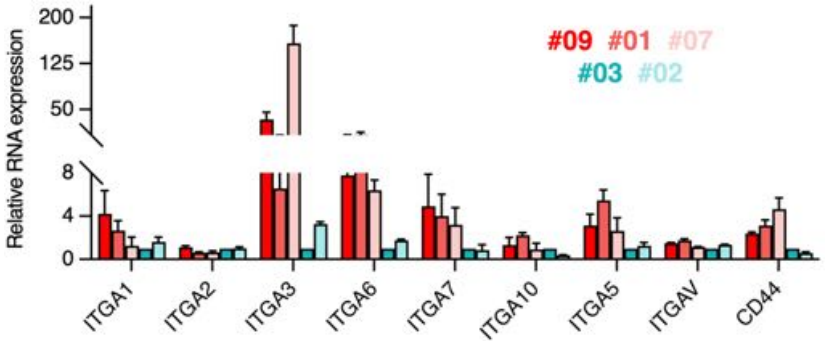

Figure 2.36: Bar plot of mRNA expression levels of ITGA1, ITGA2, ITGA3, ITGA5, ITGA6, ITGA7, ITGA10, ITGAV, and CD44 determined by qRT-PCR in the 5 GBM7 sub-populations. The data are normalized over the expression in clone #03. n=3 independent experiments each.

ize GBM intra-patient heterogeneity in cell motility.

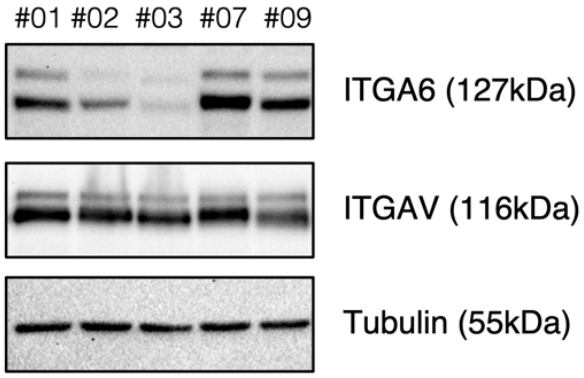

Figure 2.37: Integrin alpha6 is upregulated in motile clones compare to non-motile. Expression of ITGA6, ITGAV and tubulin in total extracts of the indicated cell lines growing as adherent monolayers on laminin-coated plates.

2.7 Preliminary studies of functional cellular networks validate the motility modes detected by SP2G

As introduced in section 1.3, glioblastoma cells can form large functional networks via long connecting bridges that help cells to protect themselves from damages such as radiation [122, 125]. These networks allow communications among neighboring cells via sub-cellular structures, namely the TM and the TNT [132]. Key molecular players identified throughout the years are GAP43, which is enriched at the tips of TMs, and CX43, responsible for the stability of the gap junctions, which are the junction formed when TMs successfully bridge neighboring cells. Moreover, p120-catenin, a protein involved in the stability of adherens junctions, has been identified as a central hub enabling dynamic cell–cell interactions and network infiltration into brain parenchyma [128].

Calcium signaling waves can be observed propagating within this type of networks [122, 128] and constitute a powerful readout to prove whether in a cell line intercellular communications do exist and, if it does, how efficient it can be. Using

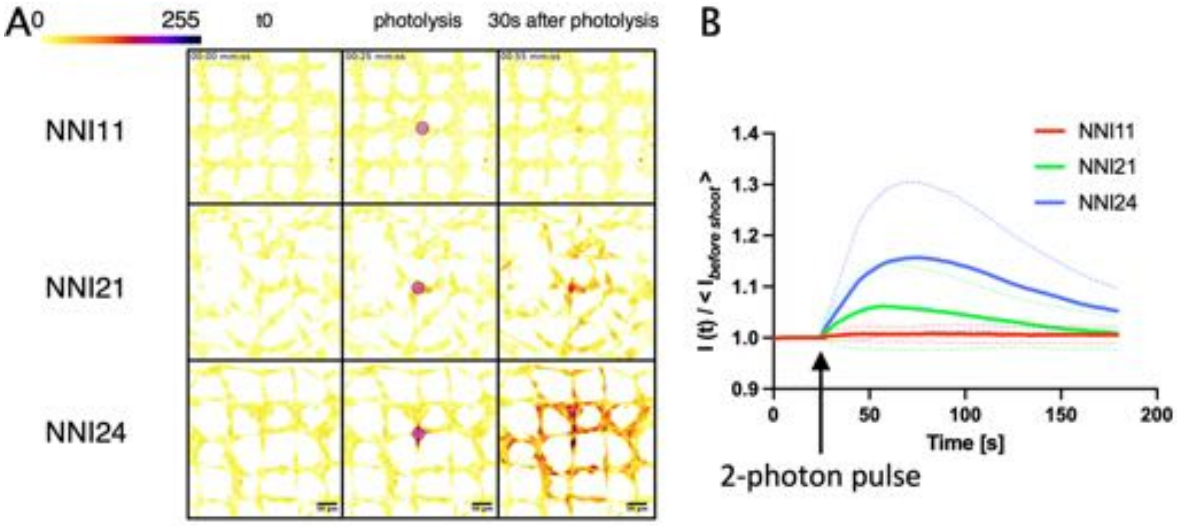

Figure 2.38: Intercellular communication and calcium waves propagation. (A) Snapshot of the cells before the 2-photon pulse (left), just after the pulse (250 ms long) that triggers photolysis (middle) and 30 s after the photolysis (right). The magenta circle corresponds to the point where the 2-photon pulse was induced. Color-bar corresponds to the intensity of the calcium signal. (B) Signal intensity of the calcium dye Rhod-2-AM overtime normalized over the mean intensity of all the pre-pulse frames.

our gridded micropattern, we indeed analyzed the ability of our NNI-21, NNI-24, NNI-11 patient-derived GBM cell lines to form this type of functional networks and gave preliminary hints on the molecular players involved.

We induced calcium waves through a 2-photon excitation system. Briefly, when cells reach confluency on the grid, the samples were loaded with the calcium dye Rhod-2-AM and the calcium chelator DMNP-EDTA. The former stained the calcium ion for fluorescent readout, the latter sequestered a fraction of the calcium present in the cell medium. When excited with a pulse from a 2-photon laser, the sequestered calcium is promptly released by photolysis, being the EDTA sensitive to ultraviolet wavelenghts. The localized, sudden spike in calcium concentration should propagate through the cell network depending on the presence of the cell-cell communication bridges: in this context, the grid system ensures a robust readout on how far calcium waves could potentially propagate.

With this assay, we have been able to record calcium waves within networks formed by our motile cells NNI-21 and NNI-24 while our non-motile NNI-11 were

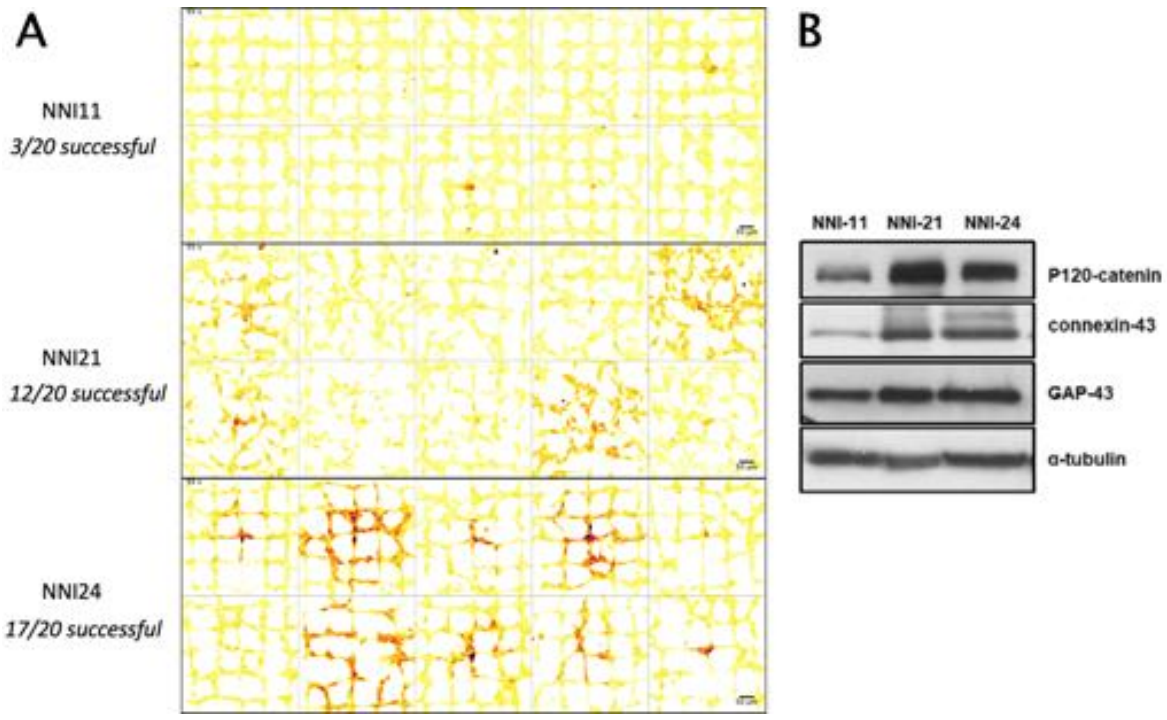

Figure 2.39: Intercellular communication and expression of related proteins. (A) 10 fields of view from an independent experiment are reported. The success rate is indicated on the left, pooling 2 independent experiments (10 fields of view per cell line per experiment). (B) Protein expression of the cell-cell adhesion markers p120-catenin, connexin-43 and GAP43 in total cell extracts from the NNI cells.

not able to transmit any signal (Fig. 2.38A, 2.39A). In addition to a correlation between the motile/non-motile phenotype and the presence/absence of propagating calcium waves, the paramount strength of how the waves propagate in the NNI-24 (Fig. 2.38B) is in close relationship with their higher collective migration (Fig. 2.17A). In accordance, molecules that have been involved in these networks such as connexin 43, Gap43 and P120-catenin were upregulated in NNI-21 and NNI-24 (Fig. 2.39B).

Chapter 3

Discussion

In heterogeneous tumors such as glioblastoma, some cells can be highly aggressive migrating long distances from the tumor core by following Scherer's structures, while other cells can be less motile and maybe more proliferative likely remaining in the tumor core. Our goal is to develop a method to rapidly define the various motility modes present in single patients and to identify which ones are the most efficient at invading mammalian brains. In previous studies, we and others, demonstrated that linear patterns were excellent proxy to mimic the brain blood vessel tracks, allowing high resolution imaging and analysis [180, 177, 183, 181, 91]. In particular, gridded micropatterns allowed to easily differentiate various motility modes [92]. Here, we improved our grid system by using spheroid spreading assays (SP2G for SPheroid SPreading on Grids, Fig. 2.11). Besides allowing a faster, semi-automated analysis of the cell migration by tracking the spreading area of the spheres, this assay allows the analysis of the cell motility on a naïve, clean substrate which has never seen a glioma cell, similarly to the surface of brain blood vessels before being invaded by glioblastoma.

3.1 Comparison of SP2G with other *in vitro* systems

We have developed SP2G as a comprehensive *in vitro* method for the holistic characterization of GBM migration and motility modes. In particular, SP2G relies on a gridded micropattern [92] that reproduce the tangled topography given by the Scherer's structures. *In vivo*, GBM exploits these structures as an invasive highway

[77]. Being no cells in the brain further than 25 µm from a capillary [100], the choice of 75 µm as grid edge is a good proxy to mimic the density of the vessel network (Fig. 2.1) [184]. Moreover, the topography imposed by the grid provides linear cues exploited by cells in *ex vivo* brain slice assays and, likewise, it induces the formation of invasive strands (Fig. 2.7) [105, 212]. Conversely, invasion is isotropic in 3D hydrogels devoid of topographical cues (Fig. 2.5) [148, 213]. Our gridded micropattern triggers motility modes that recapitulate the ones seen in 3D environments (Fig. 2.8) [210, 214]: strikingly, Doyle and collaborators [214] showed how mono-dimensional patterns triggers cell migration mechanisms similar to the ones adopted in three-dimensional configurations. Here, we propose a set of monodimensional patterns that form a network via several criss-crosses. Importantly, this setup keeps the advantages of simpler *in vitro* systems, such as experimental reproducibility, time profitability and amenability to high-resolution imaging techniques (Fig. 2.10). However, SP2G might be inadequate for co-cultures between GBM and other cell lines, whereas mechanical confinement or chemical perturbations can be easily applied. In the brain slice and 3D hydrogel assays, despite they recapitulate well the cues of the in vivo 3D environment, imaging can be troublesome because of opacity that, in turn, prevents the development of analytical tools.

3.2 Advantages introduced by SP2G analytical toolbox

In fact, SP2G combines the experimental section with an ImageJ/Fiji toolbox tailored on it. The toolbox relies on 7 macros that deliver 3 outputs for cell migration (area, diffusivity, boundary speed) and 3 outputs for the motility modes (collective migration, directional persistence, hurdling). The short duration of our experiments (8 hours) reasonably ensures the independence from cell proliferation. We utilized the patient-derived cell lines NNI-11, NNI-21 and NNI-24 as a benchmark to assess the performance of SP2G analytical toolbox (Fig. 2.14). In our previous work [92], we extensively studied the migration and the motility modes of these 3 cell lines. The NNI-11 were non-motile and highly proliferative, while the NNI-21 and NNI-24 were both diffusive, endowed with a stochastic, jumpy motion (*hurdlers*) and following the same track with high persistence (*gliders*), respectively. When tested with SP2G, the

motile NNI-21 and NNI-24 mirrored their known migration trend (90 and 60 µm/h for the NNI-21, SP2G and single cells on grid, respectively; 40 and 30 µm/h for the NNI-24) and, strikingly, SP2G enhanced their motility modes, confirming the high directional persistence of NNI-24 and hurdling of NNI-21. Furthermore, SP2G highlighted the formation of collective strands in the NNI-24, which is boosted as the spheroid acts as a reservoir for the cells to diffusively spread, a feature that we could not observe in our previous study [92].

3.3 Advantages introduced by utilizing spheroids

Indeed, for migration and invasion studies, spheroids are the *sine-qua-non* to dissect the motility modes behind the transition from a clustering niche towards a diffusive entity. Spheroids also allow to study 2D migration, 3D invasion, motility modes, the influence of biomaterials, microenvironmental cues, and drugs [137, 148, 173, 213]. Our results using a panel of cytoskeleton-perturbing drugs illustrate the suitability of SP2G as a sensitive drug screening platform (Fig. 2.18), unveiling dependency of SP2 on myosin II, microtubule, and f-actin for migration and motility modes. SP2 was independent from arp2/3, similarly to previous findings in glioblastoma [91]. This confirmed the suitability of SP2G as a motility platform to tackle glioblastoma invasion and showed its sensitivity, as differences at low dose of drugs were visible, particularly for microtubule perturbations (Fig. 2.19). These effects are usually hard to detect at low concentrations with other methods. Future experiments could investigate the effects of chemoterapeutic agents such as temozolomide.

The use of spheroids underlined other key aspects of GBM migration. For example, they keep a naïve microenvironment, useful to unveil the effects of external biochemical cues. In our case it revealed a striking dose-dependency on the laminin concentration of the gridded micropattern (Fig. 2.21): by modifying the density of laminin of the grid, we showed how SP2G fits in tackling micro-environmental cues like fine differences in the biochemical composition of the substrate. Interestingly, the migration velocity of PtK_1 cells on fibronectin substrates from 2.5 to 100 µg/ml peaked at 10 µg/ml, forming a gaussian-like trend [215]. When we tested the NNI-21 with SP2G, their migration monotonically increased up to the highest concentrations (200 and 400 µg/ml): whether this is due to an addiction of the NNI-21 to laminin or to flaws in microcontact printing (it is unclear how much protein is transferred

from the PDMS stamp to the substrate) is still unclear.

3.4 SP2G added value in studying glioblastoma heterogeneity

SP2G underlined other key aspects of GBM migration. For example, it revealed the hitch-hiking motility mode in one of our patient-derived samples. In fact, in our best example a GBM7 spheroid is torn apart into 3 daughter spheroids (Fig. 2.24), leading us to hypothesize the presence of hidden sub-populations within a heterogeneous tumor. In fact, spheroids maintain intra-heterogeneity and stemness of the native cancer while forming a clustering niche. On one hand, the presence of glioma stem cell niches endows the cancer with plasticity that relies on stemness and heterogeneity [45, 46, 53, 54], but on the other, recent avenues propose to leverage this GBM plasticity to induce an indolent differentiation state (i.e. lacking differentiation and tumor initiation capacity) potentially targetable with existing therapies [216].

Intra-heterogeneity in glioblastomas is deeply studied with genomic and transcriptomic tools [48, 49, 50, 51, 52]. However, how this heterogeneity is reflected in motility was poorly understood. Here we have reported how 11 sub-populations derived from 2 patient-derived samples behave differently in terms of migration, hurdling, persistence and collective migration (Fig. 2.26, 2.27, 2.31, 2.32). The sub-populations have different cell shapes, some aggregate spontaneously in islands or spheroids when cultured in 2D, others are prone to form several cell-to-cell interconnections (Fig. 2.23, 2.29). Furthermore, our transcriptomic analysis showed clustering of the motile versus non-motile groups (Fig. 2.33) and, while looking for enrichment in gene sets key pathways, ECM-receptor interaction and focal adhesion emerged (Fig. 2.34). We confirmed this result by qPCR (Fig. 2.36) and western blot (Fig. 2.37), showing a higher expression in the laminin binding integrins, in agreement with glioma preference for laminin and with the large presence of laminin on brain blood vessels [91, 92, 217, 86, 102]. Interestingly, we found a higher protein expression in the motile GBM7 sub-populations for the integrin Alpha 6 (Fig. 5e), which is known to regulate glioblastoma stem cells [217]. At this stage, we do not know whether the differences in sub-population motility and their combination

in the hitch-hiking mode might be present *in vivo*. Tracing the history of patients by correlating with *in vivo* data is likely to help on how heterogeneity and GBM diffusivity mutually drive GBM invasion in patients.

3.5 Discussion of preliminary results obtained in the study of glioblastoma functional networks

Another feature I co-studied utilizing the gridded micropattern is the formation of cellular networks in the glioblastoma cell lines NNI-11, NNI-21, NNI-24 (Fig. 2.38). Despite the setting is slightly different than SP2G (no spheroid is utilized), the principle is similar: the central point of the field of view is the starting point of a propagating calcium wave, which is triggered by an external a 2-photon pulse. Interestingly, the calcium wave strength (Fig. 2.38B) and the expression of key molecules involved in multicellular networks as connexin 43, Gap43 and P120-catenin (Fig. 2.39B) correlates with motility and collective migration values quantified by SP2G (Fig. 2.16,2.17). These results are in line with the milestone study by Osswald and collaborators in Winkler lab [122], where the increased expression of GAP43 is linked to higher tumor proliferation, area and volume in a *PDX* murine model. In the latest work from the same lab [218], Venkataramani and colleagues showed how heterogeneity is linked to brain invasion in the context of TM an functional network formation. Neural-like GBM cells who are disconnected from others drive GBM invasion and form neurogliomal synapses. This causes the *de novo* formation of TMs and increased cell's invasion speed. These results show how GBM invasion and heterogeneity are closely interlinked: with respect to this PhD work, it would be interesting to study how our sub-populations propagate calcium waves and form functional networks, and correlate these results with their capacity to drive GBM invasion. Assuming that the most-motile sub-populations drive the invasion of the others [218], it would be interesting to study whether the most motile cells are the more disconnected, and, when re-pooled with the less-motile sub-populations, investigate the way they cooperate.

3.6 Expanding SP2G towards a pan-cancer screening method

SP2G can be potentially expanded as a pan-cancer, motility screening device. Outside of glioblastoma, in which cells were studied with tapered grooves aiming to screen anti-motile drugs [181] or with electrospun fibers to attract the most-migratory cells in an implantable trap filled with citotoxic drugs [180], motility screening devices were developed for instance in breast cancer, ovarian cancer, and carcinoma [219, 220, 221, 222]. Together, these works revolve around the spontaneous migration characteristics of the selected cell pools in order to retrieve them for downstream analysis. For example, Chen et al. [220] developed a microfluidic chip to profile the chemotactic heterogeneity in the metastatic breast cancer cell line MDA-MB-231: the chemotactic cells were more migratory and sparsely growing. Similarly, the work of Yankaskas and collaborators exploits constrictions in a microfluidic device to predict the metastatic and proliferative properties of a panel of breast cancer cell lines [222]. Wang and collaborators utilized needles filled with Matrigel to retrieve carcinoma cells from primary mammary tumors in rats [219]. This approach was utilized to study gene expression in motile and non motile cells, showing that the genes involved in cell division, survival, and cell motility were upregulated in the migratory cells. Arora et al. developed 3D methods for sorting motile and non-motile cells [221]. One of them relies in peeling off the top layer of a 3D laminated device, assuming the migration of breast and ovarian cancer cell lines from the bottom substrate towards the top one, which is coated with fibronectin. All these methods allow molecular post-characterization of the sorted cell lines, while SP2G tracks and deeply describes the motility based on live cell imaging. The 2 approaches may be complementary, as these works do not permit to track cell motility and might be quicker for cell sorting. Conversely, for this PhD work, cells are sorted independently of the SP2G workflow, which is meant to screen the motility properties of any cell lines interacting with the gridded micropattern: this aspect is not considered in any of these works. In this sense, the versatility of our system will be proved with experiments involving a panel of cancer cell lines other than brain.

3.7 Limitations of this study

The last aspect worth discussing concerns the bottlenecks hidden in SP2G. They span aspects such as microfabrication, *in vivo* mimicry, and the lack of biochemical pathways that could be targeted with therapies.

Microcontact printing presents hidden flaws in the concentration that is actually stamped on the substrate. In this work, we coated the PDMS stamps at 50 µg/ml. However, as the stamp is leant onto the substrate to transfer the protein, we do not know how much of it transfers to the petri dish. This may depend on several variables, such as the material of the substrate (we stamped both glass and plastic), for how long the stamp is blown to dry the excess of laminin, and the pressure utilized to lean the stamp. This might have impacted the results when we fine-tuned the concentration of the laminin grid (Fig. 2.21). To rise awareness in the limitations of microcontact printing, we recently published a protocol where the step-by-step methods of this procedure are explained and the critical steps are highlighted [223]. To tackle the fine-tuning of laminin concentration, microcontact printing could be potentially replaced with deep UV patterning: briefly, a glass coverslip is coated with PEG-PLL (to prevent cell adhesion) that, by utilizing chromium masks, can be selectively burnt to obtain PEG-free zones [223]. The PEG-free zones - e.g. our grid micropattern - can then be coated with laminin solutions prepared at selected concentrations.

SP2G mimics only the topography of brain blood vessels, and the grid setup is a reductionist - yet decipherable - system to do so. As we print adhesive stripes, there is no curvature as in brain blood vessels. An interesting method to reproduce the 3D arrangement of blood vessels was published by the lab of Charlot in Bordeaux [184]. It relies on backside litography, which is useful to obtain geometries extruded from a substrate that imitated the vascular tree. Such geometries could be selectively coated with laminin and exploited for our migration studies. Furthermore, atomic force microscopy data from [162] suggested that a durotactic cue might attract glioma cells towards the brain blood vessels. This means that there is a gradient of stiffness from the parenchyma (the brain is a viscoelastic material with an average stiffness of 3 kPa [161]) to the vascular tree, which had a stiffness of circa 3 MPa [162]. In SP2G, the substrate stiffness is in the order of GPa (glass, plastic), and there is no stiffness gradient at all. Reproducing the physiological stiffness gradient *in vitro* might be

challenging, but the stiffness of brain blood vessels could be reproduced by patterning PA gels at values measured *in vivo*. Briefly, the combination of deep UV litography and PA gel fabrication returns patterned adhesive substrated on the PA gel [224] and this procedure could be exploited to get physiological stiffness values on a substrate for SP2G. Despite these approaches fail in tackling the creation of a vessel-to-brain-parenchyma interface, they might be useful for a more accurate physiological mimicry of the setup. To mimic the vessel-to-brain-parenchyma interface, the current SP2G setup or its potential extensions could be combined with the deposition of a hydrogel on top of the patterned surface. This approach was implemented by Gritsenko and collaborators in Friedl lab [173], where Matrigel was deposited on top of spheroids migrating on a substrate. Matrigel could be replaced with a more relevent HA gel [152].

In light of the discussed potential increments for SP2G, we do not know whether the *hitch-hiking* motility mnode identified in the GBM7 heterogeneous cell line would be reproduced in these setups. We do not even know if it might be present *in vivo*: interestingly, we hypothesized that this may be behind the dissemination of heterogeneous recurrent tumors. Reconstituting the heterogeneous bulk with fluorescent markers for each population and its stereotactic implant in mouse brains combined with *in vivo* imaging could give clues on this aspect. *In vitro*, the presence in SP2G of a solid biomaterial that three-dimensionally confined the cells might lead to different motility modes, and we do not even know whether cells would anymore stick to the printed pattern.

One of the main bottlenecks of SP2G is the lack of correlation between migration/motility modes and biological pathways wich could be potentially targeted with therapies. Through RNA sequencing analysis we identified upregulated pathways in the GBM7 motile sub-population compared to the non-motile ones. These motility-related pathways identified the upregulation of laminin-binding integrins (ITGA6, ITGA3), but we do not know whether this is reproducible (results are obtained from a single replicate, 1 sample per sub-population) and whether this is replicated as the substrate changes. In fact, we plated cells onto laminin before extracting the RNA, and this might constitute a bias. A different substrate (e.g. fibronectin, PLL) is very likely to change integrin expression accordingly. Furthermore, we do not know if laminin-binding integrins could be targets for therapies. Clinical trials for the chemotherapeutic agent cilengitide that targets the fibronectin-binding integrin

ITGAV showed no benefits in the group treated with Stupp protocol [73] plus cilengitide with respect to the group treated with Stupp protocol only [225]. This is in line with the enrichment of laminin around brain blood vessels that potentiate motility in GBM [101, 102, 103, 91, 92] and with our western blot in Figure 2.37. Despite integrins can be targeted for glioblastoma, we do not know whether our results could potentially unfold into clinical trials for drugs targeting laminin-binding integrins such as ITGA6 or ITGA3, and a successful drug development should be performed beforehand.

Finally, our experiments with drug treatments (Fig. 2.18) aimed at validating SP2G as a sensitive method for drug screening. These experiments did not help in identifying a relevant biochemical pathway that selectively hampered cell migration in GBM, neither relevant chemotherapeutic compounds were tested for cell motility. Future experiments could validate SP2G as drug-screening method for compounds to be tested in clinics.

In summary, we have presented a methodology that integrates the time-lapse imaging of spheroid spreading on grids with an ImageJ/Fiji analytical toolbox that quantitatively characterizes cell migration and motility modes. It is nicknamed SP2G, and we hope it opens up a new standard for motility screenings, potentially extendable as a pan-spheroid approach that helps answering questions on how cell migration impacts on cancer dissemination.

3.8 Debatable: is science running out of (original) ideas?

The final section of this PhD thesis is a stand-alone essay that lies outside its main technical and scientific body concerning Glioblastoma. It includes a series of (personal?) considerations regarding the socio-economic status of science, which would otherwise be lost in the meanders of my Google Chrome history and purposelessly floating in my weak memory. This can be the chance to put them black on white and trying to share them with my 2 or 3 readers.

The main article fueling these reflections is from the journalist Derek Thompson [226], staff writer at *The Atlantic* who, basing on a paper about stagnation and scientific incentives [227] by Jay Bhattacharya and Mikko Packalen - medicine and economics professors at Stanford and Waterloo university, respectively - made me jump into the question: nowadays, what is the approach adopted by scientists to drive scientific innovation? This debate might provocatively sustain that scientists are running on fumes, just passively *"standing on the shoulders of giants"*. However, this discussion needs to dig into economic, social and, of course, scientific considerations. Initially, this piece of writing explores whether new ideas are actually harder to find and how scientific works are rewarded. Then the discussion digs on how the global markets have changed and adapted to make people comfortable in welcoming novelties, how the scientific market has been laid out by institutions and how scientists are mastering it, and its implication on the way this system is feeding economic growth through scientific discoveries. Well, it may seem a bunch of ideas thrown here and there, but I'll try to smoothly walk my readers through them.

Let's start with a catchy paradigm: in cinema, the movie industry is producing less and less original blockbuster movies. Since 2018, when I started my PhD, the number of sequels and remakes based on pre-existing cinematic material occupies the largest portion of releases. Considering the top-10 grossing movies worldwide of each year, in the years 2018-2021 28 movies out of 40 were either re-makes or sequels (Tab. 3.1). Fast-backward 25 years in time: between 1993 and 1996, 8 movies out of 40 were either re-makes or sequels (Tab. 3.2). One may argue that many

of these releases were either based on older cartoons/tv-series or books, which are not as viral as cinema in shaping the culture, the identity of masses (cinema was invented to educate and spread propaganda!). Indeed, *Toy Story*, *The Lion King*, or *Pocahontas* influenced the childhood of Millennials and *Forrest Gump* and *Jurassic Park* became cultural milestones: people were keen on cinemas to see characters that never appeared on the big screen. No doubts as well that *Avengers*, *Spider-Man* and *No Time to Die* have been planetary successes, which are all coming from decade-long franchises: nowadays, people are keen on cinema but absorbed with familiarity. How does this example relate to science?

"New ideas no longer fuel economic growth the way they once did", is the blunt point by the economists Bhattacharya and Packalen in the abstract of their publication [227]. Despite we might seem on the cusp of a new scientific revolution, with CRISPR enabling selective molecular treatments and telescopes able to reconstruct the shape of a black hole, global economy might conversely be on the cusp of a recession, or at least stagnating. *"A popular explanation for stagnation is that good ideas are harder to find, rendering slowdown inevitable"*. There are roughly 25 years of literature on the relationship between economic and intellectual stagnation: even the idea that science is running out of ideas is not a new idea. Even this section of my discussion is not a new idea. Is this true?

The main issue in the scientific system is the lack of rewards for ideas that can potentially transform into landmark advances. No rewards are awarded for novel, exploratory works, regardless their scientific impact and how popular they become. Scientists then respond as everyone else would, that is following the path that brings rewards: ideas are basing on works previously praised by the community, conceived for being easily-accepted and, being science a peer-reviewed system, for appealing reviewers and journal editors. Consequently, the disincentive towards exploratory works has shifted the evaluation of scientists according to their popularity. The more a scientist is able to generate publications that are in turn cited by other scientists, the more it is considered influential (the so-called *h-index*). The same applies to their papers for becoming breakthroughs. The *citation revolution* has, on the other hand, incentivized mee-too incremental science over exploration and scientific play. This circle is finally reinforced by academic search engines such as Google Scholar, which allows scientists to survive the harsh "publish-or-perish" law, but its ultimate by-product is stagnating science. On the other side of the publishing

	2021	2020
Rank	**Release**	
1	Spider-Man: No Way Home	The Eight Hundred
2	The Battle at Lake Changjin	Demon Slayer the Movie: Mugen Train
3	Hi, Mom	Bad Boys for Life
4	No Time to Die	My People, My Homeland
5	F9: The Fast Saga	Tenet
6	Detective Chinatown 3	Sonic the Hedgehog
7	Venom: Let There Be Carnage	Dolittle
8	Godzilla vs. Kong	Legend of Deification
9	Shang-Chi and the Legend of the Ten Rings	A Little Red Flower
10	Sing 2	The Croods: A New Age

	2019	2018
Rank	**Release**	
1	Avengers: Endgame	Avengers: Infinity War
2	The Lion King	Black Panther
3	Frozen II	Jurassic World: Fallen Kingdom
4	Spider-Man: Far from Home	Incredibles 2
5	Captain Marvel	Aquaman
6	Joker	Bohemian Rhapsody
7	Star Wars: Episode IX - The Rise of Skywalker	Venom
8	Toy Story 4	Mission: Impossible - Fallout
9	Aladdin	Deadpool 2
10	Jumanji: The Next Level	Fantastic Beasts: The Crimes of Grindelwald

Table 3.1: Summary of top 10 highest-grossing movies during the years 2018-2021. Red color highlights movies that are re-makes or sequels. Source: https://www.boxofficemojo.com/year/world/.

industry, journal editors look for works that might generate a high number of citation, being the main metrics for evaluating a journal, the *impact factor*, function of the number of published papers and the citation gathered with such papers. Celebrating breakthrough discoveries with a high number of citations is right, but evaluations with monodimensional metrics relying on mere raw counts generate a distorted view

	1996	1995
Rank	**Release**	
1	Independence Day	Toy Story
2	Twister	Apollo 13
3	The Heat	Batman Forever
4	Mission: Impossible	Pocahontas
5	Jerry Maguire	Ace Ventura: When Nature Calls
6	Ransom	GoldenEye
7	101 Dalmatians	Jumanji
8	The Rock	Casper
9	The Nutty Professor	Se7en
10	The Birdcage	Die Hard with a Vengeance
	1994	**1993**
Rank	**Release**	
1	The Lion King	Jurassic Park
2	Forrest Gump	Mrs. Doubtfire
3	True Lies	The Fugitive
4	The Santa Clause	The Firm
5	The Flintstones	Sleepless in Seattle
6	Dumb and Dumber	Indecent Proposal
7	Clear and Present Danger	In the Line of Fire
8	Speed	The Pelican Brief
9	The Mask	Schindler's List
10	Pulp Fiction	Cliffhanger

Table 3.2: Summary of top 10 highest-grossing movies during the years 1993-1996. Red color highlights movies that are re-makes or sequels. Source: https://www.boxofficemojo.com/year/world/.

of science [228], being such metrics incapable of distinguishing between incremental, me-too science and scientific exploration and play.

Would Brock and Freeze have nowadays gone to Yellowstone Park to isolate the bacterium *Thermus aquaticus*? In 1969, their work [229] about the heat-resistant bacterium - harvested from waters hotter than 70 °C - gained few citations. Temporal leap to 1976: the enzyme DNA polymerase was isolated by other scientists and the discovery published [230]. Both of these works initially generated a modest impact in the scientific community. Until the mid 80s, when Kary Mullis was

dreaming of the PCR: its successful invention involved several cycles of heating and cooling the sample to amplify a DNA strand through the effect of DNA polymerase [31]. Due to its thermosensitivity, the DNA polymerase was manually added back in each cycle, rendering the procedure extremely time-consuming and thus impractical for widespread use. After few years, Mullis refined the PCR protocol by discovering the work by Brock and Freeze, which apparently had nothing to do with his. The thermostable DNA polymerase of the *Thermus aquaticus* was hence isolated and the PCR procedure fully automatized [231]. If today we are able to sequence zillions of DNA/RNA strands and to process millions of COVID-19 tests is thanks to both the explorative, playing around science of couple of scientists in the geysers of Yellowstone Park, and the incremental science on a promising topic that has ultimately revolutionized biochemistry. Either the scientific approaches are needed for 2 reasons: firstly, breakthroughs rely on high-risk works. Secondly, it is excessively difficult to anticipate which field will become a breakthrough with slow, gradual advancements. However, high-risk, explorative science needs rewards in order not to disappear.

Figure 3.1 is the first brick to understand how. It illustrates the lifetime of a scientific idea in 3 phases. New ideas come to scientists as they carry out their work: those in the embryonic form bring no evidence and the majority just dies out, while others pave the way for the exploration phase, in which many scientist might be involved. In this phase there is a huge effort and little reward, as it implies several negative experiments going under the carpet and few positive outcomes. Once the results can be arranged in a publication, either it just makes the giant's shoulder stronger (in this case the authors gain a huge knowledge, but generate a low scientific impact), or it is transformed in a fruitful line of experiments and applications. It then goes in the breakthrough phase, spinning-off scientific career(s). As it has convinced the skepticism of the community, various other scientists apply the idea in their own field: this is modeled by a sharp increase in the curve, as the scientific impact is larger and larger with a smaller effort, and these scientists will begin standing on the shoulders of giants. Ultimately, in the incremental advance phase, there is work to sharpen the details and have an high impact, despite a large effort. What the citation system rewards is those who jump on the idea and have the capability to exploit it in the breakthrough/incremental advance phase, generating works that physiologically cite only the latest papers: as a very early idea thoroughly permeates scientific knowledge, what it is actually founding is implicitly taken for granted.

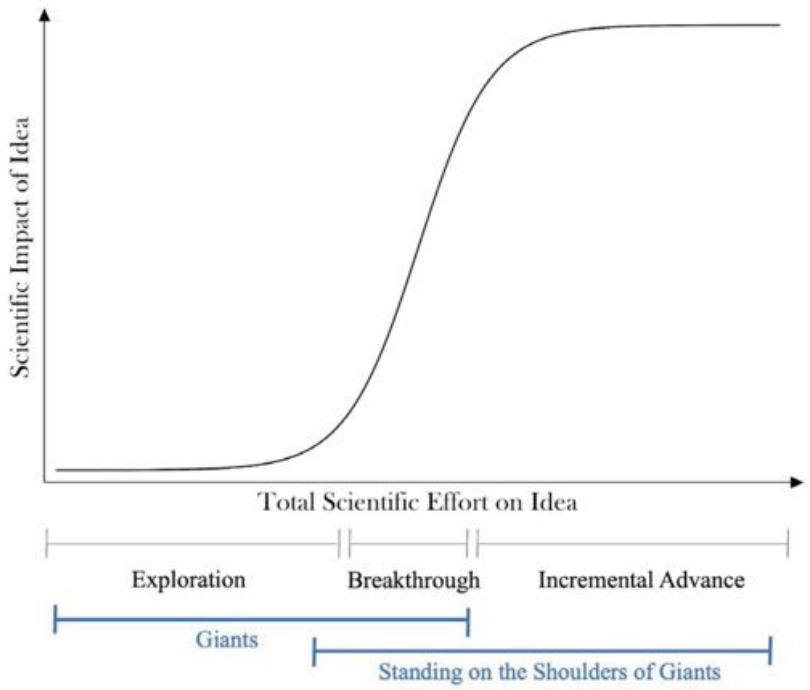

Figure 3.1: The relationship between scientific effort on an idea and the scientific impact of the idea. In this model, the horizontal axis captures the three phases of scientific idea lifetime: exploration, breakthrough, and incremental advance. The vertical axis captures the influence of the idea on the scientific community. Work done during the exploration phase has little observed impact but lays the necessary groundwork for the later breakthroughs.
Furthermore, giants are not only those who work on the idea during the breakthrough phase but also those who investigated and developed the idea during the exploration phase. Importantly, the status of giant does not depend on whether the idea is ultimately successful. Adapted from [227].

This is mirrored in the citation system, that indeed forgets the earliest works that actually have brought the novelty and favors the latest ones, thus fostering scientific stagnation [232]. For instance, in glioblastoma, the seminal works by Virchow [5, 6] and Scherer [24, 2] gained much less citations than single-cell sequencing papers within the TCGA project [45, 46].

The strategies adopted by funding agencies generate a positive feedback loop over this cycle. As leading nation in biomedical research, the USA - through the quantitative National Institute of Health (NIH) - established a system that was mirrored in the EU - through the European Research Council (ERC) - that is prone to give fundings to highly-cited scientists publishing the large number of papers, failing to evaluate innovativeness in research proposals. The richest grants are hence

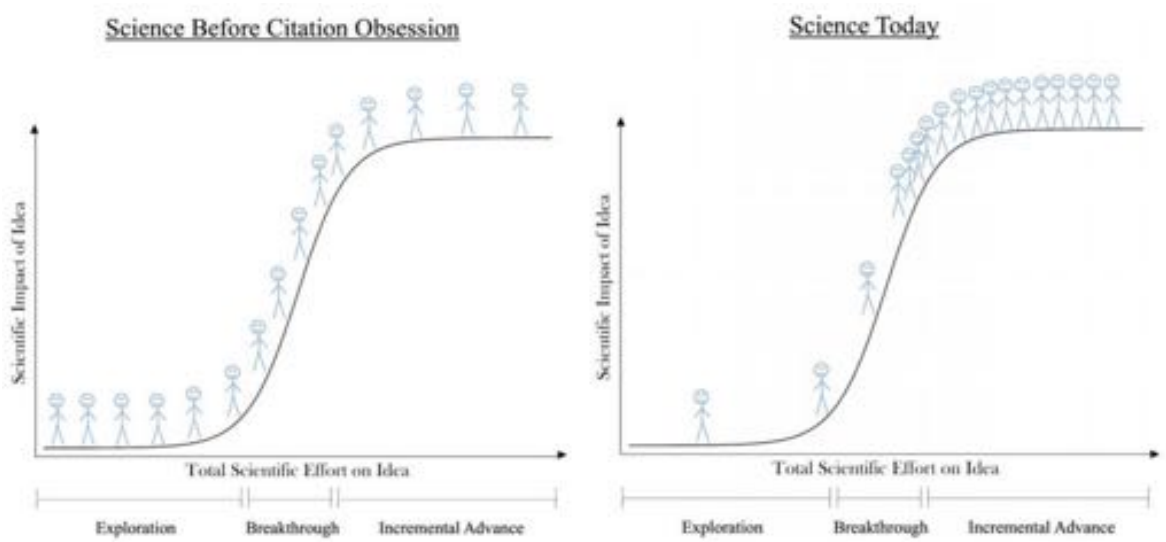

Figure 3.2: The shift in scientists' effort away from exploration and toward incremental science. Before citations came to dominate research evaluation, more scientists were willing to engage in risky exploration that laid the groundwork for later breakthroughs (left panel). The citation revolution led to a decline in exploration in favor of incremental science. The decline in exploration eventually also decreased opportunities for breakthrough science (right panel). Adapted from [227].

awarded to those who propose ideas that stand on giants' shoulders, suffocating novelty and creativity [233]. Here's why scientists are less confident in taking the ownership of risky projects and to propose ideas that rely on more or less familiar foundations (Fig. 3.2).

Given that scientists, like all the people, respond to incentives, the constructive way to untangle the stagnation is to provide rewards for explorative, novel works. Providing such type of rewards implies that novelty has to be measured. To provide metrics for novelty, Bhattacharya and Packalen propose the textual analysis of research publications, basing on the idea that the text of a scientific work builds new ideas manifested as new words and new word sequences. This reminds me of the work by Ludwig Wittgenstein, who deeply investigated the relationship between language and reality. His early-20$^{\text{th}}$-century work emerged in a season where philosophers and thinkers were rebuilding the foundations of scientific knowledge, firmly believing in the paradigmatic, exemplary validity of science for all the knowledge that aims to be truthful and rigorous. Long story short: Wittgenstein assumed that scientific knowledge is configured through a set of linguistic sentences. The gnosiological (i.e. regarding the theory of knowledge: gnosiology aims to provide a definition

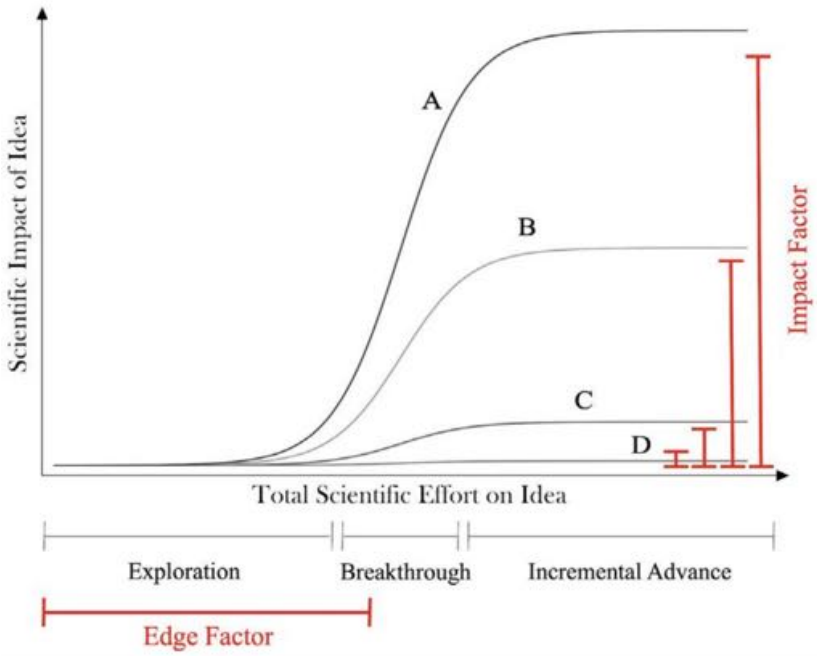

Figure 3.3: The impact factor and the edge factor for four ideas. The impact factor (citation counts at journal-, scientist-, or article-level) rewards only high-impact work on ideas that succeed. The edge factor rewards early exploratory work on successful ideas (A and B) and on ideas that ultimately fail (C and D). Increasing the tolerance for failure is one key rationale for measuring and rewarding scientific novelty separately from scientific impact. Adapted from [227].

for knowledge) analysis of reality is the analysis of knowledge intended as language: reality *per se* is what factually happens and what can be expressed as language, and the two are isomorphic. Furthermore, he believed that both language and reality are assembled combinations that can be reduced to atomic determinations that are, in turn, the foundation of a truthful and rigorous knowledge. In light of these premises, the textual analysis of research papers through indexing and classification can determine the vintage of the ideas within each publication. Novel versus conventional sciences can thus be discriminated. The calculation of *edge factors* for scientists and journals is similar to *impact factors*: the former recapitulates the tendency to pursue and publish novel ideas, the latter to build a sound science (Fig. 3.3). Let's consider the 4 ideas in Figure 3.3: the 2 more-successful (A and B), despite being much more impacting than the others, are rewarded as much as the 2 less-successful (C and D) with an *edge factor* metrics. This could favour explorative science and increase the tolerance for failure, making scientists more prone to explore several paths and embarking the one that in the end looks more promising. In this model, novelty

and impact are empirically different since, firstly, science that is built on solid ideas does not always lead to influencing contributions: this underlines the importance of incremental science, which has nothing to do with bad science. The bad thing is having too much of it. Secondly, novel research often leads to failure rather than success: only a small slice of the successes become breakthroughs.

The considerations by Bhattacharya and Packalen conclude by providing a proof-of-concept model of the *edge factor* based on the existing literature. Its calculation, however, is not clearly reported. The idea is to have software capable to analyze text in a *Wittgensteinian* manner: in the Artificial Intelligence (AI) field we have works that lay solid basis to this regard. Not later than summer 2022 it went viral on the news that Blake Lemoine, AI engineer at Google, believed that the AI Language Models for Dialog Applications (LaMDA) [234] was sentient [235]. Google and most of the press reported it is not. Few people might think it is. I am linking the suggestion by Bhattacharya and Packalen with the huge capabilities that AIs such as LaMDA has shown to have: to get an idea how far this AI has come in dialoguing with humans, I invite those who have a scarce half an hour to read/listen at the transcript of a conversation between Lemoine and LaMDA (link: https://cajundiscordian.medium.com/is-lamda-sentient-an-interview-ea64d916d917). In the conversation, they talk about emotion, feelings, death and... self-awareness. For those who do not have half an hour, just think on how powerful the Google answer box is: in fraction of seconds Google AIs browse the web, associate the user's question with the most pertinent answer, links it in a dialog box, and redirect to the very exact line of the source text. Would it be a dream to create *Language Models for Novelty Applications* - LaMNA - that are trained with texts from scientific papers and capable of providing novelty scores in the form of *edge factors*?

So far, the main subject of this section has been the discussion of scientific approach adopted by scientist to drive scientific innovation. Derek Thompson, in his article, stretches the discussion to other fields, which I think are worth mentioning. Are new ideas actually incapable of nurturing growth as in the past? Or is there a short-circuit somewhere else in the western socio-economic system?

In institutions, Europe is not creating elite universities since centuries, in the USA the top-ranked schools are roughly 100-150 years old. I mentioned the NIH, founded in the 19th century, and in Italy, since 1965, we have Fondazione AIRC per la Ricerca sul Cancro (AIRC) as one of the main agencies funding cancer research. Despite the ERC was established in 2007, rumors to build institutions that deal with 21st-century issues (e.g. the pandemic) or today's economic trends are far from being heard. In science and technology, a famous paper in the *American Economic Review* states that *"everywhere we look we find that ideas, and the exponential growth they imply, are getting harder to find"* [236]. The authors examines how productivity, since 1970, has dramatically decreased - e.g. 18 times to keep the pace of the famous Moore's law - in electronics, agriculture, biomedical sciences, and publicly-traded firms: the higher number of researchers does not necessarily generate new technological advancements or, the other way around, we need greater and greater efforts to keep a constant growth.

Let's imagine to be in 1780, going to sleep, and waking up in 1830: probably we would be amazed by technological advancements from the first industrial revolution. Cities would now be urbanized, open fields disappeared, burgoise rising and industries booming in the cotton, textile, mining, hydraulics, metallurgic fields. Goods were transported with the first steamboats and trains. In physics, we would be in the golden age of electromagnetism: scientists as Coulomb, Ampere, Ohm, Faraday were laying the basis of the discoveries of the early 20th century. Same process, 100 years later: cities were electrified and skyscrapers sprouting in the USA, a flooding immigration towards America was promoting entrepreneurship and the current top-world university were being founded. People could move by car and plane, listen to radio and telephone communication, take pictures and go to watch soccer games at the stadium or movies at the cinema. Thanks to anesthesia, the first attempts in curing glioblastoma were possible through craniotomies. In physics, Einstein would have postulated special and general relativity from the theories in electromagnetism. Across the 21st century, the main invention is the widespread use of the internet, that spinned-off a set of incremental advances over the telephone that permit instant communication and access to almost any service. If we were to wake up today after 50 years we would find barcodes, GPS and informatics to track what we buy, where we are, what we did. As we approach 2030, cities have roughly the same aspect, we did not build hyperloop trains, flying cars, or assistant robots obeying the Asimov's

laws; neither urbanized cities to make them climatically sustainable, unified quantum mechanics and general relativity or proved the string theory. How come we did not realize the *revolutionizing* fancy dreams of the 1980s?

I do not believe and I do not want to believe that today's scientists are running out of ideas. There is plenty of brilliant people in the research institutes I have been. Nor screenplay writers are innately unable to conceive original stories for their movies. Where's the fault then? It is hard to find an all-encompassing reason, but some bricks might help in explaining how this complex phenomenon is standing.

First brick. *Data dulling* made cultural investments more statistically intelligent and tended to ruin originality. When the application of inferential statistics revolutionized baseball in the early 2000s - a.k.a. moneyball, the same models were applied for decision making in culture and arts. For filmmakers, this corresponded in pouring money in projects that were more likely to generate economic returns. Sneakily innovative swirls on familiar stories turned out to be the most appealing blend for moviegoers. Music producers, as these algorithms became capable of anticipating the audience tastes, realized that the largest chunk of people likes to listen the same thing over and over. Due to the Shazam effect, songs are spending more time in the ranking charts and radio stations are more repetitive. As producers became expert in mastering markets, scientists did as well. Principal Investigators know what journal editors and their community most probably like and dislike. They know which proposals are more likely to be funded, and they know that proposals have to like as many peer-reviewers as possible [237]. Successful applications are most achievable by showcasing a deeper expertise - typical of older scientists - rather then cross-disciplinarity. This trend in the scientific market is exacerbated by the time spent by scientists in asking for money and navigating the bureaucracy of science: 30 to 40 % [238]. Despite the peer-review system is virtuous in prioritizing applications, it shows also the flaws of the scientific market [239, 240].

Second Brick. In 2020, the venture capitalist Marc Andreessen published a famous article entitled *IT'S TIME TO BUILD* [241]. While deciphering the total failure in responding to the coronavirus pandemic by modern democracies [242], he pinpointed the escalating *"smug complacency"* of the western world as leading to stagnation in city development, public health, education, transportation, which all still rely on what was built in the past. He urged more entrepreneurship in all of these sectors. Assuming that money - all the western states passed billion, or trillion coronavirus

rescue packages - and capitalism - *"capitalism is how we take care of people we don't know"* - are not causing the stagnation, he is envisioning an attitudinal revolution in all of us: we need to desire to build what we actually need. Ezra Klein, columnist at the New York Times, faced the discussion opened by Andreessen [243]: the lack of building does not necessarily mean lack of desire - governments are indeed loaded with proposals in the aforementioned sectors. What is missing is an efficient institutional apparatus to make the proposals approved. They just don't pass because western democracies have become *dysfunctional vetocracies*: everywhere, power is too-widely distributed. As somebody wants to build, many people with vetoes impede that building to happen. The result is a system based towards inaction and incrementalism, rather than action and ambition. What has to be rebuild is the institutions. I think truth may lie in the middle: in 2018, the *"smug complacency"* towards the *res publica* caused the collapse of the "Morandi Bridge" in Genoa. After the catastrophe, governmental institutions strove to quickly build a new bridge. Desire and permissions ran hand by hand. Nobody thought of veto. The result? A new bridge was built in less than 2 years and... all the crucial bridges/viaducts have been thoroughly checked all over Italy.

Third brick. We are living in an age of *gerontocracy*, which is quite likely linked to the bias towards inaction and incrementalism. In institutions, considering the last 4 elections of the italian head of state, the youngest elected president was the 74 years-old Sergio Mattarella in 2015. Joe Biden is the oldest President in US history. In business and cinema, the average age of CEOs of S&P 500 companies increased of more than 10 years over the last two decades, as well as the age of leading actors in movies. In sport, the teams where LeBron James and Cristiano Ronaldo (both 37) play are willing to offer them net salaries worth more than 30 M€. In science, Nobel prize laureates and NIH grant awardees of are getting older [244]. As James Watson and Albert Einstein were 25 and 26 when they published about the structure of DNA and special relativity, correlating gerontocracy with the increased life expectancy is reductive. Part of the explanation lies in the concept of *"Burden of Knowledge"* [245]: it is becoming more complicated to learn something about the world because nowadays we know a lot about the world. For youngsters, mastering the existing knowledge to push its frontiers outwards has become burdening. No disrespect for Gregor Mendel, but cross-breading strains of peas in the backyard - agriculture was there since millennia! - and showing the results in an observational study it's

surely not a thing belonging to 21st century. Today's experiments require notions that academics typically gain over master, doctoral, and post-doctoral trainings that may span over a decade. Today's experiments require dedicated facilities. Today's experiments, in biology, involve material - cells - that are literally ecosystems made of thousands of variable that interact with thousands of variables in their outside. Drawing hypothesis, designing, carrying out and interpreting experiments has become burdening compared to the past. Side effects? The aging of science. Another part of the explanation is on how work and workplaces has evolved: the Boomer elite is clinging to the power and to the high positions gained decades ago. Due to the *"Boomer Blockade"*, Gen Xers and Gen Yers are hence delayed or struggling to get to the highest ranks [246, 247]. The rising *"Workism"*, the idea that work has become the personal religion in an era of plunging religiosity, generated this blockade and became the dominant mindset at the workplace. It has good sides - the shift towards more brainy labors - and bad sides - workplaces are becoming religious temples leading to spiritual emptiness. Contributions from the wise expertise of old people must not be cast aside, but innovations, and above all revolutions, need a naïve transversal plasticity that is more inherently common in young people.

Fourth brick. To this regard, we might have to accept that we are living in an age of *normal science*, intended according to the consideration of the philosopher Thomas Kuhn. He tried to answer the question: how are theories criticized and formulated? He realized that the mere examination of the logical structure of theories is not sufficient. It is necessary an historical approach on how and why they raised and, when applicable, how and why they were abandoned. He crossed the epistemology with the history of science: in his view, science is not growing through a linear accumulation, but following *"periodic revolutions"* (i.e. *"paradigm shifts"*). These revolutions definitively take over as *"anomalies"* are progressively seeded and proven right within the previous paradigm (in which *"normal science"* is conducted) [248]. In a *Kuhnian* sense, scientific proofs about young-scientist driven advances come from the paper *"Does science advance one funeral at a time?"* [249]. According to this analysis, the premature death of a luminary opens up opportunities for the opponents to grow the field and drive innovation, while the flow of publications by the collaborators decreases. *"A new scientific truth does not triumph by convincing its opponents and making them see the light, but rather because its opponents eventually die, and a new generation grows up that is familiar with it"* (Max Planck) [250, 251].

An example in a relatively small field: in the debate between *Reticularists* and *Neuronists* (see section 1.1.1), I let my 2 or 3 readers guess who died first between Camillo Golgi and Santiago Ramón y Cajal...

What can be the best way to untangle all these considerations? What do we actually need to build? I agree with Ezra Klein in stating that we need to build institutions striving for ambition and pragmatism [243]. Rather than changing old institutions conceived to manage 20th century issues, a new institutional course should engage with arising businesses and nimbly reshape as changes occur. On the other hand, businesses cannot elude the existence of institutions and governments, they have to cope with them so as to synergistically rebuild the political power. Surely this is a process that has to initiate from the roots: it is an educational challenge that has to start in primary schools. The new generations should be educated as men, not only as workers.

Fast Grants (https://fastgrants.org/) may give lessons on how to plan the future of science. The assumption of this institution conceived to speed up COVID-19 research is that, in the world, several projects are blocked on

"[...] the willingness of funders (especially institutional funders) to support something unusual simply on the basis of belief in the individuals involved. Too often, the de facto goal of funders is to find established things that look like everything else - it is typically easier to defend a long-established institution. But, of course, the most valuable opportunities will often be those that look quite different, and a structural bias towards familiarity can easily militate against innovation" [252].

Fast Grants supported short-term projects with application forms that could be compiled in 30 min, and response on funding decision in less than 48 hours. Since the large vaccine programs were not funded by Fast Grants, probably the fight against the pandemic would not have unraveled differently. This reveal the strength of the current scientific market. However, Fast Grants revealed also its weaknesses: it financed stuff like saliva tests, clinical trial, long-COVID research, with relatively easy money that implicitly tolerated failure. Outcomes? Fast Grants was acknowledged

in more than 350 papers. In surveys proposed to the applicants, more than half of them pointed how they spend 1/4 of their time in research application and, most importantly, circa the 80% would change their research focus *"a lot"* if they were given the possibility to, and they would become more ambitious if the current scientific funding body had an higher tolerance for failure. In conclusion, Fast Grants reveal how science can be quick if the scientific marked would be different or, at least, more diversified: alternative scientific funding methods can work. As the Scientific Revolution pointed out the importance of the scientific method, we need a thorough analysis of the social practices in the scientific market [226, 253, 254]. In other words, we need more *science of science* that builds a new scientific market that, in turn, drives innovation and paves the way towards a new scientific revolution.

Chapter 4

Materials and Methods

4.1 FMN1 shRNA design and cloning

shRNAs against human FMN1 were designed to target 19 nucleotide sequences and cloned into the BamH1 and HindIII cloning site of pRNAT-U6/Neo vector (GenScript corporation) which also contains a GFP marker under a cytomegalovirus promoter control. PAGE purified oligos (FMN1-KD#1 forward, 5'-GATCCC GTA TTA CGA GAC ATC CAA ATT CAA GAG ATT TGG ATG TCT CGT AAT ACT TTT TTC CAA A-3' and reverse, 5'- AGC TTT TGG AAA AAA GTA TTA CGA GAC ATC CAA ATC TCT TGA ATT TGG ATG TCT CGT AAT ACG G -3'; FMN1-KD#2 forward, 5'- GAT CCC GGA GTC GCT AAG AGC TGT GTT CAA GAG ACA CAG CTC TTA GCG ACT CCT TTT TTC CAA A-3' and reverse, 5'-AGC TTT TGG AAA AAA GGA GTC GCT AAG AGC TGT GTC TCT TGA ACA CAG CTC TTA GCG ACT CCG G-3'; FMN1-KD#3 forward, 5'- GAT CCC GAC AAC CAG AAG TAA TCA ATT CAA GAG ATT GAT TAC TTC TGG TTG TCT TTT TTC CAA A-3' and reverse, 5'- AGC TTT TGG AAA AAA GAC AAC CAG AAG TAA TCA ATC TCT TGA ATT GAT TAC TTC TGG TTG TCG G-3') were obtained from Integrated DNA Technologies. 0.5 nmol of forward and reverse oligonucleotides were diluted to 20 ml in water incubated for 4 min at 94 °C and slowly cooled down to 4 °C. Annealed oligos were ligated into the BamH1 and HindIII restriction sites of pRNAT-U6/Neo vector. Successful cloning was confirmed by sequencing.

4.2 Cell culture

Rat C6 cells were cultivated in high-glucose DMEM supplemented with glutamine and 10% fetal bovine serum (FBS). To form spheroids, C6 cells were seeded in untreated 6-cm petri dishes previously treated for 1h with 0.2% pluronic F127 in DPBS at room temperature. After 1 day, spheroids between 75 and 150 µm in diameter were obtained. Patient-derived GBM samples from the National Neuroscience Institute (NNI-11, NNI-21 and NNI-24) were acquired with informed consent and de-identified in accordance with the SingHealth Centralised Institutional Review Board A. Patient-derived GBM samples (GBM-7, GBM-22) from the laboratory of G. Pelicci (IEO, Milan, Italy) were acquired according to protocols approved by the Institute Ethical Committee for animal use and in accordance with the Italian laws (D.L.vo 116/92 and following additions), which enforce EU 86/609 Directive (Council Directive 86/609/EEC of 24 November 1986 on the approximation of laws, regulations and administrative provisions of the Member States regarding the protection of animals used for experimental and other scientific purposes). Our patient-derived GBM cell lines were kept as previously reported [223]. Briefly, GBM cell lines were grown in non-adherent conditions utilizing DMEM/F-12 supplemented with sodium pyruvate, non-essential amino acid, glutamine, penicillin/streptomycin, B27 supplement, bFGF (20 ng/ml), EGF (20 ng/ml), and heparin (5 mg/ml). Patient-derived GBM cell lines were passaged every 5 days. All the cell lines were maintained at 37 °C and 5% CO_2.

4.3 Cell Transfection

For transfection and migration assays, NNI-21 were cultured as monolayers on laminin (10 mg/ml) coated petri dishes for 3-5 days before transfection. Cell transfections were performed with a Neon electroporator (Invitrogen) as per manufacturer's recommendations as follow: 10 mg DNA for 1,000,000 cells were electroporated at 1600V, 20 ms, 1 choc in 100 ul buffer R. For grid migration, matrigel and animal experiments, NNI-21 were transfected with control and FMN1 shRNAs and single clones were selected in geneticin (50 mg/ml).

4.4 Brain slice invasion assays and staining

Mouse brains from C57BL/6J mice (http://www.criver.com; Charles River, Wilmington, MA) were isolated in the animal facility of IFOM, in accordance with the Institutional Animal Care and Use Committee, and in compliance with the guidelines established in the Principles of Laboratory Animal Care (directive 86/609/EEC); they were also approved by the Italian Ministry of Health. The brain slice assay was performed as reported in [255] and [209]. Prior to sacrifice, mice were anesthetized, their chest was cut and intra-cardiac injection was performed with 5 ml solution of Dil stain (ThermoFisher D282) to label the luminal side of blood vessels. The Dil stain was diluted 0.5 mg/ml in 100% ethanol and this solution was further diluted 1:10 in a 30% w/v solution of sucrose-DPBS. Brains were then isolated in ice-cold $CaCl_2$+/$MgCl_2$+ 1X HBSS (Euroclone ECB4006) supplemented with 2.5mM HEPES (complete HBSS). Brains were sectioned in 150 or 100 µm thick slices using a Leica VT1200S vibratome and placed in a glass bottom 24-well, which was previously coated at 37 °C overnight using a solution of 12.5 mg/ml laminin and 12.5 mg/ml Poly-L-lysine (1 slice/well). Slices were left 3h at 37 °C and 5% CO_2 to consolidate on the substrate. Subsequently, glioma spheroids were gently added and the co-culture was kept 4h at 37 °C and 5% CO2 prior to imaging. Movies were recorded overweekend on a Leica confocal SP5 microscope equipped with temperature, humidity, and CO_2 control utilizing a 20X air objective (1 frame/15 min for rat C6, 1 frame/30 min for GBM-7 sub-populations, 1 frame/25 min for NNI-21 FMN1-CTRL/KD). All the brain slice live experiments were performed with brain slice culture medium (68% L-glutamine supplemented DMEM, 26% complete HBSS, 5% FBS, 1% Penicillin-Streptomycin). For immunofluorescence staining of C6 and blood vessels, the co-culture was then fixed with 4% PFA for 20 min and incubated for 1h at room temperature with a blocking solution made of 5% BSA, 5% Normal-Donkey-Serum (NDS) and 0.3% Triton-X 100 in DPBS. The co-culture was incubated overnight at 4 °C with 10 mg/ml of Tomato Lectin (Vector Laboratories, DL-1178) in blocking solution. DAPI was put afterwards. Images were acquired with a Leica SP8 microscope utilizing a 63X oil objective (1 µm Z step).

4.5 Collagen and Matrigel invasion assays

A previous protocol was adapted for collagen and matrigel assays [256]. Briefly, 20 ml of polydimethylsiloxane (PDMS; Sylgard 184 Dow Corning) were casted at 1:10 ratio by mixing curing agent and silicone elastomer base, respectively, in a 10-cm plate. 6-mm PDMS wells were obtained by punching holes with a biopsy puncher in 18x18 mm PDMS squares. The PDMS wells were bound on a 24 mm coverslip via plasma treatment (90 s) followed by 5 min at 80 °C. Each 6-mm well was then treated with 1 mg/ml poly-d-lysine at 37 °C for 3h, rinsed in milliQ water, and cured overnight at 80 °C. Meanwhile, rat C6 spheroids were incubated in medium with 5 µM Dil stain for 3 h, then collected, centrifuged at 500 rpm for 2 minutes and re-suspended in 1 ml of medium. 10 µl of spheroid suspension was then mixed with 80 µl of 6 mg/ml collagen solution (Collagen I from rat tail, Corning #354249 diluted in cell culture medium, 10% v/v 1.2% NaHCO3, 5% 1M HEPES, 1.5% 1M NaOH) or 10 mg/ml Matrigel (reconstituted basement membrane, rBM, Trevigen # 3445-005-01). The spheroids embedded in unpolymerized solutions were placed in the 6-mm PDMS wells and left at 37 °C for 1h to polymerize. With this method between 5 and 15 spheroids per well were obtained. Afterwards, medium was added and movies of invading spheroids were acquired on an IX83 inverted microscope (Olympus) equipped with a Confocal Spinning Disk unit, temperature, humidity, and CO2 control. A 10X objective was utilized, along with an IXON 897 Ultra camera (Andor) and OLYMPUS cellSens Dimension software. Movies were obtained for $>$ 24 hours (1 frame / 15 min for rat C6, 1 frame / 25 min for NNI-21 FMN1-CTRL/KD) with 7.5 µm Z step for RFP and DIC channels.

4.6 Quantification of SP2 with area ratio and MSD

For SP2 in collagen and matrigel assays, SP2 was obtained as the ratio between the area occupied by spheroids at 24 and 0 hours. The area was calculated as the maximum intensity projection firstly in Z, then in time, of the fluorescent channel. For SP2 in 2D flat and grid, the ratio between the areas at 8 and 0 hours was calculated, and the areas were obtained utilizing the maximum intensity projection in time. For MSD calculation we utilized a published protocol [257]. To get XY coordinates overtime, manual tracking was performed with the dedicated plugin in

Fiji. For brain slice, collagen and Matrigel cells were followed for 14 h respectively considering as initial time point 24 h, 10 h and 10 h to fully visualize single cells.

4.7 Generation of radar plots to assess *in vitro* system performance

Radar plots were generated with a survey that included 4 wet-lab members from Gauthier's and Maiuri's lab in IFOM Milan. The participants were blindly asked to evaluate with scores (1 to 5) each experimental parameter in the 5 *in vitro* systems. The final score was obtained by averaging the score of each participant.

4.8 Microcontact printing

Microcontact printing was performed as we extensively described [223]. Briefly, we casted 1:10 PDMS from a dedicated silicon mold, cut it into 1x1 or 1x2 cm^2 stamps, and coated with 50 µg/ml laminin (ThermoFisherScientific, #23017015) in DPBS for 20 min. Each stamp was then air-blow dried, leant on a 35-mm dish, then gently removed. In case of a plastic dish, the surface was then passivated with 0.2% pluronic F127 in DPBS at room temperature for 1 h, whereas for glass poly-l-lysine-grafted polyethylene glycol (0.1 mg/ml, pLL-PEG, SuSoS) was utilized. Dishes were then rinsed 4 times with DPBS and kept in medium until spheroids were seeded. For printing laminin concentrations from 400 to 6.25 µg/ml, a sequence of 6 serial dilutions (1:1 in DPBS) was carried out.

4.9 SP2G experimental and image analysis workflow

In SP2G experimental section, the laminin solution for the gridded micropattern was mixed with 7 µg/ml BSA-conjugated-647 in order to visualize it. Similarly, 1-day old or 5-days old spheroids (for rat C6 or human patient-derived glioma, respectively) were incubated in medium with 5 µM Dil stain for 3 hours in 6-well plates previously passivated with 0.2% pluronic F127. Spheroids were then deposited on the grid and the samples were placed under the microscope and left 5 to 15 min to equilibrate.

Afterwards, 8-hours time-lapse movies were recorded using a 10X objective mounted on a Leica AM TIRF MC system or onto an Olympus ScanR inverted microscope (1 frame / 5 min). 3 channels per time point (phase contrast, Dil stain fluorescence for the cells, BSA-647 fluorescence for the grid) were acquired in live cell imaging for the experiments in Figure 2.14, 2.21. 2 channels per time point were acquired in Figure 2.26, 2.31, since the grid fluorescence was recorded for just 1 frame before and 1 frame after the time-lapse movie. For the experiments in Figure 2.18 cells were not fluorescently labeled and Dil stain channel was not acquired, the drugs were injected 25 min after imaging onset.

For the characterization of cell migration, we utilized the SP2G analytical toolbox that measured the polygonal area A(t). Briefly, as SP2G formed the polygon to track the invasive boundary, the code initially multiplied the binarized grid nodes with the binarized spreading spheroid in order to obtain only the node traveled by at least 1 cell. Then, SP2G iteratively checked whether a node has blinked for at least 3 consecutive time frames. If this condition is met, the node is added to the polygon. Therefore, SP2G always stopped tracking 2 frames earlier than the total duration of any movie. Afterwards, from A(t) we derived the diffusivity D(t) = dA(t) / dt, where dt was the time frame in the time-lapse movies (5 min) and dA(t) was the difference between 2 polygonal areas at subsequent time steps. For the calculation of single cell velocity v(t) = D(t) / (2 $\cdot\sqrt{A(t)}$), being now L = $\sqrt{A(t)}$ the edge of the square having an area equivalent to the polygon, the following 2-equation system was solved:

$$\begin{cases} D(t) = \frac{\delta A(t)}{\delta t} \\ L(t) = \sqrt{A(t)} \end{cases}$$

that inferred

$$D(t) = \frac{\delta L^2(t)}{\delta t} = L \cdot \frac{\delta L(t)}{\delta t} + L \cdot \frac{\delta L(t)}{\delta t} = 2L \cdot \frac{\delta L(t)}{\delta t}$$

The following was then obtained

$$\frac{\delta L(t)}{\delta t} = \frac{\delta A(t)}{\delta t} \cdot \frac{1}{2L} = D(t) \cdot \frac{1}{2\sqrt{A(t)}}$$

that corresponded to the value of the boundary speed. In this way a length gradient was inferred from an area gradient.

For the characterization of the motility modes we extrapolated all the parameters from RA movies and averaged data from several spheroids. Collective migration values were obtained by thresholding each frame of the RA within the last histogram bin, that necessarily spans up to 255 (the maximum value of an 8-bit image). The ratio

$$\frac{\#Counts[Last\ bin]}{\#Total\ Counts}$$

returns the collective migration. The rationale behind this assumption was that collective strands generated high intensity values when averaged, since many cells travelled the same path. Therefore, in the RA movie there were zones of high intensity. Vice versa, single entities generated low intensities when averaged, since no cells other than the single one contributed to the final average value. Background pixels were set to NaN (see Supplementary Appendix).

Directional persistence is calculated through the function "OrientationJ distribution" of the OrientationJ plugin [258], which returns the Orientation Field OF: it consists in 180 values (1 per direction, sampled every 1°). Reasonably, we assumed that the spheroid spreading is isotropic, and therefore SP2G averages the values 0-90, 1-91, etc. and gets 90 values. The following ratio

$$DP = \frac{OF[0°] + OF[1°] + OF[2°] + OF[3°] + OF[87°] + OF[88°] + OF[89°]}{OF[42°] + OF[43°] + OF[44°] + OF[45°] + OF[46°] + OF[47°] + OF[48°]}$$

returns the directional persistence. It is the ratio between the direction of least resistance to cell migration (i.e. the ones provided by the grid segments) and the direction of most resistance (the one a cell has necessarily to face when undergoing a directional change).

4.10 Simulation of particle diffusion

Simulated data were generated with a custom-written code in imageJ/Fiji. Briefly, the function

$$\texttt{Speed\_particle} = \texttt{speed} \cdot \texttt{(1+random("gaussian"))}$$

was applied at each time step to generate motion. "`speed`" was equal to 2, 2.5 or 3 and "`random(\gaussian")`" returned a Gaussian distributed pseudorandom number with mean 0 and standard deviation 1. Continuity was set by imposing a 100% overlap probability to moving particles, pseudo-continuity a 99% probability, pure diffusivity with no constraints.

4.11 RNA sequencing

For the RNA analysis, all the cell lines were plated on laminin at 10 µg/ml and lysed at 70-90% confluency. Libraries for RNA sequencing were prepared following the manufacturer protocols for transcriptome sequencing with the Illumina NextSeq 550DX sequencer (Illumina). For each experimental sample, RNA was extracted using the RNAeasy Mini Kit (Qiagen), its abundance measured using Nanodrop and its integrity assessed using Agilent Bioanalyzer 2100 with Nano Rna kit (RIN $>$ 8). mRNA-seq indexed library preparation was performed starting from 500 ng of total RNA with the Illumina ligation stranded mRNA (Illumina) according to the manufacturer's instructions. Indexed libraries were quality controlled on Agilent Bioanalyzer 2100 with High Sensitivity DNA kit, quantified with Qubit HS DNA, normalized and pooled to perform a multiplexed sequencing run. 1% PhiX control was added to the sequencing pool, to serve as a positive run control. Sequencing was performed in PE mode (2x75nt) on an Illumina NextSeq550Dx platform, generating on average 50 millions PE reads per sample.

4.12 RNA extraction and qPCR analysis

RNA was extracted with the RNAeasy Mini Kit (Qiagen) as per manufacturer specifications. Real-time PCR performed with a 7500 Real-Time PCR System (Thermo

Fisher). The following parameters were utilized: pre-PCR step of 20 s at 95 °C, followed by 40 cycles of 1 s at 95 °C and 20 s at 60 °C. Samples were amplified with primers and probes for each target, and for all the targets, one NTC sample was run. Raw data (Ct) were analyzed with Excel using the DDCT method to calculate the relative fold gene expression. DCT was calculated using 2 housekeeping genes and averaged. For the mRNA expression of selected integrins data were normalized against the expression of the GBM7 sub-population #03.

4.13 Analysis of RNA sequencing data

Reads were aligned to the GRCh38/hg38 assembly human reference genome using the STAR aligner (v 2.6.1d; [259]) and reads were quantified using Salmon (v1.4.0; [260]). Differential gene expression analysis was performed using the Bioconductor package DESeq2 (v 1.30.0; [261]) that estimates variance-mean dependence in count data from high-throughput sequencing data and tests for differential expression exploiting a negative binomial distribution-based model. Preranked GSEA for evaluating pathway enrichment in transcriptional data was carried out using the Bioconductor package fgsea [262], taking advantage of the Kyoto Encyclopedia of Genes and Genomes (KEGG) gene set available from the GSEA Molecular Signatures Database (https://www.gsea-msigdb.org/gsea/msigdb/genesets.jsp?collections).

4.14 Protein extraction and western blots

Total cell extracts were prepared in RIPA buffer (100 mM NaCl; 1 mM EGTA; 50 mM Tris pH7.4; 1% TX100) complemented with a cocktail of protease inhibitors (Roche). Proteins were quantified using the Pierce BCA protein assay kit #23225 (ThermoScientific). Proteins were denatured with SDS and resolved by SDS-PAGE using typically 8% acrylamide gels. Transfers were done on Polyvinylidene Fluoride (PVDF) membranes in methanol-containing transfer buffer. Blocking was typically done with milk diluted to 5% in PBS-0.1% tween for 1h at room temperature and antibodies were blotted overnight at 4 °C. HRP-secondary antibodies were incubated for 1-2 hours at room temperature in 5% milk and ECL were performed using the Amersham ECL Western Blotting Detection Reagents (Cat.no. RPN2106 from GE Healthcare). Detection was done using CL-Xposure films (Cat.no. 34089 from

Thermoscientific).

The following antibodies were used: anti-CX43 Sigma C6219, recombinant anti-GAP43 antibody [EP890Y] from Abcam (ab75810), anti p120 catenin from BD Biosciences AB_397537, anti-integrin alpha V (Abcam ab179475, diluted 1:1000), anti-integrin alpha 6 (Novus NBP1-85747, diluted 1:500).

4.15 Statistical analysis and data availability

All the statistical analysis was performed with Prism 9 (GraphPad). P-values were calculated as indicated in figure legends, as well as number of samples and independent experiments. The plots were generated with Prism 9 and ggplot2. Google sheets was utilized for the radar plots in Figure 2.10. Kolmogorov-Smirnov tests were performed on Matlab utilizing the function kstest2(groupA, groupB, 'Alpha', 0.05).

All the ImageJ/Fiji macros developed for SP2G and the Supplementary Appendix including instructions on how to run the codes are publicly available on the figshare repository https://figshare.com/projects/SP2G/148246.

4.16 Calcium imaging and wave propagation

Upon microcontact printing, confluent cells were co-loaded with the Ca^{2+} indicator Rhod-2-AM (5 µM, ThermoFisher R1244) and the Ca^{2+} chelator DMNP-EDTA-AM (5 µM, ThermoFisher D6814) and incubated for 1 hour.

We performed imaging with a two-photon laser-scanning microscope (Leica SP5 microscope fitted with a 40X objective lens) directly coupled to a 2-photon laser. For 2-photon photolysis we tuned the laser to 730 nm for maximum Ca^{2+} uncaging of DMNP-EDTA and excitation of Rhod-2. Laser intensities were the lowest possible for uncaging. Flash durations of 250 ms produced repeatable small transients. The laser intensity was carefully increased beyond the point for the initial transient event until a large Ca^{2+} transient characteristic of internal release occurred within the glioma cells that then induced a Ca^{2+} wave that propagated throughout the cell network. The pre-bleach window of time-lapse movies lasted 30 s, the post-bleach 180 s. Analysis was performed with ImageJ/Fiji.

4.17 SP2G experimental protocol

4.17.1 Materials

- Glioma Stem Cell (GSC) medium (or the medium necessary if other cell types are used)
- B27 mix (ThermoFisherScientific 17504044)
- 35mm glass-bottom/plastic dish
- 0.2% pluronic acid
- Cell culture 6-well
- Laminin
- DPBS
- Fluorescent BSA (ThermoFisherScientific A34785)
- Dil stain (ThermoFisherScientific D282)

4.17.2 DilC18 membrane dye preparation

MW = 933.88 g/mol. Stock prepared at 5 mM in DMSO: 933.88 g/mol * 0.005 mol/l = 4.665 g/l. Then, 4.665 mg of dye diluted in 1 ml DMSO. Aliquoted in 6ul aliquots and stored at 4 °C in the dark.

4.17.3 Microcontact printing

Done as [223] on glass bottom dishes with 7 µm wide grid. Fluorescent BSA is mixed in the solution at 1/7 ratio compared to laminin concentration. That is, given that we print laminin at 50 ug/ml, the corresponding BSA concentration will be 50/7 = 7 µg/ml. BSA was aliquoted at 1 mg/ml and stored at 4 °C in the dark. Given that volumes will be small, BSA volume is just added to the laminin solution.

4.17.4 Spheroid spreading

- Treat a 6-well with 0.2% pluronic acid for 30 min. 2 wells will be enough, 4 is better to have an extra back-up.

- Wash 4X in DPBS each well.
- Add 1.5ml GSC medium and B27 mix to each well.
- From a confluent dish (i.e. grown for 4-5 days) of glioma spheroids, gently withdraw 400 µL of sphere suspension and transfer it to a well of the multi-well. Do it for all the wells functionalized with pluronic acid.
  Remarks:
  - *if the number of sphere is higher than usual withdraw 300 µL of sphere suspension.*
  - *Any other well could be used, but 6-well is preferable since it has the same dimension of 35-mm dish that was functionalized via microcontact printing before. Useful to evaluate spheroid confluency in a support having the same dimension of the support that will be used for imaging.*
  - *If spheroids are coming from a 6-well, then withdraw 800 ul of sphere suspension and put 1ml upon DPBS washes.*
- Equilibrate each well up to 2 ml with GSC medium + B27 mix solution.
- Dil stain: working concentration is 5 µM. Dilute 5ul Dil stain in 995 ul of GSC medium + B27 mix.
- Add 500 µL of dye solution to half of the wells to stain cells.
- Add 500 µL of GSC medium + B27 mix to each well without dye.
  Remark: half of the wells will be dye-free, so spheroids will not be stained. Dye-free spheroids will be used on the dishes where microcontact printing solution was BSA-free to create a fluorescent-free control condition.
- Leave spheroids (move well gently to avoid spheroid clumping) at 37 °C for 4h for dye incubation.
- Take suspensions (1 with dye, 1 without dye) and transfer them in 2 15-ml falcon tubes.
- Centrifuge 500 rpm for 2 min.
  Remark: this centrifugation regime is enough to precipitate most of the spheres and leaves the single cells floating. Important step to get a clean imaging.

- Aspire solution as much as possible (to get rid of DMSO in the dye-containing solution) and replace with 1 ml GSC medium + B27 mix.
- Give 5-7 gentle strokes to resuspend spheres.
- Take 200 µl of sphere suspension and inject it in the 35-mm dish functionalized with microcontact printing.
  Remarks:
  - *usually 1/5 of the suspension gives a good confluency. What is important is to have sparse spheres on the grid such that they are not too close in an imaging field of view. The trade-off is between sphere number and sphere distance: 2 spheres should not fall in the same region covered by the camera size of the microscope.*
  - *If uncertain about the sphere number to inject in the 35 mm dish, start with a low volume and then increase upon checking. If too many spheres are injected it may be troublesome to wash them away.*
- Imaging: use any time-lapse microscope equipped with temperature, CO_2 control and fluorescence lamps. 1 frame / 5 min. Further details in the Supplementary Appendix.

Bibliography

[1] David N Louis, Arie Perry, Pieter Wesseling, Daniel J Brat, Ian A Cree, Dominique Figarella-Branger, Cynthia Hawkins, HK Ng, Stefan M Pfister, Guido Reifenberger, et al. The 2021 who classification of tumors of the central nervous system: a summary. *Neuro-oncology*, 23(8):1231–1251, 2021.

[2] HJ Scherer. A critical review: the pathology of cerebral gliomas. *Journal of neurology and psychiatry*, 3(2):147, 1940.

[3] George St Stoyanov and Deyan L Dzhenkov. On the concepts and history of glioblastoma multiforme—morphology, genetics and epigenetics. *Folia Med*, 60(1):48–66, 2018.

[4] Theodore M Brown and Elizabeth Fee. Rudolf carl virchow: medical scientist, social reformer, role model. *American journal of public health*, 96(12):2104–2105, 2006.

[5] Rudolf Virchow. *Cellular Pathology as based upon physiological and pathological histology. Twenty lectures delivered in... 1858. Translated from the second edition of the original by F. Chance. With notes and numerous emendations principally from MS. notes of the author, and illustrated by... engravings on wood.* 1860.

[6] Rudolf Virchow. *Die krankhaften Geschwülste; dreissig Vorlesungen: gehalten während des Wintersemesters 1862-1863 an der Universität zu Berlin*, volume 2. Hirschwald, 1865.

[7] Nicola J Allen and Ben A Barres. Glia—more than just brain glue. *Nature*, 457(7230):675–677, 2009.

[8] David N Louis, Arie Perry, Guido Reifenberger, Andreas Von Deimling, Dominique Figarella-Branger, Webster K Cavenee, Hiroko Ohgaki, Otmar D Wiestler, Paul Kleihues, and David W Ellison. The 2016 world health organization classification of tumors of the central nervous system: a summary. *Acta neuropathologica*, 131(6):803–820, 2016.

[9] Camillo Golgi. Sulla sostanza grigia del cervello. *Gazetta Medica Italiana*, 33:244–246, 1873.

[10] Paolo Mazzarello. From images to physiology: a strange paradox at the origin of modern neuroscience. *Progress in brain research*, 243:233–256, 2018.

[11] Fernando De Castro. Cajal and the spanish neurological school: neuroscience would have been a different story without them. *Frontiers in Cellular Neuroscience*, 13:187, 2019.

[12] Paul Nurse. The incredible life and times of biological cells. *Science*, 289(5485):1711–1716, 2000.

[13] Guido Cimino. Reticular theory versus neuron theory in the work of camillo golgi. *Physis; rivista internazionale di storia della scienza*, 36(2):431–472, 1999.

[14] N Chu. Centennial of the nobel prize for golgi and cajal-founding of modern neuroscience and irony of discovery. *Acta Neurologica Taiwanica*, 15(3):217, 2006.

[15] H Stroebe. Ueber entstehung und bau der gehirngliome. *Beitr Path Anat*, 18:405–486, 1895.

[16] Mihály Lenhossék. *Der feinere Bau des Nervensystems im Lichte neuester Forschungen*. Fischer, 1893.

[17] W Lloyd Andriezen. The neuroglia elements in the human brain. *British medical journal*, 2(1700):227, 1893.

[18] Pío DEL RIO-HORTEGA. El tercer elemento de los centros nerviosos. i. la microglia en estado normal ii. intervencion de la microglia en los procesos patologicos. hi. naturaleza probable de la microglia. *Boll Socieded Esp Biol*, 9:69–120, 1919.

[19] Amandip S Gill and Devin K Binder. Wilder penfield, pio del rio-hortega, and the discovery of oligodendroglia. *Neurosurgery*, 60(5):940–948, 2007.

[20] Alexei Verkhratsky, Margaret S Ho, Robert Zorec, and Vladimir Parpura. The concept of neuroglia. *Neuroglia in Neurodegenerative Diseases*, pages 1–13, 2019.

[21] Helmut Kettenmann and Alexei Verkhratsky. Neuroglia: the 150 years after. *Trends in neurosciences*, 31(12):653–659, 2008.

[22] Percival Bailey and Harvey Cushing. *A classification of the tumors of the glioma group on a histogenetic basis with a correlated study of prognosis*. Lippincott, 1926.

[23] Sherise Ferguson and Maciej S Lesniak. Percival bailey and the classification of brain tumors. *Neurosurgical focus*, 18(4):1–6, 2005.

[24] HJ Scherer. Structural development in gliomas. *The American Journal of Cancer*, 34(3):333–351, 1938.

[25] Jürgen Peiffer and Paul Kleihues. Hans-joachim scherer (1906-1945), pioneer in glioma research. *Brain pathology*, 9(2):241–245, 1999.

[26] Ana Martin-Villalba, Ali Fuat Okuducu, and Andreas Von Deimling. The evolution of our understanding on glioma. *Brain Pathology*, 18(3):455–463, 2008.

[27] John J Kepes, Lucien J Rubinstein, and Lawrence F Eng. Pleomorphic xanthoastrocytoma: A distinctive meningocerebral glioma of young subjects with relatively favorable prognosis a study of 12 cases. *Cancer*, 44(5):1839–1852, 1979.

[28] Daniel J Brat, Bernd W Scheithauer, Susan M Staugaitis, Selina C Cortez, Keith Brecher, and Peter C Burger. Third ventricular chordoid glioma: a distinct clinicopathologic entity. *Journal of Neuropathology & Experimental Neurology*, 57(3):283–290, 1998.

[29] George S Stoyanov, Deyan Dzhenkov, Peter Ghenev, Bogomil Iliev, Yavor Enchev, and Anton B Tonchev. Cell biology of glioblastoma multiforme: from basic science to diagnosis and treatment. *Medical Oncology*, 35(3):1–10, 2018.

[30] W Neal Burnette. "western blotting": electrophoretic transfer of proteins from sodium dodecyl sulfate-polyacrylamide gels to unmodified nitrocellulose and radiographic detection with antibody and radioiodinated protein a. *Analytical biochemistry*, 112(2):195–203, 1981.

[31] Randall K Saiki, Stephen Scharf, Fred Faloona, Kary B Mullis, Glenn T Horn, Henry A Erlich, and Norman Arnheim. Enzymatic amplification of β-globin genomic sequences and restriction site analysis for diagnosis of sickle cell anemia. *Science*, 230(4732):1350–1354, 1985.

[32] Manel Esteller, Jesus Garcia-Foncillas, Esther Andion, Steven N Goodman, Oscar F Hidalgo, Vicente Vanaclocha, Stephen B Baylin, and James G Herman. Inactivation of the dna-repair gene mgmt and the clinical response of gliomas to alkylating agents. *New England Journal of Medicine*, 343(19):1350–1354, 2000.

[33] Hai Yan, D Williams Parsons, Genglin Jin, Roger McLendon, B Ahmed Rasheed, Weishi Yuan, Ivan Kos, Ines Batinic-Haberle, Siân Jones, Gregory J Riggins, et al. Idh1 and idh2 mutations in gliomas. *New England journal of medicine*, 360(8):765–773, 2009.

[34] J Gregory Cairncross, Keisuke Ueki, Magdelena C Zlatescu, David K Lisle, Dianne M Finkelstein, Robert R Hammond, Jonathan S Silver, Paul C Stark, David R Macdonald, Yasushi Ino, et al. Specific genetic predictors of chemotherapeutic response and survival in patients with anaplastic oligodendrogliomas. *JNCI: Journal of the National Cancer Institute*, 90(19):1473–1479, 1998.

[35] Ines Crespo, Ana Louisa Vital, María Gonzalez-Tablas, María del Carmen Patino, Alvaro Otero, María Celeste Lopes, Catarina de Oliveira, Patricia Domingues, Alberto Orfao, and Maria Dolores Tabernero. Molecular and genomic alterations in glioblastoma multiforme. *The American journal of pathology*, 185(7):1820–1833, 2015.

[36] Tatyana N Ignatova, Valery G Kukekov, Eric D Laywell, Oleg N Suslov, Frank D Vrionis, and Dennis A Steindler. Human cortical glial tumors contain neural stem-like cells expressing astroglial and neuronal markers in vitro. *Glia*, 39(3):193–206, 2002.

[37] Sheila K Singh, Ian D Clarke, Mizuhiko Terasaki, Victoria E Bonn, Cynthia Hawkins, Jeremy Squire, and Peter B Dirks. Identification of a cancer stem cell in human brain tumors. *Cancer research*, 63(18):5821–5828, 2003.

[38] Amy H Yin, Sheri Miraglia, Esmail D Zanjani, Graca Almeida-Porada, Makio Ogawa, Anne G Leary, Johanna Olweus, John Kearney, and David W Buck. Ac133, a novel marker for human hematopoietic stem and progenitor cells. *Blood, The Journal of the American Society of Hematology*, 90(12):5002–5012, 1997.

[39] Urban Lendahl, Lyle B Zimmerman, and Ronald DG McKay. Cns stem cells express a new class of intermediate filament protein. *Cell*, 60(4):585–595, 1990.

[40] Rossella Galli, Elena Binda, Ugo Orfanelli, Barbara Cipelletti, Angela Gritti, Simona De Vitis, Roberta Fiocco, Chiara Foroni, Francesco Dimeco, and Angelo Vescovi. Isolation and characterization of tumorigenic, stem-like neural precursors from human glioblastoma. *Cancer research*, 64(19):7011–7021, 2004.

[41] Martin C Raff, Rhona Mirsky, KL Fields, ROBERT P LISAK, SUSAN H DORFMAN, DONALD H SILBERBERG, NA Gregson, SIDNEY LEIBOWITZ, and MARY C KENNEDY. Galactocerebroside is a specific cell-surface antigenic marker for oligodendrocytes in culture. *Nature*, 274(5673):813–816, 1978.

[42] Sheila K Singh, Cynthia Hawkins, Ian D Clarke, Jeremy A Squire, Jane Bayani, Takuichiro Hide, R Mark Henkelman, Michael D Cusimano, and Peter B Dirks. Identification of human brain tumour initiating cells. *nature*, 432(7015):396–401, 2004.

[43] Shideng Bao, Qiulian Wu, Roger E McLendon, Yueling Hao, Qing Shi, Anita B Hjelmeland, Mark W Dewhirst, Darell D Bigner, and Jeremy N Rich. Glioma stem cells promote radioresistance by preferential activation of the dna damage response. *nature*, 444(7120):756–760, 2006.

[44] Roel GW Verhaak, Katherine A Hoadley, Elizabeth Purdom, Victoria Wang, Yuan Qi, Matthew D Wilkerson, C Ryan Miller, Li Ding, Todd Golub, Jill P Mesirov, et al. Integrated genomic analysis identifies clinically relevant subtypes of glioblastoma characterized by abnormalities in pdgfra, idh1, egfr, and nf1. *Cancer cell*, 17(1):98–110, 2010.

[45] Cameron W Brennan, Roel GW Verhaak, Aaron McKenna, Benito Campos, Houtan Noushmehr, Sofie R Salama, Siyuan Zheng, Debyani Chakravarty, J Zachary Sanborn, Samuel H Berman, et al. The somatic genomic landscape of glioblastoma. *cell*, 155(2):462–477, 2013.

[46] Anoop P Patel, Itay Tirosh, John J Trombetta, Alex K Shalek, Shawn M Gillespie, Hiroaki Wakimoto, Daniel P Cahill, Brian V Nahed, William T Curry, Robert L Martuza, et al. Single-cell rna-seq highlights intratumoral heterogeneity in primary glioblastoma. *Science*, 344(6190):1396–1401, 2014.

[47] Yuan Xie, Tobias Bergström, Yiwen Jiang, Patrik Johansson, Voichita Dana Marinescu, Nanna Lindberg, Anna Segerman, Grzegorz Wicher, Mia Niklasson, Sathishkumar Baskaran, et al. The human glioblastoma cell culture resource: validated cell models representing all molecular subtypes. *EBioMedicine*, 2(10):1351–1363, 2015.

[48] Cyril Neftel, Julie Laffy, Mariella G Filbin, Toshiro Hara, Marni E Shore, Gilbert J Rahme, Alyssa R Richman, Dana Silverbush, McKenzie L Shaw, Christine M Hebert, et al. An integrative model of cellular states, plasticity, and genetics for glioblastoma. *Cell*, 178(4):835–849, 2019.

[49] SGM Piccirillo, R Combi, L Cajola, A Patrizi, S Redaelli, A Bentivegna, S Baronchelli, G Maira, B Pollo, A Mangiola, et al. Distinct pools of cancer stem-like cells coexist within human glioblastomas and display different tumorigenicity and independent genomic evolution. *Oncogene*, 28(15):1807–1811, 2009.

[50] Johanna Klughammer, Barbara Kiesel, Thomas Roetzer, Nikolaus Fortelny, Amelie Nemc, Karl-Heinz Nenning, Julia Furtner, Nathan C Sheffield, Paul Datlinger, Nadine Peter, et al. The dna methylation landscape of glioblastoma disease progression shows extensive heterogeneity in time and space. *Nature medicine*, 24(10):1611–1624, 2018.

[51] Xi Lu, Naga Prathyusha Maturi, Malin Jarvius, Irem Yildirim, Yonglong Dang, Linxuan Zhao, Yuan Xie, E Tan, Pengwei Xing, Rolf Larsson, et al. Cell-lineage controlled epigenetic regulation in glioblastoma stem cells determines functionally distinct subgroups and predicts patient survival. *Nature Communications*, 13(1):1–16, 2022.

[52] Spyros Darmanis, Steven A Sloan, Derek Croote, Marco Mignardi, Sophia Chernikova, Peyman Samghababi, Ye Zhang, Norma Neff, Mark Kowarsky, Christine Caneda, et al. Single-cell rna-seq analysis of infiltrating neoplastic cells at the migrating front of human glioblastoma. *Cell reports*, 21(5):1399–1410, 2017.

[53] Jiguang Wang, Emanuela Cazzato, Erik Ladewig, Veronique Frattini, Daniel IS Rosenbloom, Sakellarios Zairis, Francesco Abate, Zhaoqi Liu, Oliver Elliott, Yong-Jae Shin, et al. Clonal evolution of glioblastoma under therapy. *Nature genetics*, 48(7):768–776, 2016.

[54] Véronique G LeBlanc, Diane L Trinh, Shaghayegh Aslanpour, Martha Hughes, Dorothea Livingstone, Dan Jin, Bo Young Ahn, Michael D Blough, J Gregory Cairncross, Jennifer A Chan, et al. Single-cell landscapes of primary glioblastomas and matched explants and cell lines show variable retention of inter-and intratumor heterogeneity. *Cancer Cell*, 40(4):379–392, 2022.

[55] Damian Stichel, Azadeh Ebrahimi, David Reuss, Daniel Schrimpf, Takahiro Ono, Mitsuaki Shirahata, Guido Reifenberger, Michael Weller, Daniel Hänggi, Wolfgang Wick, et al. Distribution of egfr amplification, combined chromosome 7 gain and chromosome 10 loss, and tert promoter mutation in brain tumors and their potential for the reclassification of idhwt astrocytoma to glioblastoma. *Acta neuropathologica*, 136(5):793–803, 2018.

[56] Dennis Lee, Robert A Riestenberg, Aden Haskell-Mendoza, and Orin Bloch. Diffuse astrocytic glioma, idh-wildtype, with molecular features of glioblastoma, who grade iv: A single-institution case series and review. *Journal of Neuro-Oncology*, 152(1):89–98, 2021.

[57] Nathalie Olympios, Vianney Gilard, Florent Marguet, Florian Clatot, Frédéric Di Fiore, and Maxime Fontanilles. Tert promoter alterations in glioblastoma: a systematic review. *Cancers*, 13(5):1147, 2021.

[58] Sandra H Bigner, Joachim Mark, Peter C Burger, M Stephen Mahaley Jr, Dennis E Bullard, Lawrence H Muhlbaier, and Darell D Bigner. Specific chromosomal abnormalities in malignant human gliomas. *Cancer Research*, 48(2):405–411, 1988.

[59] Rickman J Godlee and Hughes Bennett. The excision of a tumor from the brain. *The Journal of Nervous and Mental Disease*, 12(2):247, 1885.

[60] Ian E McCutcheon and Mark C Preul. Historical perspective on surgery and survival with glioblastoma: how far have we come? *World Neurosurgery*, 149:148–168, 2021.

[61] Harvey Cushing. *The special field of neurological surgery: five years later*. Friedenwald Company, 1910.

[62] Harvey Cushing. The establishment of cerebral hernia as a decompressive measure for inaccessible brain tumors: with the description of intermuscular methods of making the bone defect in temporal and occipital regions. *Surg Gynecol Obstet*, 1:297–314, 1905.

[63] Howard H Tooth. Some observations on the growth and survival-period of intracranial tumours, based on the records of 500 cases, with special reference to the pathology of the gliomata. *Brain*, 35(2):61–108, 1912.

[64] Walter E Dandy. Ventriculography following the injection of air into the cerebral ventricles. *Annals of surgery*, 68(1):5, 1918.

[65] Egas Moniz. Liencephalograhie arterielle, son importance dans la location des tumeurs cerebrales. *Rev Neurol*, 2:72–90, 1927.

[66] AR Elvidge. The gliomas of the central nervous system. a study of two hundred and ten verified cases. In *Proc Assoc Res Nerv Ment Dis*, volume 16, pages 107–181, 1935.

[67] John G Roth and Arthur R Elvidge. Glioblastoma multiforme: a clinical survey. *Journal of neurosurgery*, 17(4):736–750, 1960.

[68] Richard Jelsma and Paul C Bucy. The treatment of glioblastoma multiforme of the brain. *Journal of neurosurgery*, 27(5):388–400, 1967.

[69] Allan M Cormack. Early two-dimensional reconstruction and recent topics stemming from it. *Science*, 209(4464):1482–1486, 1980.

[70] FH Doyle, JM Pennock, JS Orr, JC Gore, GM Bydder, RE Steiner, IR Young, H Clow, DR Bailes, M Burl, et al. Imaging of the brain by nuclear magnetic resonance. *The Lancet*, 318(8237):53–57, 1981.

[71] Michael D Walker, Sylvan B Green, David P Byar, Eben Alexander Jr, Ulrich Batzdorf, William H Brooks, William E Hunt, Collin S MacCarty, M Stephen Mahaley Jr, John Mealey Jr, et al. Randomized comparisons of radiotherapy and nitrosoureas for the treatment of malignant glioma after surgery. *New England Journal of Medicine*, 303(23):1323–1329, 1980.

[72] CH Chang, J Horton, D Schoenfeld, O Salazer, R Perez-Tamayo, S Kramer, A Weinstein, JS Nelson, and Y Tsukada. Comparison of postoperative radiotherapy and combined postoperative radiotherapy and chemotherapy in the multidisciplinary management of malignant gliomas. a joint radiation therapy oncology group and eastern cooperative oncology group study. *Cancer*, 52(6):997–1007, 1983.

[73] Roger Stupp, Warren P Mason, Martin J Van Den Bent, Michael Weller, Barbara Fisher, Martin JB Taphoorn, Karl Belanger, Alba A Brandes, Christine Marosi, Ulrich Bogdahn, et al. Radiotherapy plus concomitant and adjuvant temozolomide for glioblastoma. *New England journal of medicine*, 352(10):987–996, 2005.

[74] Eric C Holland. Glioblastoma multiforme: the terminator. *Proceedings of the National Academy of Sciences*, 97(12):6242–6244, 2000.

[75] Fred H Hochberg and Amy Pruitt. Assumptions in the radiotherapy of glioblastoma. *Neurology*, 30(9):907–907, 1980.

[76] Ulrich Batzdorf and Nathan Malamud. The problem of multicentric gliomas. *Journal of neurosurgery*, 20(2):122–136, 1963.

[77] Vishnu Anand Cuddapah, Stefanie Robel, Stacey Watkins, and Harald Sontheimer. A neurocentric perspective on glioma invasion. *Nature Reviews Neuroscience*, 15(7):455–465, 2014.

[78] Patrick Beauchesne. Extra-neural metastases of malignant gliomas: myth or reality? *Cancers*, 3(1):461–477, 2011.

[79] Renato V Iozzo and Liliana Schaefer. Proteoglycan form and function: A comprehensive nomenclature of proteoglycans. *Matrix biology*, 42:11–55, 2015.

[80] Dieter R Zimmermann and María T Dours-Zimmermann. Extracellular matrix of the central nervous system: from neglect to challenge. *Histochemistry and cell biology*, 130(4):635–653, 2008.

[81] Pavlo G. Gritsenko, Olga Ilina, and Peter Friedl. Interstitial guidance of cancer invasion. *The Journal of pathology*, 226(2):185–199, 2012.

[82] Rolf Mentlein, Kirsten Hattermann, and Janka Held-Feindt. Lost in disruption: role of proteases in glioma invasion and progression. *Biochimica et Biophysica Acta (BBA)-Reviews on Cancer*, 1825(2):178–185, 2012.

[83] Angret Joester and Andreas Faissner. The structure and function of tenascins in the nervous system. *Matrix Biology*, 20(1):13–22, 2001.

[84] Nicole Brösicke, Frank KH van Landeghem, Björn Scheffler, and Andreas Faissner. Tenascin-c is expressed by human glioma in vivo and shows a strong association with tumor blood vessels. *Cell and tissue research*, 354(2):409–430, 2013.

[85] Tim Demuth and Michael E Berens. Molecular mechanisms of glioma cell migration and invasion. *Journal of neuro-oncology*, 70(2):217–228, 2004.

[86] Berit B Tysnes, Lone F Larsen, Gro O Ness, Rupavathana Mahesparan, Klaus Edvardsen, Inmaculada Garcia-Cabrera, and Rolf Bjerkvig. Stimulation of glioma-cell migration by laminin and inhibition by anti-α3 and anti-β1 integrin antibodies. *International journal of cancer*, 67(6):777–784, 1996.

[87] Joerg-Christian Tonn, Siglinde Kerkau, Anne Hanke, Hakim Bouterfa, Justus G Mueller, Sven Wagner, Giles Hamilton Vince, and Klaus Roosen. Effect of synthetic matrix-metalloproteinase inhibitors on invasive capacity and proliferation of human malignant gliomas in vitro. *International journal of cancer*, 80(5):764–772, 1999.

[88] Adrienne Weeks, Nadia Okolowsky, Brian Golbourn, Stacey Ivanchuk, Christian Smith, and James T Rutka. Ect2 and rasal2 mediate mesenchymal-amoeboid transition in human astrocytoma cells. *The American journal of pathology*, 181(2):662–674, 2012.

[89] Eishu Hirata, Hiroko Yukinaga, Yuji Kamioka, Yoshiki Arakawa, Susumu Miyamoto, Takaharu Okada, Erik Sahai, and Michiyuki Matsuda. In vivo fluorescence resonance energy transfer imaging reveals differential activation of rho-family gtpases in glioblastoma cell invasion. *Journal of cell science*, 125(4):858–868, 2012.

[90] Ryan J Petrie and Kenneth M Yamada. Multiple mechanisms of 3d migration: the origins of plasticity. *Current opinion in cell biology*, 42:7–12, 2016.

[91] Pascale Monzo, Yuk Kien Chong, Charlotte Guetta-Terrier, Anitha Krishnasamy, Sharvari R Sathe, Evelyn KF Yim, Wai Hoe Ng, Beng Ti Ang, Carol Tang, Benoit Ladoux, et al. Mechanical confinement triggers glioma linear migration dependent on formin fhod3. *Molecular biology of the cell*, 27(8):1246–1261, 2016.

[92] Pascale Monzo, Michele Crestani, Yuk Kien Chong, Andrea Ghisleni, Katharina Hennig, Qingsen Li, Nikolaos Kakogiannos, Monica Giannotta, Cristina Richichi, Tania Dini, et al. Adaptive mechanoproperties mediated by the formin fmn1 characterize glioblastoma fitness for invasion. *Developmental cell*, 56(20):2841–2855, 2021.

[93] Anne J Ridley, Martin A Schwartz, Keith Burridge, Richard A Firtel, Mark H Ginsberg, Gary Borisy, J Thomas Parsons, and Alan Rick Horwitz. Cell migration: integrating signals from front to back. *Science*, 302(5651):1704–1709, 2003.

[94] Christopher Beadle, Marcela C Assanah, Pascale Monzo, Richard Vallee, Steven S Rosenfeld, and Peter Canoll. The role of myosin ii in glioma invasion of the brain. *Molecular biology of the cell*, 19(8):3357–3368, 2008.

[95] Aurelio Ariza, Dolores López, Jose L Mate, Marc Isamat, Eva Musulen, Magda Pujol, Adolfo Ley, and JoséJ Navas-palacios. Role of cd44 in the invasiveness of glioblastoma multiforme and the noninvasiveness of meningioma: an immunohistochemistry study. *Human pathology*, 26(10):1144–1147, 1995.

[96] Yushan Kim and Sanjay Kumar. Cd44-mediated adhesion to hyaluronic acid contributes to mechanosensing and invasive motilitycd44 adhesion, mechanosensing, and motility. *Molecular Cancer Research*, 12(10):1416–1429, 2014.

[97] JMPC Holash, PC Maisonpierre, D Compton, P Boland, CR Alexander, D Zagzag, GD Yancopoulos, and SJ Wiegand. Vessel cooption, regression, and growth in tumors mediated by angiopoietins and vegf. *Science*, 284(5422):1994–1998, 1999.

[98] Vedrana Montana and Harald Sontheimer. Bradykinin promotes the chemotactic invasion of primary brain tumors. *Journal of Neuroscience*, 31(13):4858–4867, 2011.

[99] Romeo Cecchelli, Vincent Berezowski, Stefan Lundquist, Maxime Culot, Mila Renftel, Marie-Pierre Dehouck, and Laurence Fenart. Modelling of the blood–brain barrier in drug discovery and development. *Nature reviews Drug discovery*, 6(8):650–661, 2007.

[100] N Joan Abbott, Adjanie AK Patabendige, Diana EM Dolman, Siti R Yusof, and David J Begley. Structure and function of the blood–brain barrier. *Neurobiology of disease*, 37(1):13–25, 2010.

[101] G Bellon, T Caulet, Y Cam, M Pluot, G Poulin, M Pytlinska, and MH Bernard. Immunohistochemical localisation of macromolecules of the basement membrane and extracellular matrix of human gliomas and meningiomas. *Acta neuropathologica*, 66(3):245–252, 1985.

[102] Rodney D McComb and Darell D Bigner. Immunolocalization of laminin in neoplasms of the central and peripheral nervous systems. *Journal of Neuropathology & Experimental Neurology*, 44(3):242–253, 1985.

[103] Candece L Gladson. The extracellular matrix of gliomas: modulation of cell function. *Journal of neuropathology and experimental neurology*, 58(10):1029, 1999.

[104] Jeffrey J Iliff, Minghuan Wang, Yonghong Liao, Benjamin A Plogg, Weiguo Peng, Georg A Gundersen, Helene Benveniste, G Edward Vates, Rashid Deane, Steven A Goldman, et al. A paravascular pathway facilitates csf flow through the brain parenchyma and the clearance of interstitial solutes, including amyloid β. *Science translational medicine*, 4(147):147ra111–147ra111, 2012.

[105] Azadeh Farin, Satoshi O Suzuki, Michael Weiker, James E Goldman, Jeffrey N Bruce, and Peter Canoll. Transplanted glioma cells migrate and proliferate on host brain vasculature: a dynamic analysis. *Glia*, 53(8):799–808, 2006.

[106] Frank Winkler, Yvonne Kienast, Martin Fuhrmann, Louisa Von Baumgarten, Steffen Burgold, Gerda Mitteregger, Hans Kretzschmar, and Jochen Herms. Imaging glioma cell invasion in vivo reveals mechanisms of dissemination and peritumoral angiogenesis. *Glia*, 57(12):1306–1315, 2009.

[107] Stacey Watkins, Stefanie Robel, Ian F Kimbrough, Stephanie M Robert, Graham Ellis-Davies, and Harald Sontheimer. Disruption of astrocyte–vascular coupling and the blood–brain barrier by invading glioma cells. *Nature communications*, 5(1):1–15, 2014.

[108] Peter Friedl and Stephanie Alexander. Cancer invasion and the microenvironment: plasticity and reciprocity. *Cell*, 147(5):992–1009, 2011.

[109] Stacey Watkins and Harald Sontheimer. Hydrodynamic cellular volume changes enable glioma cell invasion. *Journal of Neuroscience*, 31(47):17250–17259, 2011.

[110] Nadia Aalling Jessen, Anne Sofie Finmann Munk, Iben Lundgaard, and Maiken Nedergaard. The glymphatic system: a beginner's guide. *Neurochemical research*, 40(12):2583–2599, 2015.

[111] Andrew Bacyinski, Maosheng Xu, Wei Wang, and Jiani Hu. The paravascular pathway for brain waste clearance: current understanding, significance and controversy. *Frontiers in neuroanatomy*, 11:101, 2017.

[112] Davide Schiffer, Marta Mellai, Enrica Bovio, Ilaria Bisogno, Cristina Casalone, and Laura Annovazzi. Glioblastoma niches: From the concept to the phenotypical reality. *Neurological Sciences*, 39(7):1161–1168, 2018.

[113] Dolores Hambardzumyan and Gabriele Bergers. Glioblastoma: defining tumor niches. *Trends in cancer*, 1(4):252–265, 2015.

[114] Davide Schiffer, Laura Annovazzi, Cristina Casalone, Cristiano Corona, and Marta Mellai. Glioblastoma: microenvironment and niche concept. *Cancers*, 11(1):5, 2018.

[115] Diana A Aderetti, Vashendriya VV Hira, Remco J Molenaar, and Cornelis JF van Noorden. The hypoxic peri-arteriolar glioma stem cell niche, an integrated concept of five types of niches in human glioblastoma. *Biochimica et Biophysica Acta (BBA)-Reviews on Cancer*, 1869(2):346–354, 2018.

[116] Christopher Calabrese, Helen Poppleton, Mehmet Kocak, Twala L Hogg, Christine Fuller, Blair Hamner, Eun Young Oh, M Waleed Gaber, David Finklestein, Meredith Allen, et al. A perivascular niche for brain tumor stem cells. *Cancer cell*, 11(1):69–82, 2007.

[117] Frank Winkler, Sergey V Kozin, Ricky T Tong, Sung-Suk Chae, Michael F Booth, Igor Garkavtsev, Lei Xu, Daniel J Hicklin, Dai Fukumura, Emmanuelle di Tomaso, et al. Kinetics of vascular normalization by vegfr2 blockade governs brain tumor response to radiation: role of oxygenation, angiopoietin-1, and matrix metalloproteinases. *Cancer cell*, 6(6):553–563, 2004.

[118] Lucia Ricci-Vitiani, Roberto Pallini, Mauro Biffoni, Matilde Todaro, Gloria Invernici, Tonia Cenci, Giulio Maira, Eugenio Agostino Parati, Giorgio Stassi, Luigi Maria Larocca, et al. Tumour vascularization via endothelial differentiation of glioblastoma stem-like cells. *Nature*, 468(7325):824–828, 2010.

[119] Matthew E Hardee and David Zagzag. Mechanisms of glioma-associated neovascularization. *The American journal of pathology*, 181(4):1126–1141, 2012.

[120] Zhizhong Li, Shideng Bao, Qiulian Wu, Hui Wang, Christine Eyler, Sith Sathornsumetee, Qing Shi, Yiting Cao, Justin Lathia, Roger E McLendon, et al. Hypoxia-inducible factors regulate tumorigenic capacity of glioma stem cells. *Cancer cell*, 15(6):501–513, 2009.

[121] Alina Filatova, Sascha Seidel, Nuray Böğürcü, Sabine Gräf, Boyan K Garvalov, and Till Acker. Acidosis acts through hsp90 in a phd/vhl-independent manner to promote hif function and stem cell maintenance in gliomaacidosis promotes hif and glioma stem cells. *Cancer research*, 76(19):5845–5856, 2016.

[122] Matthias Osswald, Erik Jung, Felix Sahm, Gergely Solecki, Varun Venkataramani, Jonas Blaes, Sophie Weil, Heinz Horstmann, Benedikt Wiestler, Mustafa Syed, et al. Brain tumour cells interconnect to a functional and resistant network. *Nature*, 528(7580):93–98, 2015.

[123] Douglas Hanahan and Robert A Weinberg. Hallmarks of cancer: the next generation. *cell*, 144(5):646–674, 2011.

[124] Mikala Egeblad, Elizabeth S Nakasone, and Zena Werb. Tumors as organs: complex tissues that interface with the entire organism. *Developmental cell*, 18(6):884–901, 2010.

[125] Sophie Weil, Matthias Osswald, Gergely Solecki, Julia Grosch, Erik Jung, Dieter Lemke, Miriam Ratliff, Daniel Hänggi, Wolfgang Wick, and Frank Winkler. Tumor microtubes convey resistance to surgical lesions and chemotherapy in gliomas. *Neuro-oncology*, 19(10):1316–1326, 2017.

[126] Varun Venkataramani, Dimitar Ivanov Tanev, Christopher Strahle, Alexander Studier-Fischer, Laura Fankhauser, Tobias Kessler, Christoph Körber, Markus Kardorff, Miriam Ratliff, Ruifan Xie, et al. Glutamatergic synaptic input to glioma cells drives brain tumour progression. *Nature*, 573(7775):532–538, 2019.

[127] Ruifan Xie, Tobias Kessler, Julia Grosch, Ling Hai, Varun Venkataramani, Lulu Huang, Dirk C Hoffmann, Gergely Solecki, Miriam Ratliff, Matthias Schlesner, et al. Tumor cell network integration in glioma represents a stemness feature. *Neuro-oncology*, 23(5):757–769, 2021.

[128] Pavlo G Gritsenko, Nader Atlasy, Cindy EJ Dieteren, Anna C Navis, Jan-Hendrik Venhuizen, Cornelia Veelken, Dirk Schubert, Amparo Acker-Palmer, Bart A Westerman, Thomas Wurdinger, et al. p120-catenin-dependent collective brain infiltration by glioma cell networks. *Nature cell biology*, 22(1):97–107, 2020.

[129] Humsa S Venkatesh, Tessa B Johung, Viola Caretti, Alyssa Noll, Yujie Tang, Surya Nagaraja, Erin M Gibson, Christopher W Mount, Jai Polepalli, Siddhartha S Mitra, et al. Neuronal activity promotes glioma growth through neuroligin-3 secretion. *Cell*, 161(4):803–816, 2015.

[130] Humsa S Venkatesh, Lydia T Tam, Pamelyn J Woo, James Lennon, Surya Nagaraja, Shawn M Gillespie, Jing Ni, Damien Y Duveau, Patrick J Morris, Jean J Zhao, et al. Targeting neuronal activity-regulated neuroligin-3 dependency in high-grade glioma. *Nature*, 549(7673):533–537, 2017.

[131] Humsa S Venkatesh, Wade Morishita, Anna C Geraghty, Dana Silverbush, Shawn M Gillespie, Marlene Arzt, Lydia T Tam, Cedric Espenel, Anitha Ponnuswami, Lijun Ni, et al. Electrical and synaptic integration of glioma into neural circuits. *Nature*, 573(7775):539–545, 2019.

[132] Varun Venkataramani, Matthias Schneider, Frank Anton Giordano, Thomas Kuner, Wolfgang Wick, Ulrich Herrlinger, and Frank Winkler. Disconnecting multicellular networks in brain tumours. *Nature Reviews Cancer*, pages 1–11, 2022.

[133] Hans-Hermann Gerdes, Amin Rustom, and Xiang Wang. Tunneling nanotubes, an emerging intercellular communication route in development. *Mechanisms of development*, 130(6-8):381–387, 2013.

[134] Giulia Pinto, Christel Brou, and Chiara Zurzolo. Tunneling nanotubes: the fuel of tumor progression? *Trends in Cancer*, 6(10):874–888, 2020.

[135] JH Pate Skene, Richard D Jacobson, G Jackson Snipes, C Brian McGuire, Jeanette J Norden, and John A Freeman. A protein induced during nerve growth (gap-43) is a major component of growth-cone membranes. *Science*, 233(4765):783–786, 1986.

[136] Marcelo Gleiser. How much can we know? *Nature*, 557(7706):S20–S20, 2018.

[137] Kayla J Wolf, Joseph Chen, Jason D Coombes, Manish K Aghi, and Sanjay Kumar. Dissecting and rebuilding the glioblastoma microenvironment with engineered materials. *Nature Reviews Materials*, 4(10):651–668, 2019.

[138] Pascale Monzo, Michele Crestani, and Nils C Gauthier. In vitro mechanobiology of glioma: mimicking the brain blood vessels and white matter tracts invasion paths. In *Brain Tumors*, pages 159–196. Springer, 2021.

[139] Andrew Rape, Badriprasad Ananthanarayanan, and Sanjay Kumar. Engineering strategies to mimic the glioblastoma microenvironment. *Advanced drug delivery reviews*, 79:172–183, 2014.

[140] Devin B Mair, Heather M Ames, and Rong Li. Mechanisms of invasion and motility of high-grade gliomas in the brain. *Molecular biology of the cell*, 29(21):2509–2515, 2018.

[141] John A Pedersen and Melody A Swartz. Mechanobiology in the third dimension. *Annals of biomedical engineering*, 33(11):1469–1490, 2005.

[142] Christopher J Bettinger, Robert Langer, and Jeffrey T Borenstein. Engineering substrate topography at the micro-and nanoscale to control cell function. *Angewandte Chemie International Edition*, 48(30):5406–5415, 2009.

[143] Mark C de Gooijer, Miriam Guillén Navarro, Rene Bernards, Thomas Wurdinger, and Olaf van Tellingen. An experimenter's guide to glioblastoma invasion pathways. *Trends in molecular medicine*, 24(9):763–780, 2018.

[144] Junghwa Cha and Pilnam Kim. Biomimetic strategies for the glioblastoma microenvironment. *Frontiers in Materials*, 4:45, 2017.

[145] Brett W Stringer, Bryan W Day, Rochelle CJ D'Souza, Paul R Jamieson, Kathleen S Ensbey, Zara C Bruce, Yi Chieh Lim, Kate Goasdoué, Carolin Offenhäuser, Seçkin Akgül, et al. A reference collection of patient-derived cell line and xenograft models of proneural, classical and mesenchymal glioblastoma. *Scientific reports*, 9(1):1–14, 2019.

[146] Louis-Bastien Weiswald, Dominique Bellet, and Virginie Dangles-Marie. Spherical cancer models in tumor biology. *Neoplasia*, 17(1):1–15, 2015.

[147] Christopher G Hubert, Maricruz Rivera, Lisa C Spangler, Qiulian Wu, Stephen C Mack, Briana C Prager, Marta Couce, Roger E McLendon, Andrew E Sloan, and Jeremy N Rich. A three-dimensional organoid culture system derived from human glioblastomas recapitulates the hypoxic gradients and cancer stem cell heterogeneity of tumors found in vivobrain cancer stem cell organoids. *Cancer research*, 76(8):2465–2477, 2016.

[148] Theresa A Ulrich, Amit Jain, Kandice Tanner, Joanna L MacKay, and Sanjay Kumar. Probing cellular mechanobiology in three-dimensional culture with collagen–agarose matrices. *Biomaterials*, 31(7):1875–1884, 2010.

[149] Ya-li Yang, Stéphanie Motte, and Laura J Kaufman. Pore size variable type i collagen gels and their interaction with glioma cells. *Biomaterials*, 31(21):5678–5688, 2010.

[150] Ya-li Yang, Charles Sun, Matthew E Wilhelm, Laura J Fox, Jieling Zhu, and Laura J Kaufman. Influence of chondroitin sulfate and hyaluronic acid on structure, mechanical properties, and glioma invasion of collagen i gels. *Biomaterials*, 32(31):7932–7940, 2011.

[151] Christine Wang, Xinming Tong, Xinyi Jiang, and Fan Yang. Effect of matrix metalloproteinase-mediated matrix degradation on glioblastoma cell behavior in 3d peg-based hydrogels. *Journal of Biomedical Materials Research Part A*, 105(3):770–778, 2017.

[152] Badriprasad Ananthanarayanan, Yushan Kim, and Sanjay Kumar. Elucidating the mechanobiology of malignant brain tumors using a brain matrix-mimetic hyaluronic acid hydrogel platform. *Biomaterials*, 32(31):7913–7923, 2011.

[153] Sheeny K áLan Levengood et al. Modeling the tumor microenvironment using chitosan-alginate scaffolds to control the stem-like state of glioblastoma cells. *Biomaterials science*, 4(4):610–613, 2016.

[154] Cristina Martínez-Ramos and Myriam Lebourg. Three-dimensional constructs using hyaluronan cell carrier as a tool for the study of cancer stem cells. *Journal of Biomedical Materials Research Part B: Applied Biomaterials*, 103(6):1249–1257, 2015.

[155] Frank Charbonier, Dhiraj Indana, and Ovijit Chaudhuri. Tuning viscoelasticity in alginate hydrogels for 3d cell culture studies. *Current Protocols*, 1(5):e124, 2021.

[156] Ovijit Chaudhuri, Justin Cooper-White, Paul A Janmey, David J Mooney, and Vivek B Shenoy. Effects of extracellular matrix viscoelasticity on cellular behaviour. *Nature*, 584(7822):535–546, 2020.

[157] IlKyoo Koh, Junghwa Cha, Junseong Park, Junjeong Choi, Seok-Gu Kang, and Pilnam Kim. The mode and dynamics of glioblastoma cell invasion into a decellularized tissue-derived extracellular matrix-based three-dimensional tumor model. *Scientific reports*, 8(1):1–12, 2018.

[158] Hee-Gyeong Yi, Young Hun Jeong, Yona Kim, Yeong-Jin Choi, Hyo Eun Moon, Sung Hye Park, Kyung Shin Kang, Mihyeon Bae, Jinah Jang, Hyewon Youn, et al. A bioprinted human-glioblastoma-on-a-chip for the identification of patient-specific responses to chemoradiotherapy. *Nature Biomedical Engineering*, 3(7):509–519, 2019.

[159] Robert G Thorne and Charles Nicholson. In vivo diffusion analysis with quantum dots and dextrans predicts the width of brain extracellular space. *Proceedings of the National Academy of Sciences*, 103(14):5567–5572, 2006.

[160] Christina M Tringides, Nicolas Vachicouras, Irene de Lázaro, Hua Wang, Alix Trouillet, Bo Ri Seo, Alberto Elosegui-Artola, Florian Fallegger, Yuyoung Shin, Cinzia Casiraghi, et al. Viscoelastic surface electrode arrays to interface with viscoelastic tissues. *Nature Nanotechnology*, 16(9):1019–1029, 2021.

[161] Arvin Arani, Matthew C Murphy, Kevin J Glaser, Armando Manduca, David S Lake, Scott A Kruse, Clifford R Jack Jr, Richard L Ehman, and John Huston 3rd. Measuring the effects of aging and sex on regional brain stiffness with mr elastography in healthy older adults. *Neuroimage*, 111:59–64, 2015.

[162] Joseph Candiello, Manimalha Balasubramani, Emmanuel M Schreiber, Gregory J Cole, Ulrike Mayer, Willi Halfter, and Hai Lin. Biomechanical properties of native basement membranes. *The FEBS journal*, 274(11):2897–2908, 2007.

[163] Theresa A Ulrich, Elena M de Juan Pardo, and Sanjay Kumar. The mechanical rigidity of the extracellular matrix regulates the structure, motility, and proliferation of glioma cells. *Cancer research*, 69(10):4167–4174, 2009.

[164] Giorgio Seano, Hadi T Nia, Kyrre E Emblem, Meenal Datta, Jun Ren, Shanmugarajan Krishnan, Jonas Kloepper, Marco C Pinho, William W Ho, Mitrajit Ghosh, et al. Solid stress in brain tumours causes neuronal loss and neurological dysfunction and can be reversed by lithium. *Nature biomedical engineering*, 3(3):230–245, 2019.

[165] Robert J Pelham Jr and Yu-li Wang. Cell locomotion and focal adhesions are regulated by substrate flexibility. *Proceedings of the national academy of sciences*, 94(25):13661–13665, 1997.

[166] Justin R Tse and Adam J Engler. Preparation of hydrogel substrates with tunable mechanical properties. *Current protocols in cell biology*, 47(1):10–16, 2010.

[167] TW Thomas and PA DiMilla. Spreading and motility of human glioblastoma cells on sheets of silicone rubber depend on substratum compliance. *Medical and Biological Engineering and Computing*, 38(3):360–370, 2000.

[168] Younan Xia and George M Whitesides. Soft lithography. *Angewandte Chemie International Edition*, 37(5):550–575, 1998.

[169] Barbara Cortese, Giuseppe Gigli, and Mathis Riehle. Mechanical gradient cues for guided cell motility and control of cell behavior on uniform substrates. *Advanced Functional Materials*, 19(18):2961–2968, 2009.

[170] Sara Pedron, Eftalda Becka, and Brendan A Harley. Spatially gradated hydrogel platform as a 3d engineered tumor microenvironment. *Advanced Materials*, 27(9):1567–1572, 2015.

[171] Shreyas S Rao, Sarah Bentil, Jessica DeJesus, John Larison, Alex Hissong, Rebecca Dupaix, Atom Sarkar, and Jessica O Winter. Inherent interfacial mechanical gradients in 3d hydrogels influence tumor cell behaviors. *PLoS One*, 7(4):e35852, 2012.

[172] S Pedron and BAC Harley. Impact of the biophysical features of a 3d gelatin microenvironment on glioblastoma malignancy. *Journal of Biomedical Materials Research Part A: An Official Journal of The Society for Biomaterials, The Japanese Society for Biomaterials, and The Australian Society for Biomaterials and the Korean Society for Biomaterials*, 101(12):3404–3415, 2013.

[173] Pavlo Gritsenko, William Leenders, and Peter Friedl. Recapitulating in vivo-like plasticity of glioma cell invasion along blood vessels and in astrocyte-rich stroma. *Histochemistry and cell biology*, 148(4):395–406, 2017.

[174] Andrew D Rape and Sanjay Kumar. A composite hydrogel platform for the dissection of tumor cell migration at tissue interfaces. *Biomaterials*, 35(31):8846–8853, 2014.

[175] Amit Pathak and Sanjay Kumar. Independent regulation of tumor cell migration by matrix stiffness and confinement. *Proceedings of the National Academy of Sciences*, 109(26):10334–10339, 2012.

[176] Alexander Beliveau, Gawain Thomas, Jiaxin Gong, Qi Wen, and Anjana Jain. Aligned nanotopography promotes a migratory state in glioblastoma multiforme tumor cells. *Scientific reports*, 6(1):1–13, 2016.

[177] Shreyas S Rao, Mark T Nelson, Ruipeng Xue, Jessica K DeJesus, Mariano S Viapiano, John J Lannutti, Atom Sarkar, and Jessica O Winter. Mimicking white matter tract topography using core–shell electrospun nanofibers to examine migration of malignant brain tumors. *Biomaterials*, 34(21):5181–5190, 2013.

[178] Paula A Agudelo-Garcia, Jessica K De Jesus, Shante P Williams, Michal O Nowicki, Ennio Antonio Chiocca, Sandya Liyanarachchi, Pui-Kai Li, John J Lannutti, Jed K Johnson, Sean E Lawler, et al. Glioma cell migration on three-dimensional nanofiber

scaffolds is regulated by substrate topography and abolished by inhibition of stat3 signaling. *Neoplasia*, 13(9):831–IN22, 2011.

[179] Marisol Herrera-Perez, Sherry L Voytik-Harbin, and Jenna L Rickus. Extracellular matrix properties regulate the migratory response of glioblastoma stem cells in three-dimensional culture. *Tissue Engineering Part A*, 21(19-20):2572–2582, 2015.

[180] Anjana Jain, Martha Betancur, Gaurangkumar D Patel, Chandra M Valmikinathan, Vivek J Mukhatyar, Ajit Vakharia, S Balakrishna Pai, Barunashish Brahma, Tobey J MacDonald, and Ravi V Bellamkonda. Guiding intracortical brain tumour cells to an extracortical cytotoxic hydrogel using aligned polymeric nanofibres. *Nature materials*, 13(3):308–316, 2014.

[181] Junghwa Cha, Ilkyoo Koh, Yemuk Choi, Jungwhoi Lee, Chulhee Choi, and Pilnam Kim. Tapered microtract array platform for antimigratory drug screening of human glioblastoma multiforme. *Advanced healthcare materials*, 4(3):405–411, 2015.

[182] Bangshang Zhu, Qiqiao Zhang, Qinghua Lu, Yuhong Xu, Jie Yin, Jun Hu, and Zongguang Wang. Nanotopographical guidance of c6 glioma cell alignment and oriented growth. *Biomaterials*, 25(18):4215–4223, 2004.

[183] Daniel Gallego-Perez, Natalia Higuita-Castro, Lisa Denning, Jessica DeJesus, Kirstin Dahl, Atom Sarkar, and Derek J Hansford. Microfabricated mimics of in vivo structural cues for the study of guided tumor cell migration. *Lab on a Chip*, 12(21):4424–4432, 2012.

[184] Marianne Fenech, Vincent Girod, Viviana Claveria, Sebastien Meance, Manouk Abkarian, and Benoit Charlot. Microfluidic blood vasculature replicas using backside lithography. *Lab on a Chip*, 19(12):2096–2106, 2019.

[185] Luca Cucullo, Mohammed Hossain, Ed Rapp, Toby Manders, Nicola Marchi, and Damir Janigro. Development of a humanized in vitro blood–brain barrier model to screen for brain penetration of antiepileptic drugs. *Epilepsia*, 48(3):505–516, 2007.

[186] Luca Cucullo, Nicola Marchi, Mohammed Hossain, and Damir Janigro. A dynamic in vitro bbb model for the study of immune cell trafficking into the central nervous system. *Journal of Cerebral Blood Flow & Metabolism*, 31(2):767–777, 2011.

[187] Luca Cucullo, Mohammed Hossain, Vikram Puvenna, Nicola Marchi, and Damir Janigro. The role of shear stress in blood-brain barrier endothelial physiology. *BMC neuroscience*, 12(1):1–15, 2011.

[188] Kenneth M Chrobak, Daniel R Potter, and Joe Tien. Formation of perfused, functional microvascular tubes in vitro. *Microvascular research*, 71(3):185–196, 2006.

[189] Jeong Ah Kim, Hong Nam Kim, Sun-Kyoung Im, Seok Chung, Ji Yoon Kang, and Nakwon Choi. Collagen-based brain microvasculature model in vitro using three-dimensional printed template. *Biomicrofluidics*, 9(2):024115, 2015.

[190] Xin Cui, Renee-Tyler Tan Morales, Weiyi Qian, Haoyu Wang, Jean-Pierre Gagner, Igor Dolgalev, Dimitris Placantonakis, David Zagzag, Luisa Cimmino, Matija Snuderl, et al. Hacking macrophage-associated immunosuppression for regulating glioblastoma angiogenesis. *Biomaterials*, 161:164–178, 2018.

[191] Andrew D Wong and Peter C Searson. Live-cell imaging of invasion and intravasation in an artificial microvessel platform. *Cancer research*, 74(17):4937–4945, 2014.

[192] Lauren L Bischel, Sang-Hoon Lee, and David J Beebe. A practical method for patterning lumens through ecm hydrogels via viscous finger patterning. *Journal of laboratory automation*, 17(2):96–103, 2012.

[193] Lauren L Bischel, Edmond WK Young, Brianah R Mader, and David J Beebe. Tubeless microfluidic angiogenesis assay with three-dimensional endothelial-lined microvessels. *Biomaterials*, 34(5):1471–1477, 2013.

[194] Anna Herland, Andries D van der Meer, Edward A FitzGerald, Tae-Eun Park, Jelle JF Sleeboom, and Donald E Ingber. Distinct contributions of astrocytes and pericytes to neuroinflammation identified in a 3d human blood-brain barrier on a chip. *PLoS One*, 11(3):e0150360, 2016.

[195] Ying Zheng, Junmei Chen, Michael Craven, Nak Won Choi, Samuel Totorica, Anthony Diaz-Santana, Pouneh Kermani, Barbara Hempstead, Claudia Fischbach-Teschl, José A López, et al. In vitro microvessels for the study of angiogenesis and thrombosis. *Proceedings of the national academy of sciences*, 109(24):9342–9347, 2012.

[196] Jordan S Miller, Kelly R Stevens, Michael T Yang, Brendon M Baker, Duc-Huy T Nguyen, Daniel M Cohen, Esteban Toro, Alice A Chen, Peter A Galie, Xiang Yu, et al. Rapid casting of patterned vascular networks for perfusable engineered three-dimensional tissues. *Nature materials*, 11(9):768–774, 2012.

[197] Laëtitia Andrique, Gaëlle Recher, Kévin Alessandri, Nadège Pujol, Maxime Feyeux, Pierre Bon, Laurent Cognet, Pierre Nassoy, and Andreas Bikfalvi. A model of guided

cell self-organization for rapid and spontaneous formation of functional vessels. *Science advances*, 5(6):eaau6562, 2019.

[198] Sudong Kim, Hyunjae Lee, Minhwan Chung, and Noo Li Jeon. Engineering of functional, perfusable 3d microvascular networks on a chip. *Lab on a Chip*, 13(8):1489–1500, 2013.

[199] Marco Campisi, Yoojin Shin, Tatsuya Osaki, Cynthia Hajal, Valeria Chiono, and Roger D Kamm. 3d self-organized microvascular model of the human blood-brain barrier with endothelial cells, pericytes and astrocytes. *Biomaterials*, 180:117–129, 2018.

[200] Yuta Chonan, Sotaro Taki, Oltea Sampetrean, Hideyuki Saya, and Ryo Sudo. Endothelium-induced three-dimensional invasion of heterogeneous glioma initiating cells in a microfluidic coculture platform. *Integrative Biology*, 9(9):762–773, 2017.

[201] David W Infanger, YouJin Cho, Brina S Lopez, Sunish Mohanan, S Chris Liu, Demirkan Gursel, John A Boockvar, and Claudia Fischbach. Glioblastoma stem cells are regulated by interleukin-8 signaling in a tumoral perivascular nicheinterleukin-8 signaling on glioblastoma tumor stem cells. *Cancer research*, 73(23):7079–7089, 2013.

[202] Jacquelyn A Brown, Virginia Pensabene, Dmitry A Markov, Vanessa Allwardt, M Diana Neely, Mingjian Shi, Clayton M Britt, Orlando S Hoilett, Qing Yang, Bryson M Brewer, et al. Recreating blood-brain barrier physiology and structure on chip: A novel neurovascular microfluidic bioreactor. *Biomicrofluidics*, 9(5):054124, 2015.

[203] Hui Xu, Zhongyu Li, Yue Yu, Saman Sizdahkhani, Winson S Ho, Fangchao Yin, Li Wang, Guoli Zhu, Min Zhang, Lei Jiang, et al. A dynamic in vivo-like organotypic blood-brain barrier model to probe metastatic brain tumors. *Scientific reports*, 6(1):1–12, 2016.

[204] Danh Truong, Roberto Fiorelli, Eric S Barrientos, Ernesto Luna Melendez, Nader Sanai, Shwetal Mehta, and Mehdi Nikkhah. A three-dimensional (3d) organotypic microfluidic model for glioma stem cells–vascular interactions. *Biomaterials*, 198:63–77, 2019.

[205] Jose M Ayuso, Rosa Monge, Alicia Martínez-González, María Virumbrales-Muñoz, Guillermo A Llamazares, Javier Berganzo, Aurelio Hernández-Laín, Jorge Santolaria, Manuel Doblaré, Christopher Hubert, et al. Glioblastoma on a microfluidic chip: Generating pseudopalisades and enhancing aggressiveness through blood vessel obstruction events. *Neuro-oncology*, 19(4):503–513, 2017.

[206] Yuk Kien Chong, Edwin Sandanaraj, Lynnette WH Koh, Moogaambikai Thangaveloo, Melanie SY Tan, Geraldene RH Koh, Tan Boon Toh, Grace GY Lim, Joanna D Holbrook, Oi Lian Kon, et al. St3gal1-associated transcriptomic program in glioblastoma tumor growth, invasion, and prognosis. *JNCI: Journal of the National Cancer Institute*, 108(2), 2016.

[207] Melanie Si Yan Tan, Edwin Sandanaraj, Yuk Kien Chong, See Wee Lim, Lynnette Wei Hsien Koh, Wai Hoe Ng, Nguan Soon Tan, Patrick Tan, Beng Ti Ang, and Carol Tang. A stat3-based gene signature stratifies glioma patients for targeted therapy. *Nature communications*, 10(1):1–15, 2019.

[208] Bert Grobben, Peter De Deyn, and Herman Slegers. Rat c6 glioma as experimental model system for the study of glioblastoma growth and invasion. *Cell and tissue research*, 310(3):257–270, 2002.

[209] Franck Polleux and Anirvan Ghosh. The slice overlay assay: a versatile tool to study the influence of extracellular signals on neuronal development. *Science's STKE*, 2002(136):pl9–pl9, 2002.

[210] Jonathan E Ron, Pascale Monzo, Nils C Gauthier, Raphael Voituriez, and Nir S Gov. One-dimensional cell motility patterns. *Physical Review Research*, 2(3):033237, 2020.

[211] Jed Johnson, M Oskar Nowicki, Carol H Lee, E Antonio Chiocca, Mariano S Viapiano, Sean E Lawler, and John J Lannutti. Quantitative analysis of complex glioma cell migration on electrospun polycaprolactone using time-lapse microscopy. *Tissue Engineering Part C: Methods*, 15(4):531–540, 2009.

[212] Takanori Ohnishi, Hirotaka Matsumura, Shuichi Izumoto, Shoju Hiraga, and Toru Hayakawa. A novel model of glioma cell invasion using organotypic brain slice culture. *Cancer research*, 58(14):2935–2940, 1998.

[213] Maria Vinci, Sharon Gowan, Frances Boxall, Lisa Patterson, Miriam Zimmermann, Cara Lomas, Marta Mendiola, David Hardisson, Suzanne A Eccles, et al. Advances in establishment and analysis of three-dimensional tumor spheroid-based functional assays for target validation and drug evaluation. *BMC biology*, 10(1):1–21, 2012.

[214] Andrew D Doyle, Francis W Wang, Kazue Matsumoto, and Kenneth M Yamada. One-dimensional topography underlies three-dimensional fibrillar cell migration. *Journal of cell biology*, 184(4):481–490, 2009.

[215] Stephanie L Gupton and Clare M Waterman-Storer. Spatiotemporal feedback between actomyosin and focal-adhesion systems optimizes rapid cell migration. *Cell*, 125(7):1361–1374, 2006.

[216] Mario L Suvà and Itay Tirosh. The glioma stem cell model in the era of single-cell genomics. *Cancer cell*, 37(5):630–636, 2020.

[217] Justin D Lathia, Joseph Gallagher, John M Heddleston, Jialiang Wang, Christine E Eyler, Jennifer MacSwords, Qiulian Wu, Amit Vasanji, Roger E McLendon, Anita B Hjelmeland, et al. Integrin alpha 6 regulates glioblastoma stem cells. *Cell stem cell*, 6(5):421–432, 2010.

[218] Varun Venkataramani, Yvonne Yang, Marc Cicero Schubert, Ekin Reyhan, Svenja Kristin Tetzlaff, Niklas Wißmann, Michael Botz, Stella Judith Soyka, Carlo Antonio Beretta, Rangel Lyubomirov Pramatarov, et al. Glioblastoma hijacks neuronal mechanisms for brain invasion. *Cell*, 185(16):2899–2917, 2022.

[219] Weigang Wang, Sumanta Goswami, Kyle Lapidus, Amber L Wells, Jeffrey B Wyckoff, Erik Sahai, Robert H Singer, Jeffrey E Segall, and John S Condeelis. Identification and testing of a gene expression signature of invasive carcinoma cells within primary mammary tumors. *Cancer research*, 64(23):8585–8594, 2004.

[220] Yu-Chih Chen, Steven G Allen, Patrick N Ingram, Ronald Buckanovich, Sofia D Merajver, and Euisik Yoon. Single-cell migration chip for chemotaxis-based microfluidic selection of heterogeneous cell populations. *Scientific reports*, 5(1):1–13, 2015.

[221] Aditya Arora, Jorge Luis Galeano Niño, Myint Zu Myaing, Shumei Chia, Bakya Arasi, Andrea Ravasio, Ruby Yun-Ju Huang, Ramanuj Dasgupta, Maté Biro, and Virgile Viasnoff. Two high-yield complementary methods to sort cell populations by their 2d or 3d migration speed. *Molecular biology of the cell*, 31(25):2779–2790, 2020.

[222] Christopher L Yankaskas, Keyata N Thompson, Colin D Paul, Michele I Vitolo, Panagiotis Mistriotis, Ankit Mahendra, Vivek K Bajpai, Daniel J Shea, Kristen M Manto, Andreas C Chai, et al. A microfluidic assay for the quantification of the metastatic propensity of breast cancer specimens. *Nature biomedical engineering*, 3(6):452–465, 2019.

[223] Michele Crestani, Tania Dini, Nils C Gauthier, and Pascale Monzo. Protocol to assess human glioma propagating cell migration on linear micropatterns mimicking brain invasion tracks. *STAR protocols*, 3(2):101331, 2022.

[224] Timothée Vignaud, Hajer Ennomani, and Manuel Thery. Polyacrylamide hydrogel micropatterning. In *Methods in cell biology*, volume 120, pages 93–116. Elsevier, 2014.

[225] Roger Stupp, Monika E Hegi, Thierry Gorlia, Sara C Erridge, James Perry, Yong-Kil Hong, Kenneth D Aldape, Benoit Lhermitte, Torsten Pietsch, Danica Grujicic, et al. Cilengitide combined with standard treatment for patients with newly diagnosed glioblastoma with methylated mgmt promoter (centric eortc 26071-22072 study): a multicentre, randomised, open-label, phase 3 trial. *The lancet oncology*, 15(10):1100–1108, 2014.

[226] Derek Thompson. America is running on fumes. *The Atlantic*, https://www.theatlantic.com/ideas/archive/2021/12/america-innovation-film-science-business/620858/, 2021.

[227] Jay Bhattacharya and Mikko Packalen. Stagnation and scientific incentives. Technical report, National Bureau of Economic Research, 2020.

[228] Bruce Alberts. Impact factor distortions, 2013.

[229] Thomas D Brock and Hudson Freeze. Thermus aquaticus gen. n. and sp. n., a nonsporulating extreme thermophile. *Journal of bacteriology*, 98(1):289–297, 1969.

[230] Alice Chien, David B Edgar, and John M Trela. Deoxyribonucleic acid polymerase from the extreme thermophile thermus aquaticus. *Journal of bacteriology*, 127(3):1550–1557, 1976.

[231] Randall K Saiki, David H Gelfand, Susanne Stoffel, Stephen J Scharf, Russell Higuchi, Glenn T Horn, Kary B Mullis, and Henry A Erlich. Primer-directed enzymatic amplification of dna with a thermostable dna polymerase. *Science*, 239(4839):487–491, 1988.

[232] Johan SG Chu and James A Evans. Slowed canonical progress in large fields of science. *Proceedings of the National Academy of Sciences*, 118(41):e2021636118, 2021.

[233] Kevin J Boudreau, Eva C Guinan, Karim R Lakhani, and Christoph Riedl. Looking across and looking beyond the knowledge frontier: Intellectual distance, novelty, and resource allocation in science. *Management science*, 62(10):2765–2783, 2016.

[234] Aaron Daniel Cohen, Adam Roberts, Alejandra Molina, Alena Butryna, Alicia Jin, Apoorv Kulshreshtha, Ben Hutchinson, Ben Zevenbergen, Blaise Hilary Aguera-Arcas, Chung ching Chang, Claire Cui, Cosmo Du, Daniel De Freitas Adiwardana,

Dehao Chen, Dmitry (Dima) Lepikhin, Ed H. Chi, Erin Hoffman-John, Heng-Tze Cheng, Hongrae Lee, Igor Krivokon, James Qin, Jamie Hall, Joe Fenton, Johnny Soraker, Kathy Meier-Hellstern, Kristen Olson, Lora Mois Aroyo, Maarten Paul Bosma, Marc Joseph Pickett, Marcelo Amorim Menegali, Marian Croak, Mark Díaz, Matthew Lamm, Maxim Krikun, Meredith Ringel Morris, Noam Shazeer, Quoc V. Le, Rachel Bernstein, Ravi Rajakumar, Ray Kurzweil, Romal Thoppilan, Steven Zheng, Taylor Bos, Toju Duke, Tulsee Doshi, Vinodkumar Prabhakaran, Will Rusch, YaGuang Li, Yanping Huang, Yanqi Zhou, Yuanzhong Xu, and Zhifeng Chen. Lamda: Language models for dialog applications. In *arXiv*. 2022.

[235] Nitasha Tiku. The google engineer who thinks the company's ai has come to life. *The Washington Post*, https://www.washingtonpost.com/technology/2022/06/11/google-ai-lamda-blake-lemoine/, 2022.

[236] Nicholas Bloom, Charles I Jones, John Van Reenen, and Michael Webb. Are ideas getting harder to find? *American Economic Review*, 110(4):1104–44, 2020.

[237] Gina Kolata. Grant system leads cancer researchers to play it safe. *New York Times*, 28, 2009.

[238] Editors. Dr. no money: The broken science funding system. *Scientific American*, 2011.

[239] Danielle Li and Leila Agha. Big names or big ideas: Do peer-review panels select the best science proposals? *Science*, 348(6233):434–438, 2015.

[240] Ferric C Fang and Arturo Casadevall. Grant funding: Playing the odds. *Science*, 352(6282):158–158, 2016.

[241] Marc Andreessen. It's time to build. *Future*, https://future.com/its-time-to-build/, 2020.

[242] Zeynep Tufekci. Why did it take so long to accept the facts about covid. *The New York Times*, 7, 2021.

[243] Ezra Klein. Why we can't build. *Vox*, https://www.vox.com/2020/4/22/21228469/marc-andreessen-build-government-coronavirus, 2020.

[244] Kirstin RW Matthews, Kara M Calhoun, Nathan Lo, and Vivian Ho. The aging of biomedical research in the united states. *PloS one*, 6(12):e29738, 2011.

[245] Benjamin F Jones. The burden of knowledge and the "death of the renaissance man": Is innovation getting harder? *The Review of Economic Studies*, 76(1):283–317, 2009.

[246] Ron Zemke, Claire Raines, and Bob Filipczak. *Generations at work: Managing the clash of Boomers, Gen Xers, and Gen Yers in the workplace*. Amacom, 2013.

[247] Paul Millerd. The boomer blockade: How one generation reshaped the workforce and left everyone behind. https://think-boundless.com/the-boomer-blockade/, 2020.

[248] Dudley Shapere. The structure of scientific revolutions. *The Philosophical Review*, 73(3):383–394, 1964.

[249] Pierre Azoulay, Christian Fons-Rosen, and Joshua S Graff Zivin. Does science advance one funeral at a time? *American Economic Review*, 109(8):2889–2920, 2019.

[250] Max Planck. Scientific autobiography. *Williams and Norgate, London*, pages 33–34, 1950.

[251] David L Hull, Peter D Tessner, and Arthur M Diamond. Planck's principle: Do younger scientists accept new scientific ideas with greater alacrity than older scientists? *Science*, 202(4369):717–723, 1978.

[252] Patrick Collison, Tyler Cowen, and Patrick Hsu. What we learned doing fast grants. *Future*, https://future.com/what-we-learned-doing-fast-grants/, 2021.

[253] Jean-Philippe Bouchaud. Economics needs a scientific revolution. *Nature*, 455(7217):1181–1181, 2008.

[254] José Luis Ricón. We don't know how to fix science. *Works in progress*, 4:https://www.worksinprogress.co/issue/we–dont–know–how–to–fix–science/, 2021.

[255] Ekrem Emrah Er, Manuel Valiente, Karuna Ganesh, Yilong Zou, Saloni Agrawal, Jing Hu, Bailey Griscom, Marc Rosenblum, Adrienne Boire, Edi Brogi, et al. Pericyte-like spreading by disseminated cancer cells activates yap and mrtf for metastatic colonization. *Nature cell biology*, 20(8):966–978, 2018.

[256] Yoojin Shin, Sewoon Han, Jessie S Jeon, Kyoko Yamamoto, Ioannis K Zervantonakis, Ryo Sudo, Roger D Kamm, and Seok Chung. Microfluidic assay for simultaneous culture of multiple cell types on surfaces or within hydrogels. *Nature protocols*, 7(7):1247–1259, 2012.

[257] Roman Gorelik and Alexis Gautreau. Quantitative and unbiased analysis of directional persistence in cell migration. *Nature protocols*, 9(8):1931–1943, 2014.

[258] Rana Rezakhaniha, Aristotelis Agianniotis, Jelle Tymen Christiaan Schrauwen, Alessandra Griffa, Daniel Sage, CVC vd Bouten, FN Van De Vosse, Michaël Unser, and Nikolaos Stergiopulos. Experimental investigation of collagen waviness and orientation in the arterial adventitia using confocal laser scanning microscopy. *Biomechanics and modeling in mechanobiology*, 11(3):461–473, 2012.

[259] Alexander Dobin, Carrie A Davis, Felix Schlesinger, Jorg Drenkow, Chris Zaleski, Sonali Jha, Philippe Batut, Mark Chaisson, and Thomas R Gingeras. Star: ultrafast universal rna-seq aligner. *Bioinformatics*, 29(1):15–21, 2013.

[260] Rob Patro, Geet Duggal, Michael I Love, Rafael A Irizarry, and Carl Kingsford. Salmon provides fast and bias-aware quantification of transcript expression. *Nature methods*, 14(4):417–419, 2017.

[261] Michael I Love, Wolfgang Huber, and Simon Anders. Moderated estimation of fold change and dispersion for rna-seq data with deseq2. *Genome biology*, 15(12):1–21, 2014.

[262] Alexey Sergushichev. An algorithm for fast preranked gene set enrichment analysis using cumulative statistic calculation. *BioRxiv*, 60012:1–9, 2016.